

Alma Mater Studiorum – Università di Bologna

DOTTORATO DI RICERCA IN

Meccanica e Scienze Avanzate dell'Ingegneria

Ciclo XXX

Settore Concorsuale: 09/B1

Settore Scientifico Disciplinare: ING-IND/16

Mechanical performance assessment and dynamic crash simulation of composite materials

Presentata da: Francesco Rondina

Coordinatore Dottorato

Prof: Marco Carricato

Supervisore

Prof: Lorenzo Donati

Esame finale anno 2018

Abstract

In this PhD thesis, several technological aspects regarding the use of fibre reinforced composite materials are presented. The crashworthiness topic is studied with the aim to build and calibrate a numerical damage model for the prediction of the energies absorbed during axial crush of a sample specimen. A full experimental characterisation campaign is implemented, and several simulations are used to reach the final validation stage. Following, a small-scale test setup was developed and built to measure the permeability of dry reinforcement, necessary to predict and simulate the flow front propagation in resin injection processes. Test results are compared with experimental trials. Finally, an overview on innovative metal-composite bonding techniques using additive manufacturing processes is presented, highlighting the principal design variables that come into play in developing such advanced connections.

CONTENTS

1. Composite materials: matrix, reinforcement and manufacturing process	1
2. Crashworthiness: definition and modelling	3
2.1 Basic orthotropic constitutive behaviour	4
2.2 Ladevèze Continuum Damage Model	5
2.2.1 Fibre damage	6
2.2.2 Matrix damage	7
2.2.3 Matrix plasticity	9
2.3 Waas-Pineda progressive damage model	9
2.3.1 Initiation	10
2.3.2 Fibre damage	12
2.3.3 Matrix damage	13
2.3.4 Post-damage state	14
2.4 Cohesive zone model	14
2.5 Building block approach	16
3. Experimental Campaign	19
3.1 Materials and methods	19
3.2 Mechanical tests	20
3.2.1 Static tensile	20
3.2.2 Static compressive	22
3.2.3 Static in-plane shear	24
3.2.4 Cyclic in-plane shear	25
3.2.5 DCB delamination	28
3.2.6 ENF delamination	30

3.2.7	<i>Compact Tension</i>	33
3.2.8	<i>Compact Compression</i>	36
3.3	Summary of material properties	39
3.4	Validation crush test	40
4.	Validation of numerical crash model	43
4.1	Composite simulation in VPS	43
4.1.1	<i>Orthotropic Composite material model</i>	44
4.1.2	<i>Ladevèze damage model</i>	46
4.1.3	<i>Waas Pineda Failure model</i>	48
4.1.4	<i>Tied interface model</i>	48
4.1.5	<i>Contact pairs definitions</i>	49
4.2	Coupon level simulations with Ladevèze CDM	50
4.2.1	<i>Tensile load</i>	51
4.2.2	<i>Compressive load</i>	51
4.2.3	<i>Shear load</i>	52
4.2.4	<i>Mode I delamination</i>	53
4.2.5	<i>Mode II delamination</i>	56
4.2.6	<i>Inter-ply fracture</i>	57
4.3	Coupon level simulations with WP failure	59
4.2.6	<i>Tensile load</i>	59
4.2.6	<i>Shear load</i>	60
4.3.3	<i>Inter-ply fracture load</i>	60
4.4	Setup of crush loading simulations	62
4.4.1	<i>Contact algorithms</i>	62
4.4.2	<i>Boundary conditions</i>	62
4.4.3	<i>Element elimination strategy</i>	63
4.4.4	<i>Numerical trigger</i>	63
4.5	Validation of crush loading simulation	64
5.	Measurement of textile permeability in composite injection processes	71
5.1	Experimental determination of permeability	72

5.1.1 <i>Unsaturated linear flow</i>	73
5.1.2 <i>Unsaturated radial flow</i>	74
5.2 Experimental setup	75
5.3 Test results	77
5.4 Validation	80
6. 3D reinforcement techniques for CFRP to metal joints	81
6.1 Classical 3D-reinforcement techniques	81
6.2 Bonding techniques using additive manufacturing	83
6.2.1 <i>Pin size investigation</i>	84
6.2.2 <i>Pin shape investigation</i>	85
6.2.3 <i>-Pin offset angle investigation</i>	86
6.2.4 <i>Hybrid Penetrative Reinforcement (HYPER)</i>	87
Conclusions	89
References	91

CHAPTER 1

COMPOSITE MATERIALS: MATRIX, REINFORCEMENT AND MANUFACTURING PROCESS

The increasing adoption of fibre-reinforced composite materials, particularly in the automotive and aerospace industry, is motivated by their low weight, high strength, and flexible manufacturability. In addition to being already widely used for lightweight aesthetical components, composite materials are suitable candidates for many structural load bearing applications, still today prerogative to steel or aluminium alloys. The reason for the delay in the use of fibre-reinforced composites for highly stressed structural components is justified by the lack of reliable tools for the prediction of failure mechanism, the uncertainties regarding fatigue life and environmental effects, and finally, the influence of the full manufacturing process in the performance of the final product.

In this scenario, the ever-stricter regulations for aircrafts and automobiles, the complex safety requirements, raised motivated concerns regarding the structural behaviour during atypical and unexpected conditions like accidents or crash events, in addition to the standard design operating condition. The crashworthiness requirements impose strict boundaries on the transfer and dissipation of the kinetic energy to limit injuries and danger for the occupants, for this reason, confidence in the failure modes and crushing behaviour of a component is of paramount importance for the approval of such components for use in vehicles.

Composite materials have a high degree of flexibility, since they allow the designer to choose among different constituents – the type of fibre and matrix – the layup and orientation the reinforcement and manufacturing processes. In detail, each of these decisions will have an impact on the overall finished product in ways that cannot be assessed separately, leading to onerous characterisation efforts or conservative design choices.

The role of manufacturing comes as additional investigation point. The industry is slowly transitioning from traditional autoclave curing (AC) of composites to modern and cheaper liquid composite moulding (LCM) processes, the most promising represented by resin transfer moulding (RTM) with high injection pressure. In these processes, compacted dry reinforcements are placed in a closed mould which is ultimately impregnated with the curing resin. These processes can nowadays offer competing performances with traditional AC components, with impressively reduced production times. On the other hand, these technologies require expensive equipment in the form of a hydraulic press, and increased tooling costs compared to those for autoclave moulds, so care must be taken in robust design of the impregnation phase. As of today, little is known on the effects of poor impregnation on material performance, and the designer has no validated tools to add this information to the design phase, and often treats this aspect as an additional safety factor.

The most crucial need for the designer is the ability to predict the operating compliances and failure behaviour in a virtual environment, in order to try several design variations in short times and with high accuracy, without recurring to cost-intensive manufacturing trial and error. We know that several uncertainties are still present today, and that the current state of the art still has great margins for improvement, because information is lacking, analytical knowledge is scarce, and variables to consider are numerous. Goal of this work, is to provide tools and best practices to reduce these uncertainties and to guide the designer towards better comprehension of the manufacturing issues, the performance critical points, the failure and after-failure behaviour and to provide guidelines for future experimental investigations.

Three main activities are described in this work, the characterisation of a composite material for crash application is the first topic, where a full experimental campaign is performed to build a numerical tool and validate the crash event of a simplified geometry. Second, a test equipment is developed for the impregnation of fibrous reinforcements, representative of infusion processes. The device is used for permeability characterisation of textiles, necessary for predicting the flow distribution in closed mould impregnation processes. Validation of these experimental tests is part of a separate work. Finally, the design of innovative bonding techniques for metal-to-composite joints are discussed, where the use of innovative technologies in metals (additive manufacturing) is used to produce features that allow a superior bond with lower weight penalties compared to traditional solutions.

The work is divided between analytical investigations, experimental tests, and finally, numerical simulations. All experimental campaigns are done in the laboratory of mechanics at the University of Bologna situated in Forlì. For some tests, specific acquisition techniques, procedures and equipment have been developed in order to obtain the desired material properties and investigate the necessary damage and failure modes. These tests, defined to obtain evidence from simple cases, are compared to analytical models found in literature and ultimately verified in numerical environment. Likewise, the permeability test bench was manufactured internally following specifications approved by other research groups, and adapted to the laboratory environment. All numerical activities presented are done using ESI FE software.

CHAPTER 2

CRASHWORTHINESS: DEFINITION AND MODELLING

Lightweight requirement in transport industry demand a shift in the adoption of composite material, initially relegated to aesthetic and external surfaces, they now find their way in the structural and critically loaded components, where advantages in comparison with metal alloys are significant. In contrast with this, regulation agencies demand that these structural components meet severe criteria in case of impacts, accidents and crash, the full extent of these requirements is beyond the scope of this work, but the basic guidelines are reported here for clarity.

All different aspects regarding safety of a vehicle's occupants in case of accident can be unified under the term of crashworthiness. Specifically, we will talk about crashworthy design when an engineering process takes into account properties regarding the safety of the occupants and the different ways that these goals are met. Global principles are, among specific others:

- Maintain the occupants' survival space
- Manage collision energy
- Restrain the occupants and prevent ejection
- Maintain exit paths functional and visible
- Confine hazardous materials and prevent fire

Of these goals, some are met through the use and inclusion of active devices, as for example seatbelts, airbags, while others, regarding the integrity of the vehicle, are typically demanded by the load carrying structural frame. The second point of the above list is the main focus of this work, and must be dealt with particular attention.

The need to dissipate the kinetic energy in case of crash is directly connected with the safety of the occupants, as the high velocities must be managed in a controlled way. It is found that there is an upper limit to the tolerance of human body to sustain strong decelerations for a certain amount of time, therefore, the components in charge of dissipating the kinetic energy would impose a soft compliant behaviour producing low and safe decelerations. This is in contrast with the stringent geometric and space constraints, as well as the stiffness requirements of a structure, e.g. in a car's engine bay.

It is also clear then that any regulation requirement that must be verified on a physical structure, or certified by detailed reports, must be addressed with all the analytical and numerical tools available to the engineer, and any trial and error approach must be minimised in favour of advanced predictive methods, not to incur in costly and time-consuming activities.

When dealing with crash simulation of composite materials, it is important to distinguish the different stages that the material undergoes during its loading, from the basic undamaged behaviour, to the damage progression mechanisms and the ultimate post-damage behaviour.

Whereas metallic materials can be successfully described using only an elastic-plastic law to model the full straining range happening during crush deformation, the same cannot apply to composites. These materials are characterised by highly anisotropic damage phenomena and subsequent softening, with respects to the reinforcement orientation. Moreover, these modes of damage can be coupled with each other, resulting in a mixed contribution to the damage formation and effects.

Macroscopically, the modes of failure observed in compressive crush loading of composite structures are:

- Fibre fragmentation
- Splaying of fronds
- Wall buckling.

These modes, extensively investigated by Mamalis et. al. [1,2] are associated with vastly different energy dissipations, in particular, flatter sections will tend to fail by buckling and splaying, whereas curved geometries are associated with higher rates of fibre fragmentation, and higher energy and sustained load during crushing are observed. In addition, it is found that these modes are dominated by the geometry and material layup [3] more than they are governed by the particular material performance. Hence the difference in modelling numerically the crush events in a software environment. The FE model will have to contain all these failure modes and correctly interpret the role of geometry in the crushing evolution. furthermore, an aspect associated to the laminated nature of composite materials, is the inter-ply delamination damage, which can cause profound deformation of a component. These phenomena should be taken into account when modelling a crush simulation, therefore the FE representation must include these fault planes for example through the adoption of tied connection between adjacent plies, defined by a discrete cohesive traction-separation law.

In the following paragraphs, we will introduce and describe in detail the numerical representation of fibrous reinforced materials available in the FE software ESI Virtual Performance Solution (VPS).

2.1 Basic orthotropic constitutive behaviour

The basic undamaged elastic properties of a composite lamina will show anisotropic behaviour in the fibre plane, having a ratio between elastic modulus in the fibre direction versus transverse and shear moduli typically between 10 and 50. From the general anisotropic model, through symmetries and assumptions, it is possible to simplify the constitutive law to an orthotropic model, and additionally neglect the coupling terms between tension and shear. For a numerical model built with shell elements, the constitutive matrix for the single lamina will have only four independent terms:

$$\begin{pmatrix} \sigma_{11} \\ \sigma_{22} \\ \sigma_{12} \end{pmatrix} = \begin{pmatrix} E_{11} & -\nu_{12} & 0 \\ -\nu_{12} & E_{22} & 0 \\ 0 & 0 & G_{12} \end{pmatrix} \begin{pmatrix} \varepsilon_1 \\ \varepsilon_2 \\ \varepsilon_{12} \end{pmatrix} \quad (2.1)$$

In addition, through classical laminate theory (CLT), it is demonstrated that when a layup is balanced and symmetrical, the constitutive matrix of the whole layup is also orthotropic, coupling between shear and tension, shear and bending are removed, which is typically the ideal starting condition in the designing process of composite components.

In VPS, the numerical model of the composite layup can be implemented using a multi-layered shell, or through a stack of single-layered shells. The former solution allows a fast and easy setup, while the latter must be coupled with links between each ply to represent the interfaces.

In both cases, it is possible to output the stress and strain relation of each individual ply, as well as the damage effects (described later), but the multi-layered approach loses the ability to show separation between plies, and the forces related to it. Given that the splaying mode plays an important role during crushing, we decided to simulate all cases using the stacked shell approach. It is important, as will be made clear in Chapter 5, that all simulations be carried out with the same material card and numerical method. This removes all possible sources of uncertainty during the calibration of the model and analysis of results.

2.2 Ladevèze Continuum Damage Model

The damage model proposed by Ladevèze has its origins in a series of papers from around two decades ago. The first description of the conceptual framework is found in Allix et. al. [4] and Ladevèze, LeDantec [5], where the basic assumption and functionality of the model are described, while in later publications [6,7] validations are presented for simple and complex load cases where softening and failure are identified.

The basic concept of this model comes from the idea of Kachanov [8] that the deterioration of the material can be described by its effect on the elastic characteristics. The classical theory used for isotropic materials by Lemaitre [9] cannot apply successfully to composites, because the modes of damage are multiple and their effects are different and highly anisotropic. In addition, the idea of homogenisation of the elastic properties must be included, and the scale of the physical phenomena defined. This model doesn't deal with the micromechanics of fibre and matrix, but deals with phenomena at a higher magnitude scale, it is called a meso-model. Its goal is to represent the global response of the material starting from the local deformation status of the individual lamina.

The damaged condition is expressed as an alteration (reduction) of the Young's modulus in each direction. Basic simplifications are that the damage parameters are scalars and are "non-healing", meaning that their value at any given time cannot decrease. The criterion to activate and increase damage parameters during loading make up for the most part of the damage model.

2.2.1 Fibre damage

Fibre damage is treated in a rather simplified manner. This is based on linear modulus reduction between two limit strains, followed by a saturated region after the upper bound is reached and kept until end of run or the element is eliminated. This reduces the formulation as follows

- Sub-critical damage:

$$E_{11} = E_{11}^{0t} \text{ for } \varepsilon_{11} < \varepsilon_i^{ft} \quad 2.4$$

- Critical damage:

$$E_{11} = E_{11}^{0t}(1 - d^{ft}) \text{ with } d^{ft} = d_u^{ft} \frac{\varepsilon_{11} - \varepsilon_i^{ft}}{\varepsilon_u^{ft} - \varepsilon_i^{ft}} \text{ for } \varepsilon_i^{ft} < \varepsilon_{11} < \varepsilon_u^{ft} \quad 2.5$$

- Post-critical damage:

$$E_{11} = E_{11}^{0t}(1 - d^{ft}) \text{ with } d^{ft} = 1 - (1 - d_u^{ft}) \frac{\varepsilon_{11}}{\varepsilon_u^{ft}} \quad 2.6$$

As explained, post-critical damage above is written in a way that the stress is kept constant for increasing strain, while imposing the stiffness for total strain recovery upon unloading, this returns d^{ft} to asymptotically reach 1 with ever increasing strain. The following definitions apply:

- E_{11}^{0t} is the initial undamaged Young's modulus in 11 direction under traction;
- ε_i^{ft} is the initial (lower) strain damage limit;
- ε_u^{ft} is the ultimate (higher) strain damage limit, associated to full axial damage of the fibres;
- d_u^{ft} is the ultimate damage limit associated to ε_u^{ft} .

In compression, the same relations apply, with the option to have added softening upon loading. This phenomenon is found from experimental tests of composite specimens and has the following form

$$E_{11}^{\gamma} = \frac{E_{11}^{0c}}{1 + \gamma E_{11}^{0c} |\varepsilon_{11}|} \quad 2.7$$

So that the general damage evolution mechanism is as follows:

- Sub-critical damage:

$$E_{11} = E_{11}^{\gamma} \text{ for } |\varepsilon_{11}| < \varepsilon_i^{fc} \quad 2.8$$

- Critical damage:

$$E_{11} = E_{11}^{\gamma}(1 - d^{fc}) \text{ with } d^{fc} = d_u^{fc} \frac{|\varepsilon_{11}| - \varepsilon_i^{fc}}{\varepsilon_u^{fc} - \varepsilon_i^{fc}} \text{ for } \varepsilon_i^{fc} < |\varepsilon_{11}| < \varepsilon_u^{fc} \quad 2.9$$

- Post-critical damage:

$$E_{11} = E_{11}^Y (1 - d^{fc}) \text{ with } d^{fc} = 1 - (1 - d_u^{fc}) \frac{|\varepsilon_{11}|}{\varepsilon_u^{fc}} \text{ for } |\varepsilon_{11}| > \varepsilon_u^{fc} . \quad 2.10$$

A graphical representation of the complete damage effects in 11 direction, with limit strains to identify the three distinguished damage regions, is shown in the figure below.

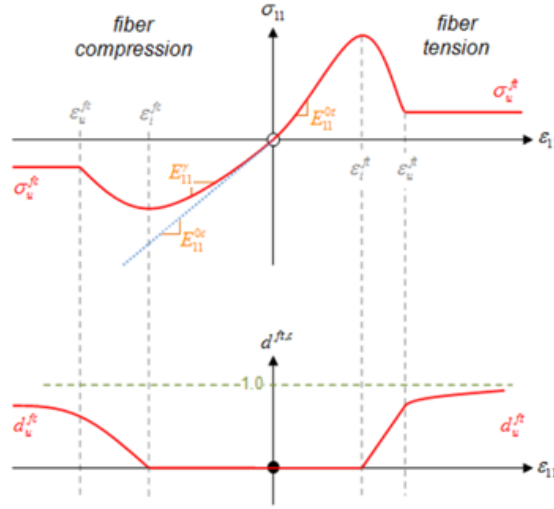


Figure 2.1 – Representation of tensile and compressive damaging model.

2.2.2 Matrix damage

The matrix related damages are taken into account by two scalar variables, d (shear damage) and d' (transverse damage). These variables express experimentally these phenomena: parameter d quantifies the damage which comes from the debonding between fibres and matrix [10], whereas parameter d' is related to the damage due to the micro-cracking of the matrix parallel to the fibre direction [11]. For this reason, the parameters d and d' are applied respectively to the ply shear and transverse modulus. However, tensile and compressive transverse responses must be distinguished, because the micro-cracks grow when the composite ply is under tensile transverse loading, but they close under compression. If needed, a compressive transverse damage can be defined too. The two damage parameters behave as follow in shear mode:

$$G_{12} = G_{12}^0 (1 - d) \quad 2.11$$

where G_{12}^0 is the initial value of ply shear modulus G_{12} ,

$$G_{i3} = G_{i3}^0 d_{shear} \quad i = 1,2 \text{ with } d_{shear} = \min(1 - d, 1 - d') \quad 2.12$$

where G_{13}^0 is the initial value of ply shear moduli G_{13} , while in transverse 22 direction:

$$E_2 = E_2^0(1 - d') \quad 2.12$$

with: E_2^0 is the initial value of ply transverse modulus E_2 .

From this basic framework, the two damage parameter are driven by strain energies through the introduction of the conjugate forces:

The damage functions Z_d for shear damage and Z'_d , for transverse damage, associated respectively with d and d' are defined by the following expressions where E_d is the elastic strain energy:

$$\frac{\partial E_D}{\partial d} = Z_d = \frac{1}{2} \left[\frac{\sigma_{12}^2}{G_{12}^0(1-d)^2} + \frac{\sigma_{13}^2}{G_{13}^0 d_{shear}^2} \right] = \frac{1}{2} [G_{12}^0 (\gamma_{12}^e)^2 + G_{13}^0 (\gamma_{13}^e)^2] \quad 2.13$$

$$\frac{\partial E_D}{\partial d'} = Z'_d = \frac{1}{2} \frac{(\sigma_{22})_+^2}{E_2^0(1-d')^2} = \frac{1}{2} \frac{E_2^0 (v_{12}^e \epsilon_{11}^e + \epsilon_{22}^e)_+^2}{(1-v_{12}v_{21})^2} \quad 2.14$$

The damage evolution functions over time t are defined as:

$$Y(t) = \text{Sup}_{\tau \leq t} \sqrt{Z_d(\tau) + b Z'_d(\tau)} \quad 2.15$$

$$Y'(t) = \text{Sup}_{\tau \leq t} \sqrt{Z'_d(\tau)} \quad 2.16$$

for shear and transverse damage respectively.

The damage values d and d' are calculated in two different ways, by using linear or exponential functions, the formers take the following forms:

$$d = 0 \quad \text{if } Y(t) < Y_0 \quad 2.17$$

$$d = \frac{(Y(t) - Y_0)_+}{Y_c} \quad \text{if } d < d_{max}, Y'(t) < Y'_s \text{ and } Y(t) < Y_R \quad 2.18$$

$$d = 1 - (1 - d_{max}) \frac{Y(t - \Delta t)}{Y(t)} \quad \text{else} \quad 2.19$$

$$d' = 0 \quad \text{if } Y(t) < Y'_0 \quad 2.17$$

$$d' = \frac{(Y'(t) - Y'_0)_+}{Y'_c} \quad \text{if } d' < d'_{max}, Y'(t) < Y'_s \text{ and } Y(t) < Y_R \quad 2.18$$

$$d' = 1 - (1 - d'_{max}) \frac{Y'(t - \Delta t)}{Y'(t)} \quad \text{else} \quad 2.19$$

Where one has to define the initial and critical shear damage limits Y_0 and Y_c , the initial and critical transverse damage Y'_0 and Y'_c , the brittle transverse damage limit of the fibre-matrix interface Y'_s , the elementary shear damage limit Y_R and finally the maximum allowed value for damage d_{max} .

Alternatively, exponential functions can apply for modelling damage evolution that is not linear and for which a best fit straight line is difficult to get. In this case the two damage functions take the following form:

$$d = d_{sat1} \left(1 - e^{-\frac{Y_0 - Y(t)}{Y_c}} \right) \quad \text{if } Y(t) > Y_0 \quad 2.20$$

$$d' = d_{sat2} \left(1 - e^{-\frac{Y'_0 - Y'(t)}{Y'_c}} \right) \quad \text{if } Y'(t) > Y'_0 \quad 2.21$$

$$d = d' = 0 \quad \text{else} \quad 2.22$$

2.2.3 Matrix plasticity

If plasticity is calculated using the true elastic strains. The elastic strain is considered like total strain minus plastic strain. A general anisotropic Hill-type plasticity criterion is introduced to allow the plastic strain calculation by an iterative algorithm. The yield function is given by:

$$f(\tilde{\sigma}, R) = \sqrt{\left[\frac{\sigma_{12}}{1-d} \right]^2 + a^2 \left[\frac{(\sigma_{22})_+}{1-d'} + \frac{(\sigma_{22})_-}{1-d'} \right]^2} - R(\varepsilon^p) \quad 2.23$$

The hardening law is isotropic and depends only on the effective plastic strain ε^p :

$$R(\varepsilon^p) = R_0 + \beta(\varepsilon^p)^m \quad 2.24$$

where R_0 is the initial yield stress β is the hardening law multiplier m is the hardening law exponent. A coupling factor a^2 between shear and transverse plastic strains is also introduced. Generally, this factor is equal to the theoretic value of 0.33 for initially isotropic resin based matrix materials, as indicated by Johnson et. al. [10].

2.3 Waas-Pineda progressive damage model

The Waas-Pineda (WP) model is a progressive damage and failure model developed for fibre-reinforced composite/laminate materials. The model uses multiple Internal State Variables (ISVs) for modelling the effects of this damage and failure. Originating from the Schapery theory of thermodynamic approach to material degradation [13-15], this model makes use of the crack band formation theory by Bazant, Oh [16] to define the internal position and orientation of cracks based on conventional failure theories, and then computes the localised faults inserting them in the continuum of the material characteristic. A description of the model and validation for notched laminates is found in [17-18], while the implementation in VPS code is detailed hereafter and taken from [19].

The result is that a softening material with negative tangent stiffness is allowed to exist and the equilibrium is guaranteed, and the cracks are treated as discontinuities where a cohesive-like zone exists, while the surrounding remains as a continuum. This method allows to effectively treat a material where multiple cracks coexist, precisely like a composite would behave.

The model implemented in the software has a slightly modified formulation compared to the paper from Waas and Pineda, but maintains the basic framework, it utilizes the continuum elastic behaviour of Ladevèze with plasticity and adds the transition to cohesive fracture and adds post-failure regimes to simulate the effects of mode I transverse matrix cracking, mode II shear matrix cracking and mode I fibre failure. These failure modes are found to be consistent with those observed in polymer matrix composites.

It was postulated by WP that the evolution of the failure mechanisms leads to a negative (local) tangent stiffness; subsequently, initiation criteria are required. The transition from the continuum state to the cohesive state is triggered by a failure criterion; the trigger levels of strain or stress are detailed in the failure model input data.

Stress and strain based criteria can be chosen for the axial fibre and transverse/matrix behaviours. In the cohesive state, the stress-strain relations are replaced by traction-separation laws. Once the maximum degradation (damage) is reached a post-damage state is entered in order to ensure a limitation in transferable stresses.

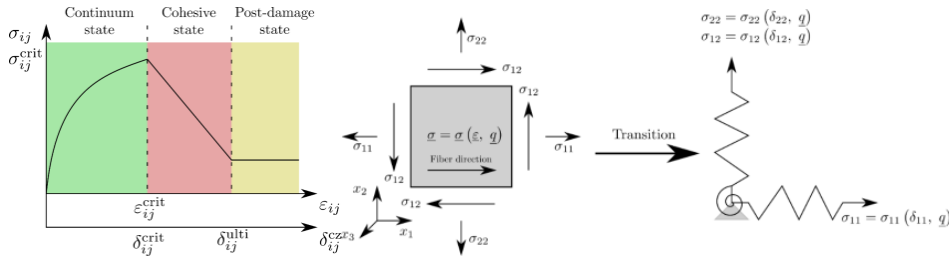


Figure 2.2 – Schematisation of the WP model localisation method, with continuum, cohesive and post-damage states.

2.3.1 Initiation

The switch from a continuum-based stress-strain relation to a cohesive traction-separation law is based on the criteria specified in the following equations, which use criteria for axial, transverse and shear straining:

$$\left(\frac{\epsilon_{11}^e}{X_T} \right)^2 \geq 1 \quad ; \quad \text{for } \epsilon_{11}^e > 0 \quad 2.25$$

$$\left(\frac{\epsilon_{22}}{Y_T} \right)^2 + \left(\frac{\gamma_{12}}{Z_{12}} \right)^2 = 1 \quad ; \quad \text{for } \epsilon_{22} > 0 \quad 2.26$$

$$\left(\frac{\varepsilon_{22}}{Y_C}\right)^2 + \left(\frac{\gamma_{12}}{Z_{12}}\right)^2 = 1 \quad ; \quad \text{for } \varepsilon_{22} < 0 \quad 2.27$$

where X_T is the maximum allowable axial strain in the lamina, aligned with the fibre orientation, Y_T is the maximum allowable strain in tension in the direction transverse to the fibre orientation, Y_C is the equivalent in a compressive deformation mode in this transverse direction, Z_{12} is the shear failure strain. The switch from a continuum-based stress-strain relation to a cohesive traction-separation law can also be achieved using criteria for axial, transverse and shear stressing of the material, the equations are analogous to the 2.25 to 2.27, where strain are substituted with the equivalent stresses.

Once the material has satisfied any of the criteria specified above, a cohesive crack is assumed to exist in the material continuum at that location and the continuum approach is superseded by traction versus separation laws. The crack tip opening displacements, $\delta_{11}, \delta_{12}, \delta_{22}$, are related to the straining of the material through the WP fibre and matrix characteristic lengths, lc_f, lc_m , using the following relations:

$$\delta_{11} = lc_f (\varepsilon_{11}^{total}) \quad 2.28$$

$$\delta_{22} = lc_m (\varepsilon_{22}^{total} - \varepsilon_{22}^{pl}) \quad 2.29$$

$$\delta_{12} = lc_m (\gamma_{12}^{total} - \gamma_{12}^{pl}) \quad 2.30$$

where $\varepsilon_{11}^{total}, \varepsilon_{22}^{total}, \gamma_{12}^{total}$ are the total straining behaviours, and $\varepsilon_{22}^{pl}, \gamma_{12}^{pl}$ are the respective plastic strains in those orientations.

The characteristic element lengths lc_f and lc_m introduced above are respectively the line running parallel to the fibre direction that intersects the element edges and the length obtained by a line running perpendicular to the fibre direction that intersects two element edges, as in the example below.

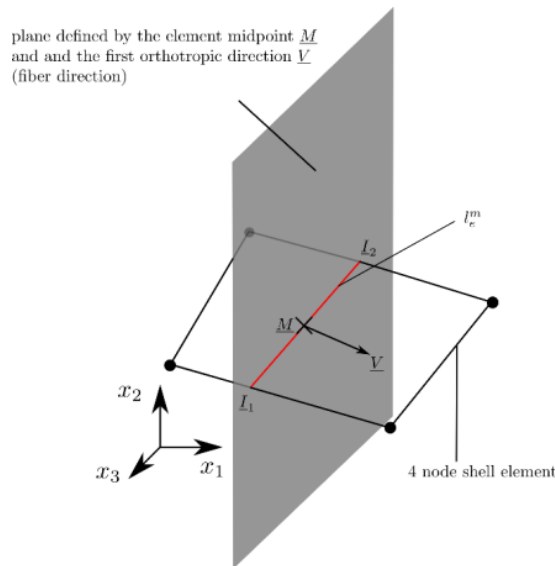


Figure 2.3 – Determination of the characteristic element length for localised fracture modelling.

The stiffnesses, K_{11} , K_{22} , and K_{12} of the cohesive region are derived relating the characteristic failure lengths and the stress response σ_{ij}^t from the previous time increment, using the following equations:

$$K_{11} = \left| \frac{\sigma_{11}^t}{\delta_{11}} \right| ; \quad K_{22} = \left| \frac{\sigma_{22}^t}{\delta_{22}} \right| ; \quad K_{12} = \left| \frac{\tau_{12}^t}{\delta_{12}} \right| \quad 2.31$$

$$K_{ij} = \begin{cases} \frac{\sigma_{ij}^0}{\delta_{ij}^0} , & \delta_{ij}^0 \neq 0 \\ \frac{E_{ij} \text{ or } G_{ij}}{lc_j} , & \text{else} \end{cases} \quad 2.32$$

Here, σ_{ij}^0 is the stress at damage initiation, and E_{ij} and G_{ij} are the elastic moduli for the individual stress components. The initial crack separations thresholds, $\delta_{11}^0, \delta_{22}^0, \delta_{12}^0$ are calculated using the cohesive stiffnesses and related displacements.

Finally, the cohesive stress response associated to the crack openings is derived logically in the following expressions:

$$\sigma_{ij} = \begin{cases} K_{ij} \delta_{ij} , & \delta_{ij} < \delta_{ij}^0 \\ (1 - D_j) K_{ij} \delta_{ij} , & \delta_{ij}^0 \leq \delta_{ij} < \delta_{ij}^{fail} , D_j < D_{max} \\ \sigma_{ij}^{res} , & \text{else} \end{cases} \quad 2.33$$

where δ_{ij}^0 and δ_{ij}^{fail} are the separations at damage initiation and total failure and D_j is the accumulated damage.

2.3.2 Fibre damage

The scalar fibre damage parameter D_1 takes the form that gives the typical cohesive stress shape, and is given by:

$$D_1 = \frac{\delta_{11}^f (\delta_{11} - \delta_{11}^0)}{\delta_{11} (\delta_{11}^f - \delta_{11}^0)} \quad 2.34$$

where the separation at total failure is determined by the associated fracture energy G_{IC} as:

$$\delta_{11}^{fail} = \frac{2G_{IC}}{|\sigma_{11}^0|} \quad 2.35$$

2.3.3 Matrix damage

Similarly, the calculation of the matrix damage incorporates the definition of an effective separation and ensuing cohesive stress generation. The effective stress is calculated as follows:

$$\sigma_{eff}^i = \sqrt{(\sigma_{22}^i)^2 + (\tau_{12}^i)^2} \quad 2.36$$

introducing the mixed-mode loading ratio:

$$\beta = \left| \frac{\delta_{12}}{\delta_{22}} \right| \quad 2.37$$

One can rearrange and write the following relations:

$$\delta_{22} = \frac{\delta_{22,12}^{eff}}{\sqrt{1 + \beta^2}} \quad 2.38$$

$$\delta_{12} = \frac{\beta \delta_{22,12}^{eff}}{\sqrt{1 + \beta^2}} \quad 2.39$$

Subsequently, the effective separation at damage initiation δ_{eff} becomes:

$$\delta_{eff} = \begin{cases} \delta_{22} \delta_{12} \sqrt{\frac{1 + \beta^2}{(\delta_{12})^2 + (\beta \delta_{22})^2}} & ; \delta_{22} \neq 0 \\ \sqrt{(\delta_{12})^2} & ; \delta_{22} = 0 \end{cases} \quad 2.40$$

Subsequently, the mixed separation at failure δ_{mixed}^{fail} is:

$$\delta_{mixed}^{fail} = \frac{2 \left\{ GIC_{22} - (GIC_{22} - GIC_{12}) \left[\frac{\beta |\tau_{12}|}{(|\sigma_{22}| + \beta |\tau_{12}|)} \right]^\eta \right\}}{\sigma_{eff}} \quad 2.41$$

where $GIC22$, $GIIC12$ are energy release rates associated to those specific fracture modes and η is a calibration parameter that can be derived from testing at different mixed mode ratios. By putting respectively $\delta_{22} = 0$ and $\delta_{12} = 0$ one comes to the simplified relations:

$$\begin{aligned}\delta_{eff} &= |\delta_{12}| \\ \delta_{mixed}^{fail} &= \frac{2(GIIC12)}{Z_{12}}\end{aligned}\quad 2.42$$

These initial and failure separations can then be used to evaluate the damage D_2 using values stored from onset, failure and the previous time t :

$$D_2 = \frac{\delta_{mixed}^{fail} (\delta_{eff}^t - \delta_{eff}^0)}{\delta_{eff}^t (\delta_{mixed}^{fail} - \delta_{eff}^0)}\quad 2.43$$

The values of damage calculated as D_1 , D_2 can then be used directly to compute the cohesive stresses cycle to cycle using the following relation, as introduced previously.

2.3.4 Post-damage state

A maximum damage parameter D_{max} is used to define the residual stresses that can be transferred in the post-damage state, it is not related to the cohesive damage, but simply follows these criteria, for fibre and matrix respectively:

$$\left(1 - \frac{|\sigma_{11}|}{\sigma_{11}^0}\right) \geq D_{max}\quad 2.44$$

$$\left(1 - \frac{|\sigma_{eff}^t|}{(\sigma_{22}^0)^2 + (\sigma_{12}^0)^2}\right) \geq D_{max}\quad 2.45$$

The transition to the post-damage state is accomplished individually for fibre and matrix damage when the corresponding criteria is met.

2.4 Cohesive zone model

Delamination is one of the most critical causes of failure in laminated composite structure. It results in the separation of two adjacent plies, leading to the propagation of an inter-laminar crack. These are caused by the low through-thickness shear and tensile properties in the resin rich areas found between plies in laminated structures. Because delamination failures cause rapid interface crack propagation, failure models are generally based on fracture mechanics concepts rather than conventional stress based failure models. In the finite element method, the cohesive elements approach is often used to model such cracks. Interface elements are then defined between the finite elements representing the plies, idealized using interface spring elements that transmit traction normal and shear forces

between adjacent plies. Software implementation of the cohesive zone modelling is taken from Johnson, Pickett [20] and Greve, Pickett [21].

Essentially, the interface spring elements represent mechanical stiffness, strength and fracture energy absorption of the interface using an idealized stress-displacement response, where the out-of-plane mode I (traction) generally assumed as:

$$\sigma_{33} = k_3(1 - d_3)u_3 \quad 2.45$$

governed by the evolution of damage parameter d_3 and relating the interface normal stresses with the displacement. In the most simple case, the particular equation for damage evolution has the form:

$$d_3 = \frac{u_{3m}(u_3 - u_{30})}{u_3(u_{3m} - u_{30})} \quad 2.46$$

Where with subscript 30 and 3m we indicate the initial and ultimate displacement for damage. It can be verified that with this particular choice of damage function, the stress-displacement function has the triangular form shown in figure below. From this example, it is clear that the function $d_3(u_3)$ can be expressed in terms of σ_{3m} and G_{IC} by:

$$u_{30} = \sigma_{3m} / k_3 \quad 2.46$$

$$u_{3m} = 2G_{IC} / \sigma_{3m} \quad 2.47$$

Having shown that G_{IC} represents the fracture energy of the particular interface fracture mode.

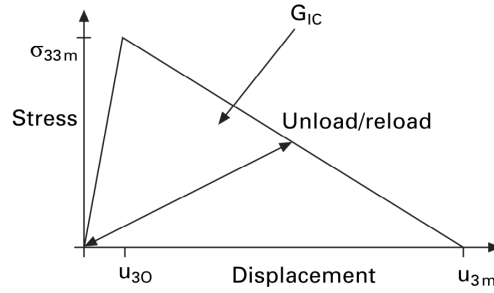


Figure 2.4 – Idealised mode I interface stress displacement function.

The same applies to the Mode II (shear) type of interface, where the fracture energy, typically indicated with G_{IIC} is dissipated in shearing mode between two displacement limits u_{130} and u_{13m} , the maximum interface stress is in this case τ_{3m} .

In the general loading case, there will be a mixture of modes at the interface, and the coupling of modes can differ from the linear case, and usually represented by an envelope defined by:

$$\left(\frac{G_I}{G_{IC}}\right)^\eta + \left(\frac{G_{II}}{G_{IIC}}\right)^\eta = 1 \quad 2.48$$

where $\eta=1$ for linear and $\eta>1$ for nonlinear interaction. Typical values for η are between 1 and 2. In VPS the nonlinear interaction defined via an empirical curve function defined as $G_{cont} = f(\theta)$ valid between 0 and 90°:

$$G_{cont} = f(\theta);$$

$$a \cos \left(\frac{G_i^{II}}{\sqrt{G_i^{I^2} + G_i^{II^2}}} \right) = \theta \quad 2.49$$

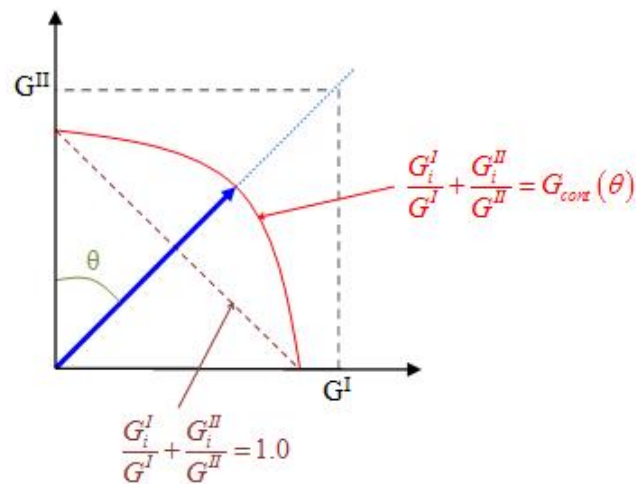


Figure 2.5 – Graphical representation of mixed mode interface fracture toughness.

The values of G_{Ic} and G_{IIc} are obtained from the standard Mode I Double Cantilever Beam (DCB) and Mode II End Notched Flexure (ENF) tests respectively. Also, coupling for mixed mode critical fracture toughness can be determined using the Mixed Mode Bending (MMB) test.

2.5 Building block approach

The structures and materials considered in this work are thin-walled structures made of plies with continuous unidirectional fibres embedded in a polymer matrix. The design of structural composites for advanced applications is nowadays conducted with computers and numerical tools. We typically distinguish two disciplines: the computer aided design (CAD) used to define the overall geometry of the part, the laminates with their optimal stacking sequences, to which follows the computer aided engineering (CAE), to analyse the structural integrity of the composite structure when subjected to the expected loads. Here, the information on damage, failure, and subsequent material behaviour obtained from simple coupon level tests are used as input to predict the structural behaviour of more complex structures and geometries. In order to have continuously predictive numerical models, the validation should be consistent at each increasing level of complexity. This methodology described with the

pyramid concept is the key foundation of the Building Block Approach (BBA) [22–23]. The idea is to build the knowledge on the material and structural behaviours step by step, starting from the fundamental stage at the coupon level up to the full-scale assembly. Graphically represented in Figure 2.6 with an exemplar case of a wing structure for airplane [24], this approach is a pyramid, where at the bottom the largest number of tests is performed, while they are reduced to few significant ones going up towards the complete structure.

The BBA ensures that cost and performance objectives are met by testing greater numbers of smaller and less expensive specimens and building on the knowledge acquired at a given level of structural complexity before progressing to a level of more complexity.

There is a close relation between experimental tests and numerical simulations: the experimental tests described in chapter 2 are used to define a reliable test procedure and this test procedure is reproduced numerically in a finite element environment to validate the predicting capabilities of the virtual environment.

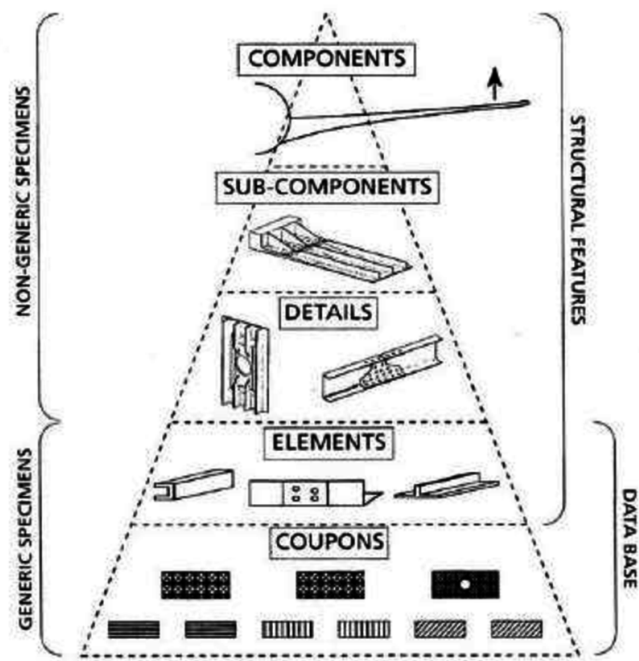


Figure 2.6 – Building block approach schematic pyramid.

It has been observed over the years that simulation, and especially models based on the finite element method, are more and more used on the different stages of the pyramid, therefore becoming an important companion of the physical tests. In addition, repeating tests for different material configurations (e.g. different stacking sequences, varying geometrical features, thicknesses, etc.) or when small changes in the components geometry are studied, will result in expensive and time-consuming efforts, that could be avoided by efficient and robust numerical tools.

Developing predictive simulation tools is clearly a challenge. The simulation tools should be able to address different attributes, covering static or quasi-static analyses, damage analyses, fatigue, dynamic response, crash, etc.

In the body of this work, we will concentrate on the first levels of the BBA, regarding coupon level experimental tests, and simulations to replicate basic loading conditions, then perform validation on a higher level through the simulation of a crush element with simple geometry. The simulation should replicate the crushing behaviour observed in the experimental case, with particular attention to the energy absorption levels, the crush force, and the shape of the crushed elements.

CHAPTER 3

EXPERIMENTAL CAMPAIGN

In these pages, we present an in-depth description of the experimental tests performed for the crash analysis of CFRP. A detailed description of each test executed is included, along with the necessary post-processing of results and discussion of the data reduction methods used. Finally, the case load for validation is introduced and described with its test results.

3.1 Materials and methods

For the object study, a prepreg material with high toughness epoxy resin is used. The UD tape chosen is made of 12k T700 carbon fibre with areal weight of 150gsm and a high toughness epoxy resin with standard glass transition temperature. The reason for using a prepreg material is the relative ease of manufacturing different plates and specimens of varying thickness, layup and size, without the need of additional and expensive equipment.

The prepreg comes in a roll tape 600mm wide and is stored in a refrigerator at -20°C. Upon used, it is left to warm to room temperature for a couple hours before proceeding to cutting. The plates are then manufactured within 8 hours, and the leftover roll is put back to freeze. Care is taken to minimise moisture build-up on the material, which is always stored in a plastic bag.

Cure of the epoxy was done in autoclave under vacuum bag and added 6bar absolute pressure, and the thermal cycle followed the supplier's prescription of 90 minutes at 120°C, heating and cooling rates of 3°C per minute were imposed to have controlled resin flow for the lowest void content, and avoid distortions due to residual internal stresses.

In order to evaluate the consistency of the curing process and of the mechanical properties under investigation, fibre weight and volume fraction of each manufactured plate was evaluated by extracting a sample from a central region of the plate, and following the procedure described by Giorgini, Mazzocchetti et. al. [25]¹ examined by thermal degradation of the resin using thermogravimetric analysis. The fibre weight fraction measured using this method was close to 64,2% for most unidirectional plates, but one larger cross-ply plate showed a figure as low as 59,7%; these values correspond to 55.2% and 50,4% volume fractions respectively. As a quick comparison, these were compared with density measures

¹ Thanks to the colleagues at the department of industrial chemistry for the technical contribution and the use of equipment.

using Archimedes' principle, though this procedure results in a lower precision, the values are in agreement with TGA procedure. To complete the physical assessment of the manufacturing process, the cured ply thickness (CPT) of each plate was also obtained, and an average value defined for normalisation of lamina properties and numerical simulations.

Most lamina level tension and compression strength and modulus properties were normalized according to nominal cured ply thickness. Excluded from the normalisation procedure were 90° tensile and compressive strength and modulus, in-plane shear strength and modulus, and Poisson's ratio. The following normalization formula was used [26]:

$$\text{Normalized Value} = \text{Measured Value} \times \text{Measured CPT} / \text{Nominal CPT.}$$

The average cured ply thickness of 0.15375 mm has been used as the nominal CPT for normalization purpose. After normalizing, data scatter reduced or remained the same.

Glass transition temperature was measured by DSC after cure of each plate batch, values varied between 96 and 102°C and no appreciable residual enthalpy is found, as indication of good and repeatable processing procedure. A comprehensive summary of manufactured plates with their physical properties is reported in Table 4-1.

All samples are cut to desired dimensions using a diamond disk saw, and edges are polished with grind paper where required.

Table 3.1 – Overview of cured plates for mechanical and crush tests.

Plate #	Layup	Plate dimension (mm)	CPT (mm)
T1-1610	[0]8	150x250	0,1531
T90-1610	[90]16	150x250	0,1532
S1-1611	[+45/-45]4s	250x300	0,1542
C1-1610	[0]20	120x200	0,1536
C90-1611	[90]20	120x200	0,1536
D12-1612	[0]12s	250x300	0,1542
Crush-1612	[0/90]3s	200x300 (corrugated)	0,1542
CT-1707	[90/0]4s	250x300	0.1538

3.2 Mechanical tests

Here are reported in detail the tests performed to build the numerical models for damaging material, as described in the previous chapter. The report follows the logical order described by the building block approach, going from the easiest tests for the base lamina properties, to the more complex ones used for damage modelling.

3.2.1 Static tensile

The first test described is the tensile loading on fibre direction. As reported in Table 4-1, a plate with [0]8 layup is produced and specimens cut to desired dimensions according to ASTM D3039 standard [27]. Aluminium tabs are glued to the specimens' ends to guarantee

the correct load transfer, without damaging the material thus invalidating the trial. An epoxy glue is chosen, verifying that the shear loading was within safe limits for the expected point of failure of the UD material. Loading is carried out in displacement control at 2mm/min rate until ultimate failure. All specimens failed abruptly in brittle manner without any appreciable softening in the stress-strain curve. All specimens are instrumented with an axial extensometer to compensate for the compliance of the loading chain, while some are additionally fitted with double grid strain gages to measure both longitudinal and transverse strains simultaneously: this allowed a more precise measurement for elastic modulus and the Poisson's ratio. Below a summary of the test results.

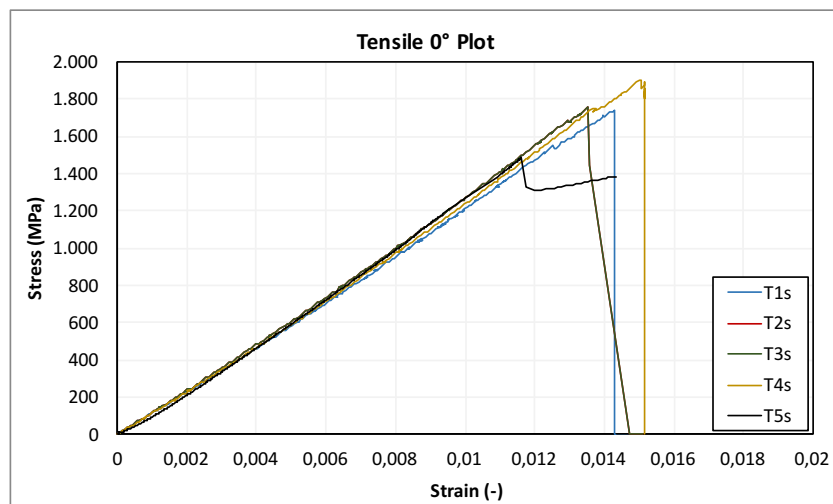


Figure 3.1 - Tensile test 0° test report

Table 3.2 - Tensile test 0° data report

Specimen	Test Data					CPT Normalized		
	Thickness (mm)	Ply Thickness (mm)	Failure stress (MPa)	Failure strain	Tensile Modulus (Gpa)	Failure stress (MPa)	Failure strain	Tensile Modulus (Gpa)
T1s	1,215	0,1519	1643	0,0131	133	1624	0,0124	131
T2s	1,28	0,16	1730	0,0142	131	1801	0,0132	137
T3s	1,325	0,1656	1756	0,0135	130	1891	0,0135	140
T4s	1,329	0,1662	1904	0,015	130	2058	0,0146	141
T5s	1,294	0,1618	1597	0,0118	127	1680	0,0126	133
T6s	1,095	0,1368	1948	0,0127	147	1734	0,0132	131
Average	1,256	0,1571	1763	0,0135	130,2	1798	0,0133	135,5

Poisson's modulus obtained from the coupled readings of longitudinal and transverse strain gage give a value close to 0,3. It is interesting to notice how this value oscillates during the loading: after a brief initial oscillation due to sensibility of the measuring device, the measurements quickly stabilize and increases from 0,28 at low strains to a peak of 0,31 at about 0,3% strain, after this point, the ratio decreases down to 0,29 at 1,3% strain when rupture occurs. A graphical representation can be appreciated in the picture below.

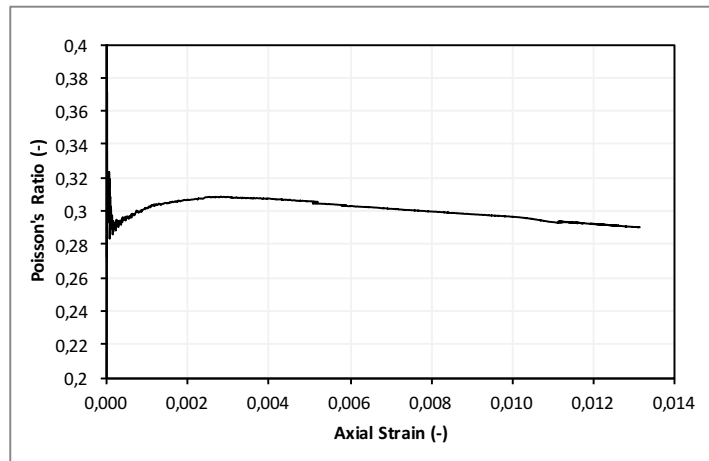


Figure 3.2 – Value of Poisson's ratio versus strain for tensile test at 0°.

In transverse direction, the same tensile tests just described are performed, with plies aligned orthogonally to the loading axis, in the 90° direction. The test geometry was slightly different, with specimens consisting of 16 plies and 15mm width. The discontinuous nature of the 90° plies makes it harder to achieve a consistent stress at failure, hence the severe differences in strength of the three repetitions (see Table 3.3). The aim of this test was mainly to identify the elastic modulus in transverse direction, which is measured at 14,5GPa average.

Table 3.3 – Tensile test 90° data report

Specimen	Thickness	Ply Thickness (mm)	Failure stress (MPa)	Tensile Modulus (GPa)
T90_1	2,475	0,155	22	13,8
T90_2	2,490	0,156	30	16,1
T90_3	2,443	0,153	57	13,6
Average	2,470	0,154	36	14,5

3.2.2 Static compressive

In this test, the specimen is loaded in compressive fashion in a specific fixture as described in the ASTM D3410 standard [28]. The test allows to define the compressive elastic modulus in fibre direction, which for CFRP is typically lower than the tensile modulus. Specimens measure 155mm length by 10mm width, and tabs are applied to both ends to efficiently transfer the load, as prescribed by the ASTM standard, and are loaded in displacement control at 1.5mm/min rate.

One specimen is instrumented using two strain gages in a back to back configuration in order to evaluate the bending of the specimen during loading and up to failure, the standard does not require that all specimens are instrumented, once the setup is verified not to introduce excessive bending upon loading. Total bending measured by the strain gages must be within +/-10% until failure:

$$\%B = 100 \frac{\varepsilon_{11 \text{ front}} - \varepsilon_{11 \text{ back}}}{\varepsilon_{11 \text{ front}} + \varepsilon_{11 \text{ back}}} \quad 3.1$$

This requirement is verified for the two tests instrumented with strain gages, as shown in the picture below.

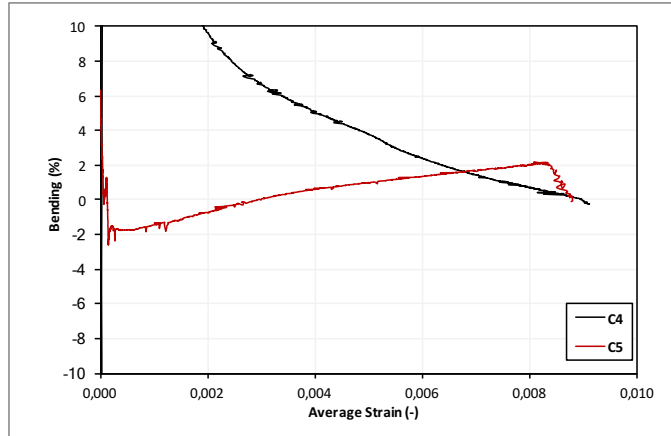


Figure 3.3 – Percentage bending versus strain for compressive tests at 0°.

The elastic modulus E_{11} under compressive loading is calculated from the two instrumented tests using the chord method between 0,1 and 0,3% strain, the average between front and back strain measures is used for the calculation. A summary of test results is found in Table 3.3.

Table 3.4 – Compressive test 0° data report

Specimen	Thickness (mm)	Test Data				CPT Normalized		
		Ply Thickness (mm)	Failure stress (MPa)	Failure strain	Compr. Modulus (GPa)*	Failure stress (MPa)	Failure strain	Compr. Modulus (GPa)
C2	3,067	0,153	631			630		
C3	3,060	0,153	728			724		
C4	3,044	0,152	737	0,0092	84,1	729	0,0091	83,2
C5	3,022	0,151	869	0,0100	83,8	854	0,0098	82,3
C6	3,004	0,150	682			667		
C7	2,989	0,149	724			704		
Average	3,04	0,152	729	0,0096	83,9	721	0,0094	82,8

* Chord moduli calculated between strain 0,001 and 0,003.

Compressive modulus under compression loading shows a slight reduction with increasing strain, due to local micro-buckling effects. For this reason, the chord modulus calculated between a wide strain range is not acceptable for computational purposes, for this reason, the local tangent modulus is fitted using this analytical expression:

$$E_C = \frac{E_{0C}}{1 + \gamma E_{0C} |\varepsilon_{11}|} \quad 3.2$$

Where the two unknowns E_{0C} and γ are found through a least square fit method, values are

$E_0 = 87 \text{ GPa}$ and $\gamma = 0,27 \text{ GPa}^{-1}$. A graphical representation of the analytical curve is shown in the figure below.

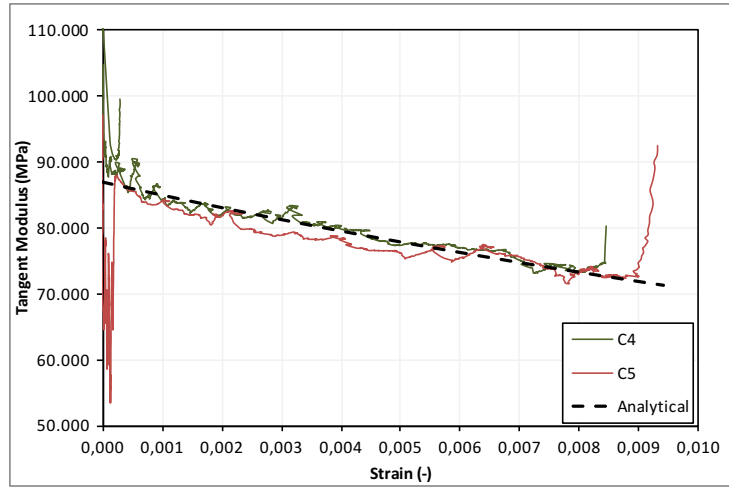


Figure 3.4 – Tangent modulus softening vs. axial strain.

3.2.3 Static in-plane shear

This test should be considered only as a preliminary load before the following cyclic tensile tests. Geometry and layup of the specimens are chosen following ASTM D3518 standard [29], and are 250mm length by 25mm width and [+45/-45]_{4s} layup for a final thickness of 2.48mm. Nevertheless, this trial was reputed useful to determine the onset of matrix plasticisation, as well as to give an indication for the ultimate failure load of this particular geometry.

From the constitutive law, the stress-strain relation for the given layup is simplified as following:

$$\begin{pmatrix} \sigma_{11} \\ \sigma_{22} \\ \sigma_{12} \end{pmatrix} = \begin{pmatrix} 0 \\ 0 \\ \sigma_L/2 \end{pmatrix} \text{ and } \begin{pmatrix} \varepsilon_{11} \\ \varepsilon_{22} \\ 2\varepsilon_{12} \end{pmatrix} = \begin{pmatrix} 0 \\ 0 \\ \varepsilon_L - \varepsilon_T \end{pmatrix} \quad 3.3$$

Where subscript L and T indicate the longitudinal and transverse direction with respect to the specimen loading axis. Acquired data from this test are load, displacement, and deformation from longitudinal and transverse extensometers.

This particular configuration exhibit extensive softening throughout the whole loading path, as can be seen from Figure 3.x, so attention must be taken to identify the shear modulus. The ASTM standard suggests calculating the chord modulus in a shear range between 2000 μ and 6000 μ , but in our tests, the specimens show a significant softening already at the 6000 μ limit, so this range was reduced to exclude this region, as can be seen in the figure below. Our modified calculations give an average shear modulus of 3.95GPa (+/-3.1%) which is considered an acceptable value for this category of material. With this modulus, offset shear strength at 0.2% strain is found at 43.6MPa (+/-3.8%) average.

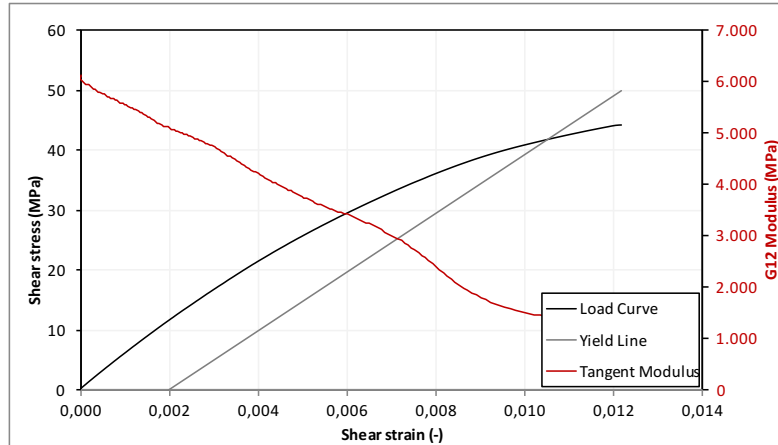


Figure 3.5 – Shear tensile test detail: Tangent modulus and Yield stress.

3.2.4 Cyclic in-plane shear

This consist in loading and unloading at constant rates with increasing ultimate stress level until failure. The goal is to obtain a number of points sufficient for interpolation of damage function, but not elevated to induce low cycle fatigue phenomena; a typical target value is 5-6 cycles. Thanks to the information gained in the simple test, the first cycle was set to achieve a 45MPa shear stress ($\sigma_{12} = P/2A$) and increasing 5MPa with each cycle until failure. These stresses are converted to loads to provide useful input to the test machine, real stresses are then recalculated using the actual specimen cross-section dimensions. Load rates are controlled at 2kN/min in both ascending and descending directions.

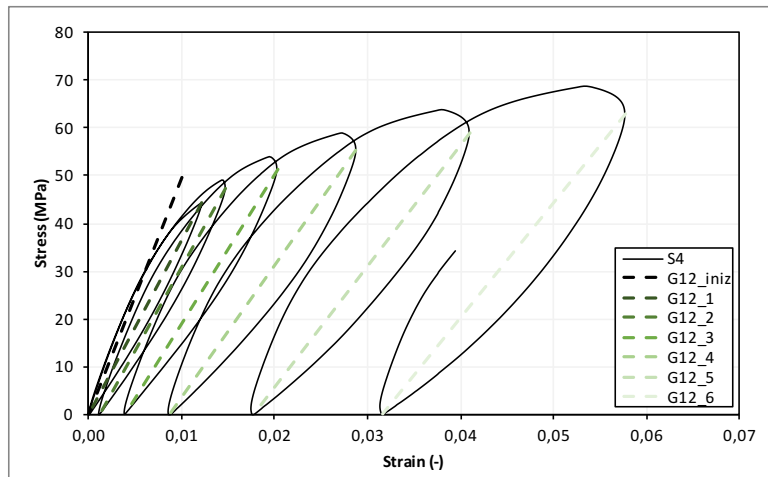


Figure 3.6 – Cyclic shear tensile test with interpolated damaged elastic moduli.

From this test curve, we derive the shear modulus reduction (related to the shear damage parameter) and the residual strain (plasticity). The material behaviour is highly nonlinear, so we have to pay attention when measuring the elastic property of the material. Since the specimen accumulates plastic deformation upon loading, the shear modulus is calculated during the unload path as the secant line (chord method) passing through the strain inversion

point after P_{max} and the point at zero load at the end of the unload path. It is also noticeable in Figure 3.6 that when the specimen has accumulated high plasticity, it passes through points of non-equilibrium, evidenced by the negative tangent modulus. This phenomenon is attributed to the plasticity effects being time-dependent, because they increase in magnitude when testing at lower speeds. A time-dependent material formulation is not being investigated in this work, so these considerations should be considered purely qualitative.

Table 3.5 – Cyclic shear tensile test, example of model test data points collected for further elaboration.

Points	time (mm:ss)	Stress (MPa)	Strain (-)	G_{12} (MPa)
1	01:41	48,4	1,38E-02	
2	02:32	0,0	1,97E-03	4107
3	04:18	48,5	1,42E-02	
4	05:10	0,0	2,47E-03	4130
5	06:59	53,2	1,75E-02	
6	07:55	0,0	4,09E-03	3969
7	09:54	58,2	2,38E-02	
8	10:54	0,0	8,29E-03	3756
9	13:03	62,9	3,22E-02	
10	14:08	0,0	1,57E-02	3813

From the strain and stress data points collected at each load cycle, the damage behaviour is plotted versus the square root of the damaging strain energy, the conjugate force, driving mechanism of damage evolution according to Ladevèze CDM [6,30].

$$Y_i = \sqrt{\frac{1}{2} G_{12}^0 (2\varepsilon_{12}^{el})^2} = \sqrt{\frac{1}{2} \frac{\sigma_{12}^2}{G_{12}^0 (1 - d_i)^2}} \quad 3.4$$

Where with G_{12}^0 we indicate the undamaged shear modulus and ε_{12}^{el} is the elastic component of the total strain. As described in the previous chapter, the damage mechanism is considered to be *non-healing*, therefore it follows that $Y(T) \geq Y(t)$ for time $T > t$ meaning that in our cyclic loading case, the target values of Y_i are those calculated at the maximum stress at the i^{th} cycle. As we can see from the plot below, although failure occurs at much different loads (67-83MPa), the resultant damage curves of four trials show a relatively narrow scatter.

Regarding the determination of fitting curves necessary to build the numerical model in the FE software, the curves of best fit are determined graphically, paying attention both to interpolation and extrapolation beyond experimental bounds. For the fitting function, we refer to the formulations introduced in the previous chapter. In the table, a comparison between the best fit of linear and exponential functions is compared to the equivalent points obtained through experimental data.

Table 3.6 – Summary of elaborated shear damage parameters, compared to experimental values.

	G_{12} (GPa)	Y_0 (GPa ^{1/2})	Y_c (GPa ^{1/2})	Y_r (GPa ^{1/2})	d_{max}
Experimental		0,0164 *	0,035 *	-	0,511
Linear fit	4,94	0,006325	0,0632	0,0443	1
Exponential fit		0,0111	0,0237	-	0,75

* These values refer to the lowest and highest strain energy values obtained in experimental tests

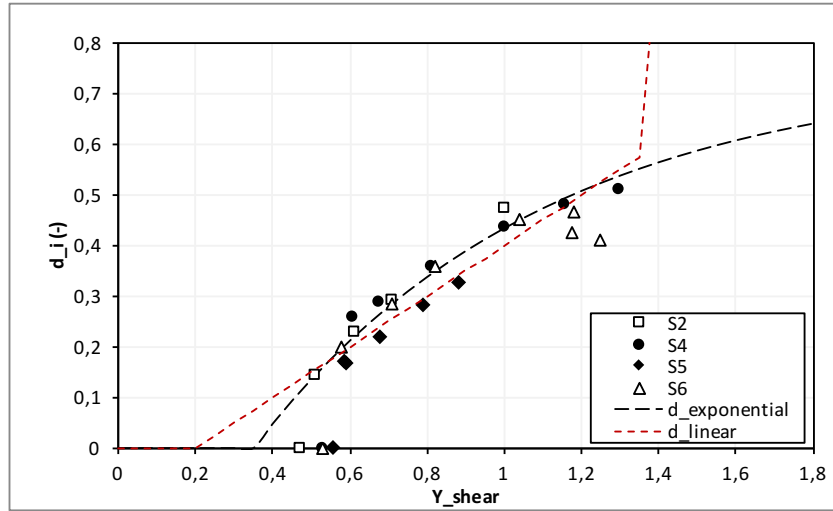


Figure 3.6 – Shear damage vs. conjugate force experimental points, fitting curves imposed for linear and exponential function.

Regarding the plasticity modelling, this is identified by a power law interpolating the plastic stress and the accumulated plastic strain. In particular, p is found by trapezoidal integration between experimental points:

$$p_i = \int_0^{\varepsilon_p^i} (1 - d_{12}^i) d\varepsilon_p = \sum_{j=1}^i \frac{1}{2} \varepsilon_p^j [1 - d_{12}]_{j-1}^j \quad 3.5$$

Where j are the load cycles, ε_p is the plastic strain expressed as total strain minus elastic strain, and by the definition of damage it follows that $d_0 = 0$. The resulting curves are shown in the plot below. In this example, scatter between specimens is wider though the trend is coherent within each repetition, an indication that the reduction method from experimental data is valid. The fitting law, as shown in previous chapter follows a power function of the form $R_i = \beta(p_i)^m$ and R_0 is the yield stress that initiates plasticisation, as determined earlier from static shear tests.

Table 3.6 – Summary of elaborated plasticity parameters, compared to experimental values.

	R_0 (GPa)	Beta (GPa)	m (-)
Numerical	0,0436	0,6	0,59

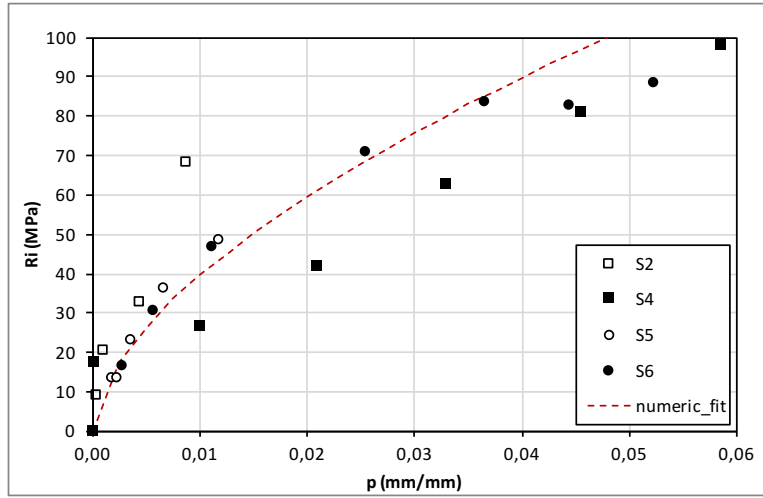


Figure 3.6 – Plastic stress vs. accumulated plastic strain, fitting curve for power law plasticity.

3.2.5 DCB delamination

For delamination fracture toughness, Double cantilever beam and end-notched flexure tests (DCB and ENF) are manufactured from one single plate measuring 250x300mm. A pre-delaminated region is obtained using a thin Teflon insert between two stacks of $[0]_{12}$ plies and the extent is marked using small aluminium tape inserts cured directly on the plate. The final thickness of the specimens was close to 4mm, as prescribed by ASTM D5528 standards [31].

DCB specimens were loaded through loading blocks, the effective pre-cracked length is 50mm from the axis of the loading pins, the overall specimen length is 150mm. The tests are carried out in continuous tensile loading at 3mm/min rate until a sufficient crack propagation is obtained. Load and crack opening displacement, while crack length was obtained by positioning a magnifying camera in front of the specimen and acquiring pictures at 5 seconds interval, spatial resolution is enough to discern crack tip within 0.1mm precision.

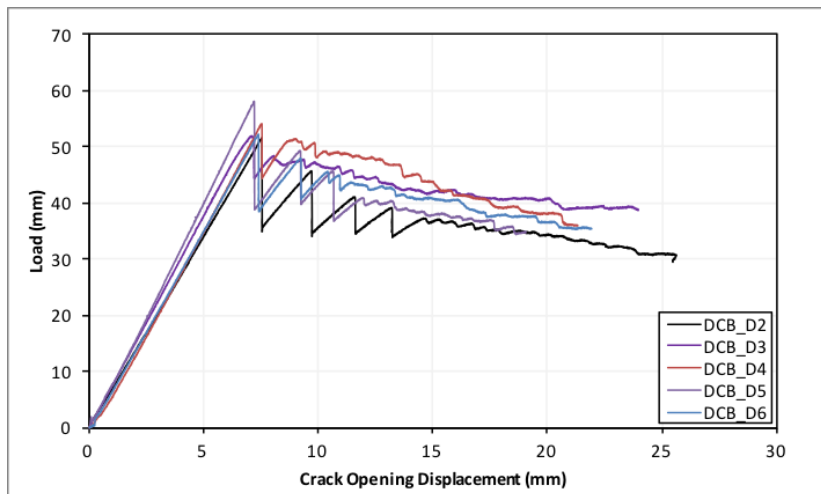


Figure 3.7 – Double Cantilever Beam delamination tests.

Fracture toughness is calculated using different data reduction methods described below. According to the Modified Beam Theory (MBT), the fracture toughness is found by:

$$G_I = \frac{3P\delta}{2b(a + \Delta)} \quad 3.6$$

where P is the load, δ the displacement, b the width and a is the crack length. The correction factor Δ is defined as the offset from the origin of the line interpolating crack length a with the cube root of the compliance: $C^{1/3}$. This factor takes into account for the non-linearity at the crack tip.

Following the Compliance Calibration method (CC), the fracture toughness is identified by:

$$G_I = \frac{nP\delta}{2ba} \quad 3.7$$

where the coefficient n is the slope of the straight line interpolating $\log(C)$ versus $\log(a)$.

Lastly, as for the Modified Compliance Calibration method (MCC), G_I is found by a similar function, and A is the slope of a/h versus $C^{1/3}$.

$$G_I = \frac{3P^2 C^{2/3}}{2Aba} \quad 3.8$$

A comparison between the results obtained with the three methods is presented in the figure below, the methods give comparable results, indicating the reliability of the test.

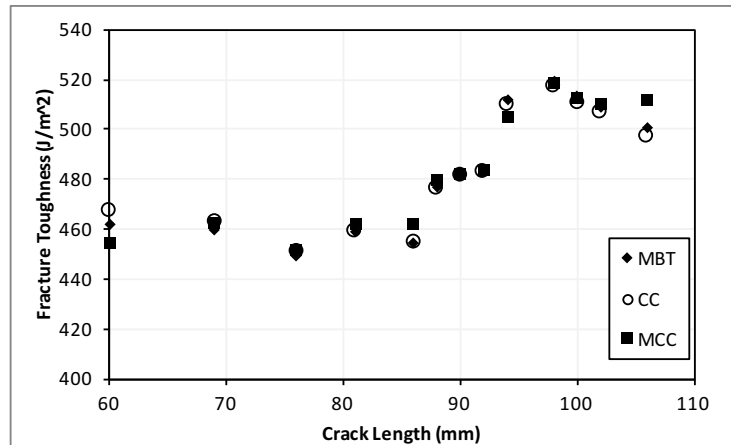


Figure 3.8 – Fracture Toughness of DCB-D2 trial, comparison of different data reduction methods.

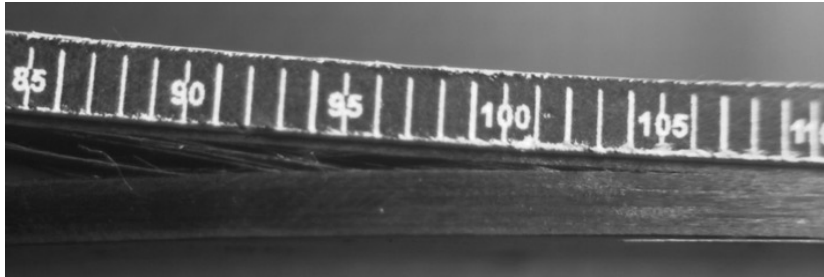


Figure 3.8 – Evidence of fibre bridging at late stage of crack propagation (>40mm).

Data scatter is relatively high, but propagation is stable for the majority of tested samples, with only few showing unstable propagation in the first stages of loading. It must be noted though that the general trend gives an increasing fracture toughness at increasing crack length, this is ascribed to the fibre bridging, intrinsic of the $0^\circ/0^\circ$ interface, in addition, the energy release rate of the first crack advancement should also be discarded, as this might be influenced by the insert used to create the pre-crack. The corrected grand average among all tests give a value of $452\text{J}/\text{m}^2$, the 90% confidence range is $\pm 54\text{J}/\text{m}^2$.

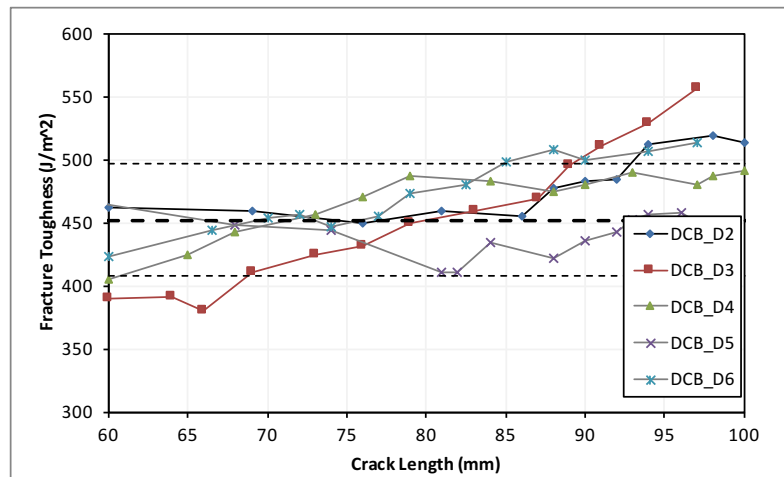


Figure 3.9 – Fracture Toughness variation in DCB test. dashed lines are average value and 90% confidence interval.

3.2.6 ENF delamination

This test consists in loading a pre-cracked specimen in three-point bending configuration using 100mm span length and 1mm/min rate as specified in ASTM D7905 standard [32]. Initial delaminated length is 45mm, and a compliance calibration method is used to identify the fracture toughness. The procedure consists in aligning the specimen to obtain different effective crack length between the lower loading pins, in order: 20mm, 40mm, then 30mm, thanks to a thin paper ruler glued onto the specimen.

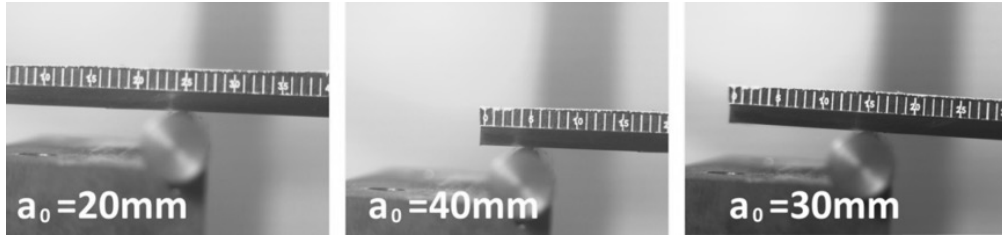


Figure 3.10 – ENF specimen is positioned at different effective crack lengths, thanks to the millimetre scale glued on top of it.

In this status, defined as “non-pre-cracked” (NPC), the specimen is positioned in the first two configuration and loaded within the elastic deformation region, to acquire data for compliance measurement. The last position (30mm crack length) is loaded until crack is advanced, that is, when the tangent stiffness becomes negative. By the multiple measures, the fracture toughness of the interface and the crack advancement are inferred. The full procedure is described in the ASTM standard, here only the essential steps are reported:

$$G_{II} = \frac{3P^2 a_0^2}{2b} \frac{dC}{da^3} \quad 3.9$$

Where a_0 is the crack length before propagation (30mm in this case), b is the specimen width and dC/da^3 is found by linear interpolation of C versus a^3 from the three data points at 20, 30 and 40mm crack length. This additionally allows to calculate the crack length after propagation from:

$$a_{calc} = \sqrt[3]{\frac{C_u - A}{m}} \quad 3.10$$

Where C_u is the compliance of the unloading path in the 30mm test (after crack propagation) A and m are respectively intercept and slope of the $C(a^3)$ line described before.

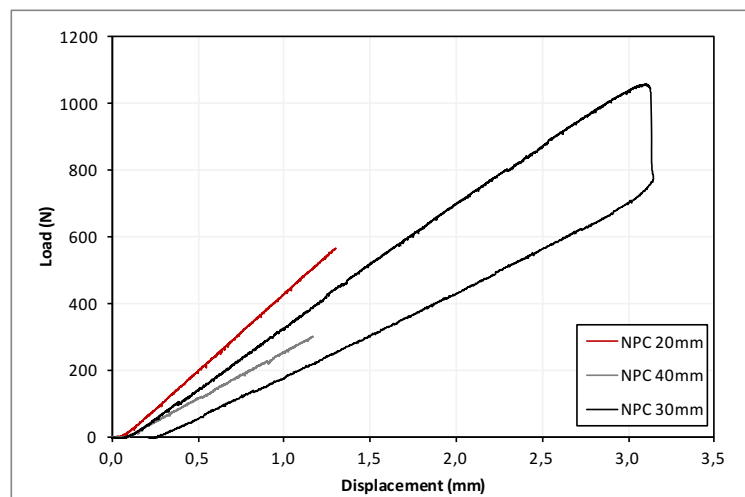


Figure 3.11 – Load displacement plot of an ENF test using compliance calibration method: NPC20 and NPC40 are only required for calibration, while NPC30 is loaded until crack propagates (at load drop).

The same procedure is repeated after the first advancement paying attention to aligning the specimen with respect of the newly found crack tip position, this stage is referred as “pre-cracked” condition (PC tests). The aim of this second procedure is to evaluate possible alteration caused by the presence of an artificial crack tip induced by the Teflon insert.

Two crack advancements are produced and recorded, as specified by the standard, and results indicate that the PC toughness is 1792J/m², lower than the NPC which is 4,6% higher at 1875J/m², the hypothesis that the insert can alter the crack behaviour is confirmed. However, the decreasing trend between does not apply to every individual test repetition, as some specimens also saw an increase from NPC to PC toughness.

Table 3.5 – ENF test data report

Specimen	Fracture Toughness (J/m ²)		Crack length points (mm)		
	NPC	PC	CC	DPI	Difference
ENF 2	1772	1789	66,32	70	5,6%
ENF 3	1848	1794	71,10	75	5,5%
ENF 4	2088	1712	65,51	68	3,8%
ENF 5	1677	1809	66,65	66	1,0%
ENF 6	1990	1859	72,24	79	9,4%
Average	1875	1792	68,4	71,6	5%

Finally, crack length inferred by compliance calibration after the PC tests is verified by dye penetrant inspection, the measured lengths lie within 1mm error, validating the efficacy of the CC reduction method, as well as the test setup. We chose not to verify the crack length after NPC tests because the liquids could alter the behaviour of the crack tip during the PC tests.

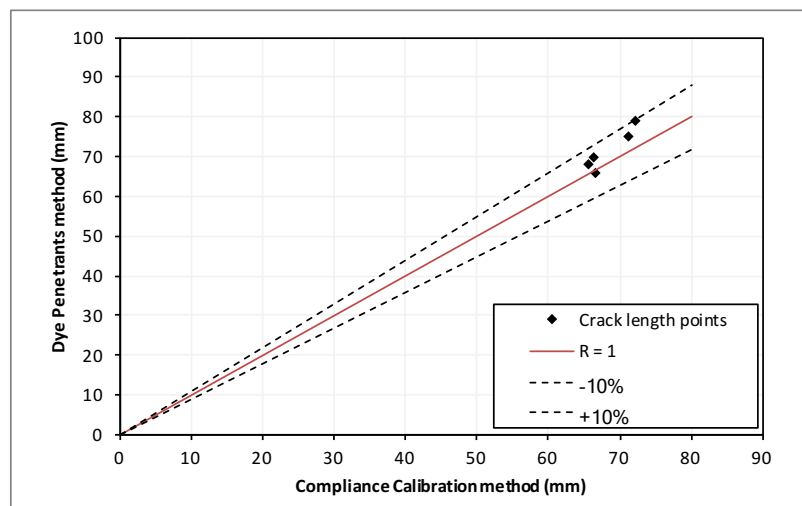


Figure 3.12 – Comparison between numerical and experimental crack length measures. Dashed lines are 90% confidence interval.

3.2.7 Compact Tension

In order to investigate the progressive failure of the material in tensile and compressive loading, a fracture toughness test was developed. This should overcome the brittle failure evidenced in previous tests, and gives information about the energies associated with fractures happening on a plane perpendicular to the plies.

The ASTM E399 reference standard for isotropic metallic materials [33] is not valid for fibre reinforced composites, for which the ESET (eccentrically loaded single-edge-notch specimen) geometry is suggested, described in ASTM E1922 [34]. This reference gives no indication on absolute dimensions of the specimens to test, but only a range of values shown to give acceptable results. In general, with these geometries, the amount of material required for testing is quite high, for this reason, many research labs proposed a new, smaller geometry referenced as Compact Tension (CT), which typically requires just half the area of one ESET specimen. Of several proposed test setups reviewed by Laffan [35], we chose to follow the geometries of Pinho et al. [36,38], because it is proven in many experimental experiences to produce a stable crack growth, and because it's being adopted by several other research groups, comparison of results becomes more convenient. The layup chosen is $[90/0]_{4s}$ for a final thickness of 2.5mm, Overall specimen dimensions are 60x65mm with initial crack length $a_0 = 26$ mm. the initial crack was manufactured using a 1mm thick disk saw until a depth of 20mm, then sharpened using a 0,5mm razor blade up to the desired length. To keep the experimental efforts under control, only one layup is tested, though several reported varying results between dispersed and blocked plies. The interaction between adjacent plies is beyond the scope of this work and the capabilities of our numerical tool.

The test was performed at 0,5mm/min displacement rate, and after each crack propagation, a short unload-reload path was inserted to better capture the compliance of the specimen. In order to avoid bending of the specimen at the free edge, an anti-buckling device was used that constrains off-axis displacement. Similar to the DCB, crack length is measured optically using a magnifying lens, paying attention to synchronize the acquisition of both the test-rig and the camera.

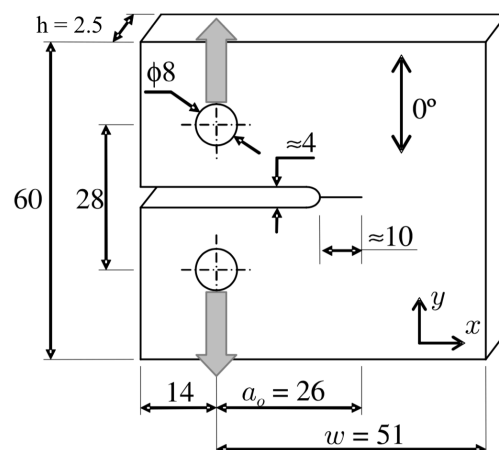


Figure 3.13 – Dimensions and load setup of compact tension test specimen.

There are several data reduction methods available for this type of tests, some analytical, and other numerical, a comprehensive description of the different methodologies is found in [37]. In our experimental campaign, we compared two methods:

- E399 method
- Compliance Calibration

The ASTM E399 is intended for isotropic materials, and it assumes that the specimens are in plane deformation state. Nevertheless, this formulation has been applied extensively to composite material, as many reported differences within 10%. It follows the determination of the stress intensity factor for the given geometry as:

$$K_{IC} = \frac{P_c}{t\sqrt{w}} f(a/w) \quad 3.11$$

with

$$f(a/w) = \frac{2 + a/w}{(1 - a/w)^{3/2}} [0,886 + 4,64(a/w) - 13,32(a/w)^2 + 14,72(a/w)^3 - 5,6(a/w)^4] \quad 3.12$$

Where P_c is the measured critical load at crack advancement, t is the thickness of the specimen, a/w is the normalised crack length, with respect to the length from the load axis to the specimen edge (shown in picture). From the Stress intensity factor, the Critical strain energy release rate of the laminate is calculated from

$$G_{IC}^{lam} = \frac{K_{IC}^2}{\sqrt{2E_x E_y}} \sqrt{\frac{E_x}{E_y} + \frac{E_x}{2G_{xy}} - \nu_{xy}} \quad 3.13$$

Where E_x , E_y , G_{xy} and ν_{xy} are elastic properties of the laminate, calculated using the classical laminate theory from the lamina properties determined by previous experimental tests, reported in Table 3.6 below.

Regarding the Compliance calibration method, this relies on the reduction in stiffness that follows an increase in crack length. By accurate measurements of the compliance after each crack advancement, a polynomial interpolation for the compliance $C_i = C(a_i)$ is fitted to the experimental points at crack lengths a_i and used to solve the following expression:

$$G_c = \frac{P_c^2}{2t} \frac{dC}{da} \quad 3.14$$

Where all terms are defined as before.

Table 3.6 – Cross-ply laminate equivalent properties determined using CLT.

Lamina properties				Laminate Properties [90/0] _{4s}			
E _{11t} (GPa)	E ₂₂ (GPa)	G ₁₂ (GPa)	ν ₁₂ (-)	E _x (GPa)	E _y (GPa)	G _{xy} (GPa)	ν _{xy} (-)
135,5	14,5	4,95	0,31	75,5	75,5	4,95	0,06

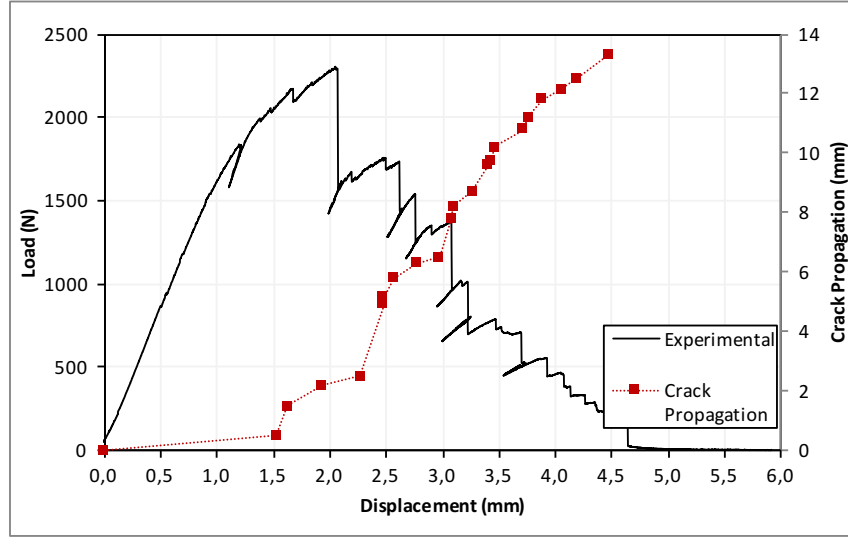


Figure 3.14 – Load vs. Displacement plot of a CT test, in red the measured crack length advancement at each load drop.

A comparison of the two data reduction methods indicate that the CC algorithm is the one with higher uncertainties and scatter. Although the compliance curve vs. crack propagation is coherent and repeatable across the three tested specimens, the derivation of the fitting curve yields to unrealistic values both at the initial and later stage. A better study on the shape of the interpolating polynomial is deemed necessary.

In addition, it is found that at higher displacements, the specimens failed in buckling mode at the free edge, resulting in apparent lower fracture energies, due to the strong increase in compliance. For this reason, the data points beyond 4mm displacement are discarded and only the correct data points are used for the computation of the average value.

Finally, to obtain the lamina fracture toughness relative only to the 0° plies, we must discard the contribute of the 90° plies using the following relation

$$G_C^0 = \frac{t_{lam}}{t_0} G_{Ic}^{lam} - \frac{t_{90}}{t_0} G_{Ic}^{90} \quad 3.15$$

With t indicating the thicknesses of the whole laminate, only the 0 -plies and only the 90 -plies (for a balanced laminate with equal amount of 0° and 90° plies it is of course $t_{90} = t_0 = 0,5t_{lam}$), G_{Ic}^{lam} is the laminate fracture toughness calculated above, G_C^0 is relative to the 0 -plies loaded in fibre direction. Regarding G_{Ic}^{90} we can suppose that a 90° fracture propagates in a similar manner to an interlaminar fracture in tearing mode of a $0/0$ interface, that means that its fracture toughness is equal to the one obtained through DCB testing.

Though some [39] reported values up to 4 times higher for this type of fracture using a comparative analysis of different laminates, this contributes very little to the overall laminate fracture energy, which is still dominated by the 0° plies, to the point that it could be safe even to discard its contribute straight away and simplify the previous

Eq. 3.15 with $G_C^0 = 2G_{Ic}^{lam}$, with the premises of balanced laminate shown above. Final value for the fracture energy was determined at 109,7kJ/m², calculated using the E399 method. The compliance calibration method yields a higher average value at 137kJ/m², though at a deviation twice as high. For this reason, we considered accurate only the value obtained using the E399 procedure.

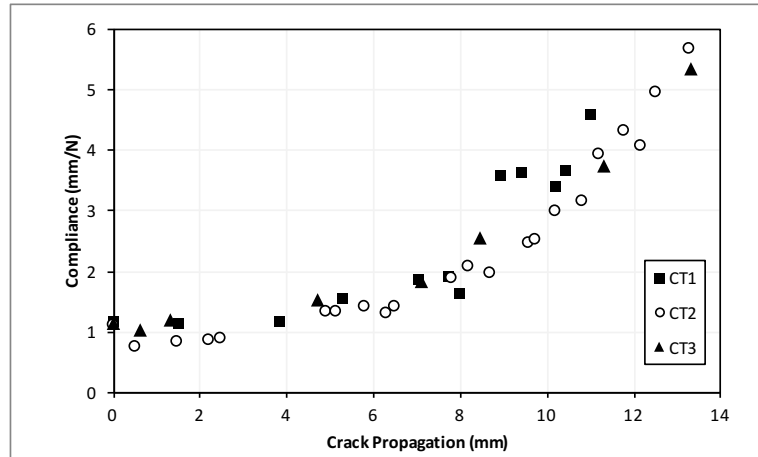


Figure 3.15 – Compliance vs. crack length of three CT test. A 3rd order polynomial fit is used to interpolate the data.

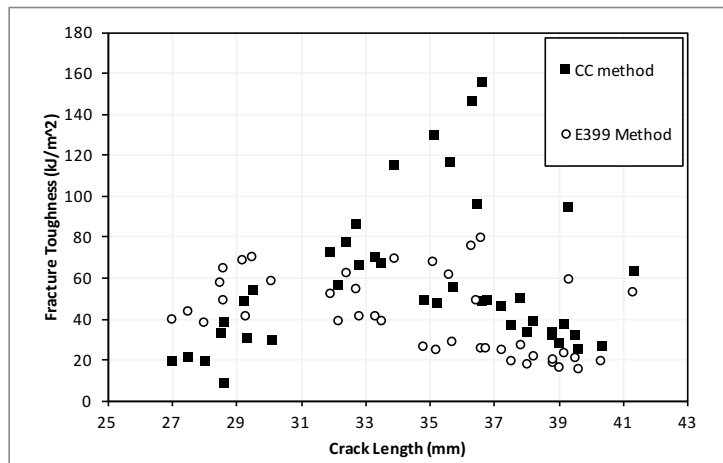


Figure 3.16 – Laminate energy release rates vs. crack length points calculated using the two data reduction methods.

3.2.8 Compact Compression

The general rules apply from the test described above. In this case the notch region is altered, to allow for sufficient displacement without interference, and there is no need for a sharp crack tip. Here the crack propagation is different, as there is not a defined crack plane as in CT mode, but a deformed region extending in front of the crack tip. Identification of the

affected zone is done by comparison of consequent pictures acquired at 5s intervals throughout the whole trial. Also, regarding the load, this doesn't have the clear drops observed in tension mode, but a smoother softening until a definite negative tangent modulus arises. For this reason, and since the specimen unloading is highly non-linear (see the plot below) we cannot measure the compliance by fitting a straight line to an elastic loading region, but we can only assume it as the displacement divided by the load at any given point; this assumes in addition that no plasticity –residual strain– occurs. An example of the load-displacement behaviour is presented in the picture.

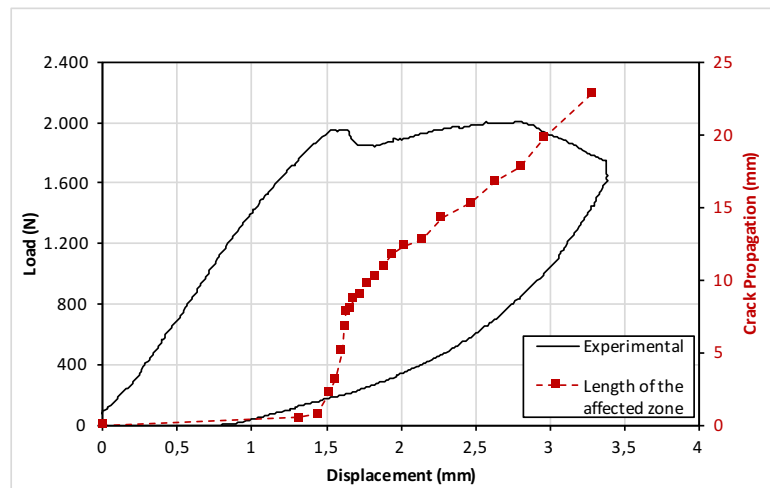


Figure 3.17 – Load vs. Displacement plot of a CC test, in red the measured crack length advancement at each load drop.

The two reduction methods described above are applied to this test, the results are reported directly as the reader can refer to the previous paragraph for more in-depth explanation on the maths behind the data elaboration. The only difference is in the use of the formula 3.15 for the calculation of the 0-ply fracture toughness: in this case, Pinho [36] justifies that failure of the 90° plies happens in a manner similar to the shearing mode for inter-ply fracture, and so $G_{Ic}^{90_{compr}} = G_{IIc}^{delam}$ measured in ENF delamination tests. At any rate, the same observation valid for the tensile case could also apply here, as the contribution of the 90° plies is small compared to the energy associated to the 0° plies, therefore one could simply assume that $G_C^{0_{compr}} = 2G_{Ic}^{lam}$.

As we can see from the plot below, in this case, the E399 method quickly diverges, giving unreliable results, and it's justified by the inappropriate use of the 3.12. The compliance calibration method offers more reliable results, with a general increasing trend, also to be expected, result of the buckling at the mid-plane and the occurrence of different modes of failure in addition to the compressive collapse within the fibre plane: shearing between two penetrating fronds, delamination, extensive buckling.

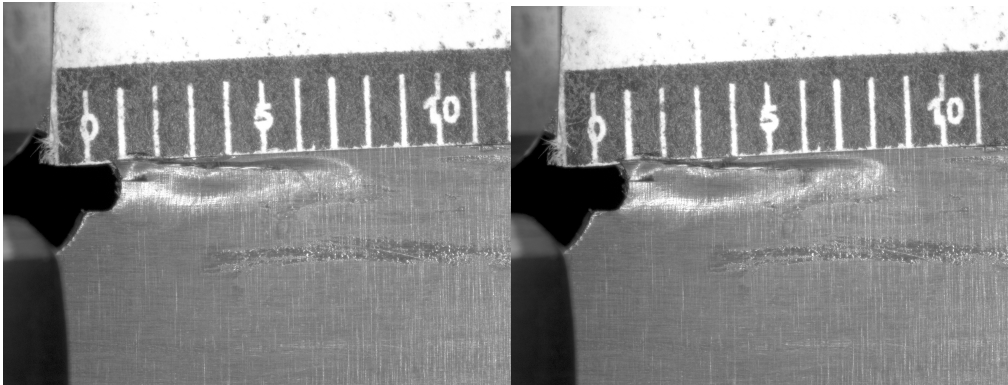


Figure 3.18 – Example of two pictures shot 5 seconds apart for the determination of the fracture affected zone extension (left: ~7,8mm, right: ~8,3mm).

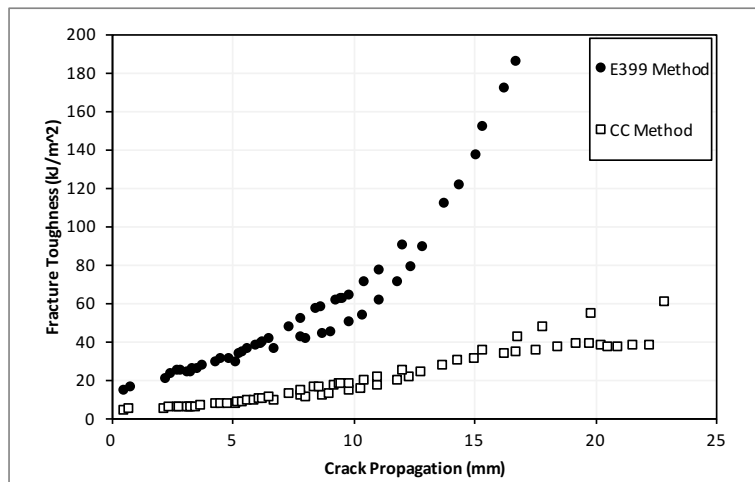


Figure 3.18 – Comparison of laminate fracture toughness from the two data reduction methods for a Compact Compression test.

A definite solution to determine the real toughness value is not available, some suggest considering only the first crack value, but in our case, this will result in a too low toughness, equal to 10kJ/m², probably due to the difficulty in producing a brittle fracture propagation. To obtain a representative value of the compressive in-plane failure mode, we chose to average all data before 10mm crack length, point at which the carried load starts to increase again, after a negative slope, reinforced from the evidence that the acquired images show extensive out-of-plane bending occurs in the outer plies. These two phenomena indicate that the failure mode is different from the one we want to measure, and the reduction method will give unacceptable results. With these considerations, the target value of fracture toughness for this type of loading is determined at 48,2kJ/m².

3.3 Summary of material properties

In summary, we report here a list of all the material properties identified during this testing campaign, and used to define the numerical material model in future FE analyses. Damage parameters are also reported

Table 3.7 – Summary of determined experimental material properties.

Property	Definition	Test	Value
CPT	Ply thickness	Average all	0,15375 mm
ρ	Mass per unit volume	Mixture rule	1.53 g/cm ³
E_{11t}	Tensile axial Young's modulus	Tensile 0°	135,5 GPa
E_{11c}	Compressive axial Young's modulus	Compressive 0°	87 GPa
γ	Compressive softening factor	Compressive 0°	0,27 GPa ⁻¹
E_{22}	Transverse Young's modulus	Tensile 90°	14,5 GPa
G_{12}	In-plane shear modulus	Tensile +45/-45	4,95 GPa
ν_{12}	In-plane major Poisson's ratio	Tensile 0°	0,316
F_{1t}	Tensile axial strength	Tensile 0°	1800 MPa
F_{1c}	Compressive axial strength	Compressive 0°	720 MPa
F_{2t}	Tensile transverse strength	Tensile 90°	36 MPa
$F_{12} 0.2\%$	Shear 0,2% offset strength (plasticity yield)	Tensile +45/-45	43,6 MPa
$F_{12} 5\%$	Shear 5% offset strength	Tensile +45/-45	65 MPa
ϵ_{1t}	Tensile axial failure strain	Tensile 0°	0,0133
ϵ_{1c}	Compressive axial failure strain	Compressive 0°	0,0094
ϵ_{2t}	Tensile transverse failure strain	Tensile 90°	-
ϵ_{12}	Total (el+pl) tensile shear failure strain	Tensile +45/-45	0,075
$Y_{0 \text{ lin}}$	Linear initial shear damage limit	Tensile +45/-45	0,2 MPa ^{1/2}
$Y_{C \text{ lin}}$	Linear critical shear damage limit	Tensile +45/-45	2 MPa ^{1/2}
$Y_{r \text{ lin}}$	Linear shear damage limit	Tensile +45/-45	1,4 MPa ^{1/2}
$d_{\text{max lin}}$	Linear ultimate shear damage	Tensile +45/-45	1
$Y_{0 \text{ exp}}$	Exponential initial shear damage limit	Tensile +45/-45	0,35 MPa ^{1/2}
$Y_{C \text{ exp}}$	Exponential critical shear damage limit	Tensile +45/-45	0,75 MPa ^{1/2}
$d_{\text{max exp}}$	Exponential ultimate shear damage	Tensile +45/-45	0,75
β	Hardening law multiplier	Tensile +45/-45	600 MPa
m	Hardening law exponent	Tensile +45/-45	0,6
$G_{Ic \text{ matrix}}$	Mode I inter-ply fracture toughness	DCB	470 J/m ²
$G_{IIc \text{ mat NPC}}$	Non-pre-cracked Mode II inter-ply Fracture T.	ENF	1895J/m ²
$G_{IIc \text{ mat PC}}$	Pre-cracked Mode II inter-ply Fracture T.	ENF	1792 J/m ²
$G_{Ic \text{ fiber t}}$	Tensile axial intra-ply fracture toughness	CT	107,9 kJ/m ²
$G_{Ic \text{ fiber c}}$	Compressive axial intra-ply fracture toughness	CC	48,2 kJ/m ²

3.4 Validation crush test

A self-supporting specimen was developed, as proposed by the CMH-17 Crashworthiness group [40] consisting in a corrugated geometry with repeating semi-circular pattern of 7mm radius. This geometry was realised in a closed mould having a final thickness of ~1,8mm and manufactured through hand-layup and autoclave curing similarly to all previous samples.

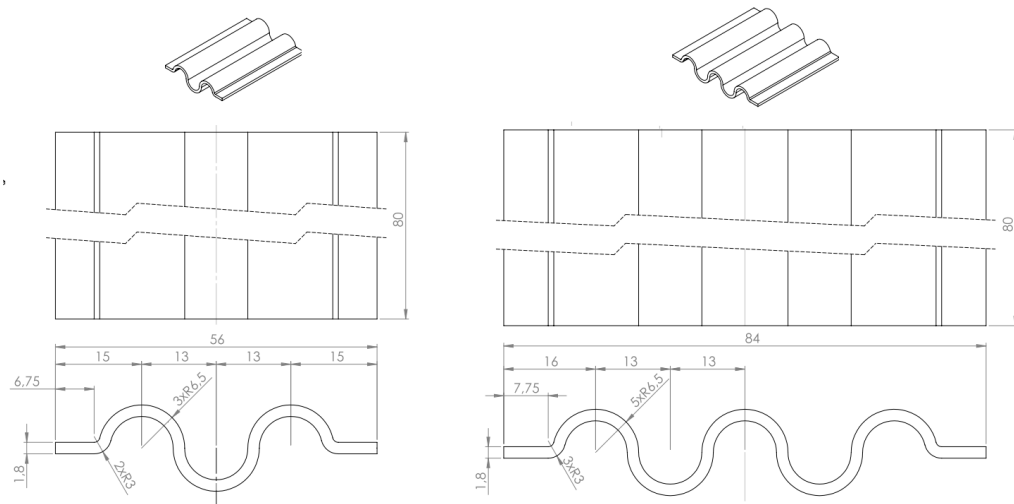


Figure 3.19 – Drawing detail of the Crush specimen geometry, left: 3P, right: 5P.

The layup for the coupon is $[0/90]_{3s}$. The mould is realised in a way that with a single cure it's possible to have four specimens with 3 repeating circular elements and two specimens with 5 repeating semi-circles, all having 80mm final height. The 3P specimens have 60mm width while the 5P specimens are 90mm wide. This geometry is chosen not only for its stable crush, but also for its higher crush load: as evidenced in previous works [41,42] in the presence of rounded sections and curves, brittle micro-buckling and fibre fragmentation is increased, a flat linear section on the other hand will typically fail by delamination and splaying into two fronds, or by global buckling and catastrophic collapse, both associated with lower energy and unstable load.

Axial crush tests are performed at quasi-static loading conditions at 5mm/min rate on a fixture consisting of two plates sliding normally to their planes. The parallelism is imposed by four pillars attached to the lower plate, while the upper moving plate is constrained by four bearing rollers. The test is stopped once 40mm total displacement is reached.

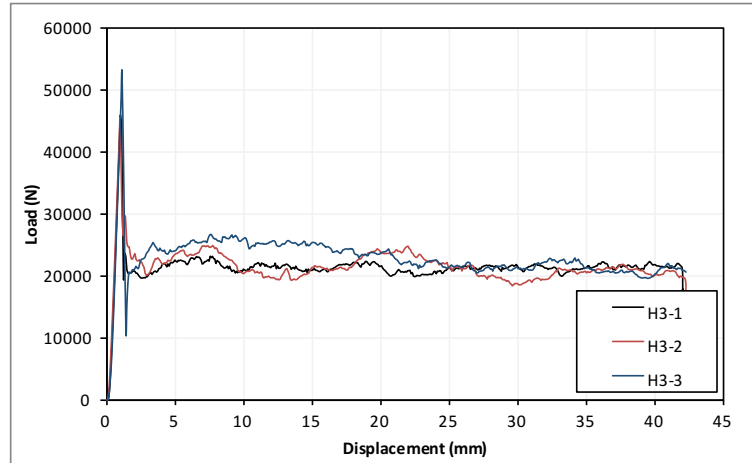


Figure 3.18 – Crush load plot of three 3P specimens tested.

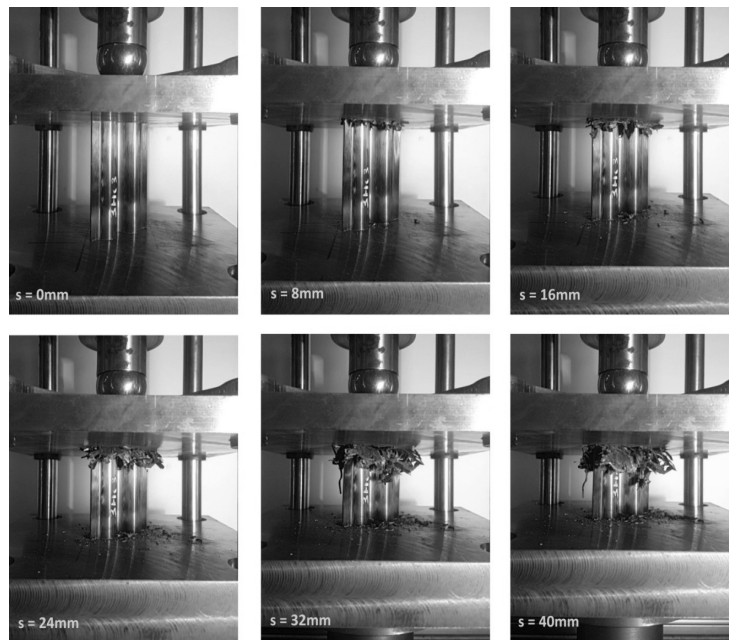


Figure 3.19 – Pictures showing the progressive crushing of a 5P specimen.

The specific absorbed energy (SEA) is then calculated as follows:

$$SEA = \frac{\int_0^{x_j} F dx}{\rho_c A_f x_j} \quad 3.16$$

Where F is the crush force, x_j is the stroke at the time j , ρ_c is the specific weight of the composite, and A_f is the frontal crush area. It is evident that in 3.8 the numerator is the crush energy while the denominator is the crushed mass.

Table 3.7 – Summary of crush trials experimental data.

	Initial load peak (kN)	Sustained crush load (kN)	Initial slope (kN/mm)	Crush Efficiency	SEA (J/g)
3P_1	53,9	18,8	57,6	0,349	88,91
3P_2	46,1	21,2	56,1	0,461	98,77
3P_3	40,5	21,3	59,1	0,527	97,97
3P_4	52,9	23,0	58,3	0,435	104,40
5P_1	70,5	31,8	36,2	0,45	99,13
5P_2	71,1	32,1	71,5	0,45	101,93
Average	-	-	-	0,445	98,52

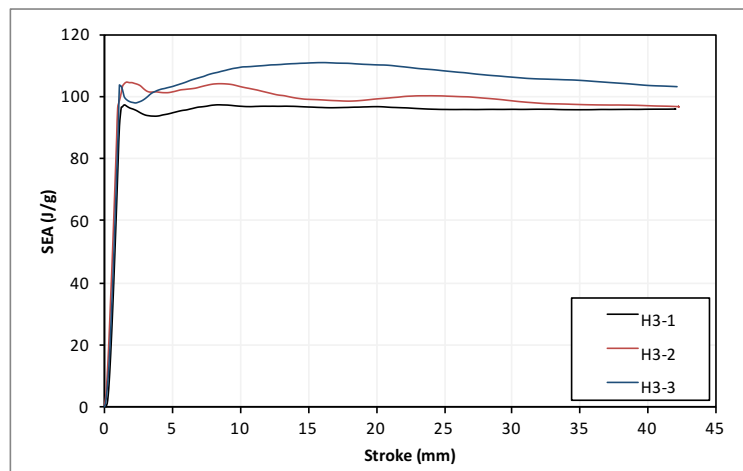


Figure 3.20 – SEA curves for three corrugated crush specimens

All tested specimens show similar behaviour, with constant sustained crush load of 20kN for the 3P geometry, 32kN for 5P geometry, in both cases the resulting SEA measures slightly below 100J/g, constant throughout the crush stroke. After verifying that the two geometries gave very similar results in terms of SEA, we decided to limit the numerical efforts only to one geometry, discarding the 5P trials and focusing on the analysis of the 3P specimens.

After visual inspection, the predominant modes of failure during crush are observed: fibre fracture by local micro-buckling was found to be the main energy absorbing mechanism in the central blocked plies, with limited lamina splaying occurring primarily in the flat outer regions. A central debris wedge is considered to contribute to a high extent to the crush load, the motivation is twofold: fibre breakage is a high energy failure mechanism, and very small fragments almost powder-like, generate high friction forces between the crushing plate and the lateral laminas.

CHAPTER 4

VALIDATION OF NUMERICAL CRASH MODEL

Aim of this phase is to build a numerical model and a reliable procedure to simulate a crash event. Following the same principles of the building block approach for the experimental campaign, we will scale up with simulation efforts, starting from the most elementary load cases, gradually to more complex scenarios. For the numerical FE simulations, the finite element tool Virtual Performance Solution (VPS) of ESI-software is used. This is the dynamic explicit solver formerly known as Pam-Crash, allows for simulation of complex composite structures under dynamic loading, as required for a typical crash simulation, and offers material cards specific for composite materials, refined models for contact between parts and powerful solution algorithms.

4.1. Composite simulation in VPS

VPS files are based on cards, simple text based formatted documents used to store definitions for most of the features of the numerical model [43]. The feature tree displayed in the figure below, shows the typical configuration for a simple model containing several entities described here:

- **Controls:** the principal set of numerical properties used to define how to run a simulation
- **Parts:** individual disjointed bodies with different material and properties,
- **Materials:** the set of physical properties that can be associated to one or multiple parts
- **Plies:** specific to composite materials, the set of properties representative of a single lamina
- **Layers:** a system used to build a lay-up of plies with varying orientations
- **Links:** used for the definition of tied pairs (Cohesive interfaces)
- **Contacts:** a set of definition for the interaction between and within parts
- **Constraints:** Boundary conditions that define the dynamics of the model.
- **Auxiliaries:** a collector for functions and curves used throughout the model.

A full detailed description of each section of the model tree is beyond the scope of this work, so we will limit our in-depth analysis to those entities related to composite materials, and some additional information regarding supplementary variables object of our sensitivity analyses.

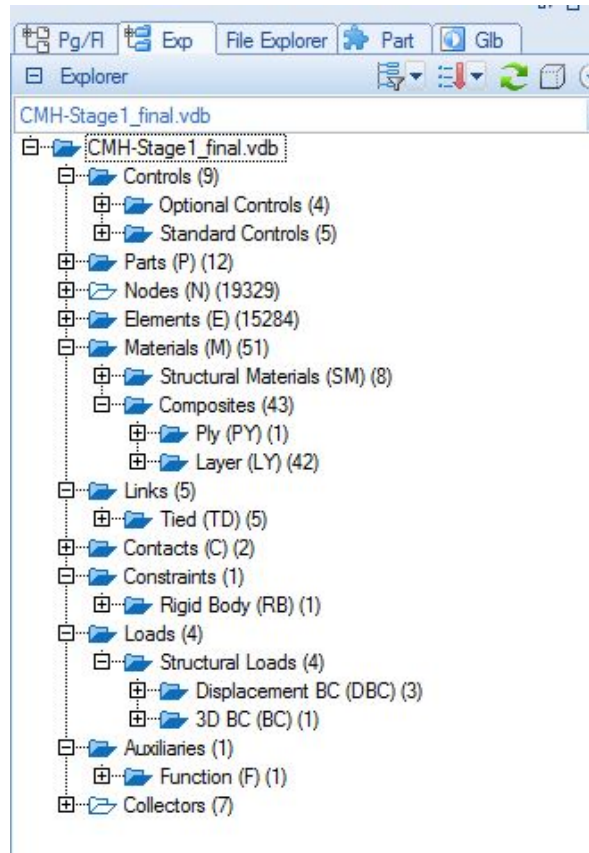


Figure 4.1 – Feature tree of a generic VPS file.

4.1.1. Orthotropic Composite material model

Material type MAT131 corresponds to Multi-layered Shell Elements. The layers can consist of materials modelled as elastic damaging fibre-matrix (bi-phase or global) composite, or elastic-plastic with damage. This is the material used to define every fibre reinforced material. Plies are numbered consecutively from shell element side $z = -t/2$ to $z = +t/2$ where t is the element thickness defined in the Part card. It must be taken care that each specified ply corresponds to one integration point across the thickness of the shell, located at the centre of the ply. The minimum allowed number of plies is equal to one. In that case, the element responds as a membrane and no bending moments are considered. A minimum of 5 integration points is recommended to represent bending moments effectively.

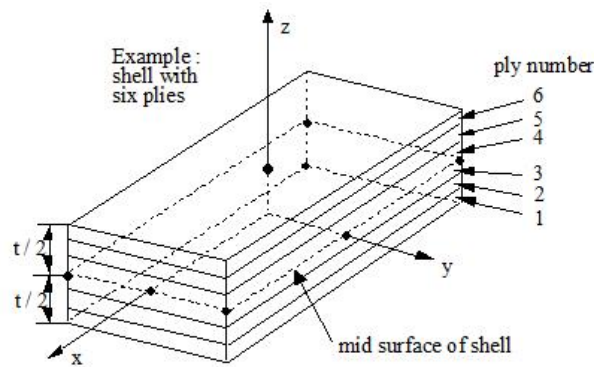


Figure 4.2 – Multi-layered shell layout representation.

In the table below, a selected list of input parameters for MAT131 are described. This card is used mainly to define the stacking sequence of the composite, in addition to some numerical parameters for stable simulation.

Table 4.1 – Select MAT131 user-defined inputs

Name	Definition	Type	Notes
KSI	Stiffness proportional damping ratio	Numerical	N/A
Fo	Damping target frequency	Numerical	N/A
HGM	Membrane Hourglass coefficient	Numerical	Recommended: 0,01 to 0,05
HGW	Out-of-plane Hourglass coefficient	Numerical	Recommended: 0,01 to 0,05
HGQ	Rotation Hourglass coefficient	Numerical	Recommended: 0,01 to 0,05
As	Transverse Shear correction factor	Numerical	N/A
NOPER	Number of operations (layers)	Logic	Each layer is one integration point
ILAY	Flag for layer definition type	Logic	Choose between ply method and layer method.
IFAIL	Flag for failure type	Logic	Refer to reference manual
NMIN	Cycles to damage saturation	Numerical	Number of cycles required for damage to reach 1, used to prevent catastrophic failure

The multi-layered shell layout can be defined in two different ways using the ILAY flag: the so called “layer” definition and the “ply” definition. The former computes the equilibrium for each single layer, while the latter solves the equilibrium of the whole layout using the equivalent elastic properties of the stack calculated using the Classical Laminate Theory (CLT). This option doesn’t store stresses and strains of each individual lamina in the output, but only the shell element average. For the purposes of this work we choose then to adopt the more detailed approach using layers.

In combination with MAT131, several ply types are available to build the composite stack, the most used are:

- PLY ITYP = 0, unidirectional bi-phase ply
- PLY ITYP = 1, unidirectional global ply
- PLY ITYP = 7, fabric global ply
- PLY ITYP = 8, fabric bi-phase ply.

The bi-phase models refer to an older damage model which considers the damaging of matrix and fibre separately, its mathematical framework is analogous to the Ladevèze model, but it's been substituted gradually by the ITYP1, the global composite ply model, because the latter is easier to determine from a set of experimental data, tackling the specific damage modes with specific test geometries.

The fabric models are similar to their unidirectional counterparts: While still being an orthotropic model with distinct axial and transverse elastic properties, their associated damage laws are identical, as they have the same formulation, though they are set independently. In-plane shear damage is also considered, and takes the same formulation seen in the UD ply model.

4.1.2. Ladevèze damage model

In this work, we only deal with UD plies, therefore, we will limit to an in-depth look at the PLY ITYP = 1. In the following table, an extensive look at the ply card is presented, with a description of most of its parameters and some considerations on their experimental determination methods.

In Table 4.2 the parameters for ply ITYP1 are presented, highlighting each category according to function: base elastic properties are in the first orange block, in blue the fibre damage model is defined, in green the matrix damage, and lastly yellow for plasticity. The Ladevèze damage model described in Chapter 3 is defined in its entirety by the parameters in highlighted green and yellow. Additional functions like strain rate modelling and numerical formulation and hourglass coefficients are not shown, as they are discarded or left to default values as suggested in the reference manual.

For the element elimination, an equivalent shear strain limit is used: this corresponds to setting FAILINP = 1 and FAILTYP = 0 and the unique parameter EPSIslim to 0,14. A compromise value between stability of the solver and conservative energy removal: the elements cannot be eliminated too early because it would alter the energy contribution of the deforming bodies, but also not too late, because this would require the time-step for calculation to drop too low and stop the solution altogether.

$$EPSIslim = \frac{1}{3} * (\varepsilon_{12} + \varepsilon_{23} + \varepsilon_{13}) \quad 4.1$$

This method for element elimination is quick and acceptable for setting up a general criterion in complex models, but it is not adequate for simple coupon level tests, because EPSIslim cannot trigger basic loading modes like pure tension or compression, but is only activated from shear deformation, per its definition in Eq. 4.1. For this reason, a more detailed strain based failure method is used where felt necessary: FAILTYP = 6 (maximum strain model) makes possible to define strain limits for element elimination in all 6 directions, three axial and three shear, and both positive and negative direction, for a total of 12 inputs required. This renders the simulations under complex loading much more flexible, though at an increased complexity.

Table 4.2 - Select PLY ITYP1 user-defined input definition and required experimental tests

Name	Definition	Type	Measurement/Notes
ITYP	Ply type identification number	Logic	N/A
RHO	Mass per unit volume	Experimental	Density test
E0t1	Tensile axial Young's modulus	Experimental	0° tension test
E0t2	Transverse Young's modulus	Experimental	90° tension test
E0c1	Compressive Axial Young's modulus	Experimental	0° compression test
GAMMA	Compressive softening factor	Experimental	0° compression test
G012	Shear modulus G12	Experimental	Shear tension test
G023	Shear modulus G32	Experimental	Other shear test
G013	Shear modulus G13	Shear factor	Other shear test
NU12	Poisson's ratio ν_{12}	Experimental	0° tension test with biaxial strain measurement
KAPPA23	Shear correction factor	Numerical	N/A, Default: 0,833
KAPPA13	Shear correction factor	Numerical	N/A, Default: 0,833
KSI	Kinematic damping factor	Numerical	N/A Default 0,1
EPSifti	Initial strain axial tensile damage limit	Experimental	0° tension test
EPSiftu	Ultimate strain axial tensile damage limit	Experimental	0° tension test
Dftu	Axial tensile damage limit	Damage factor	Recommended: 0
EPSifci	Initial strain axial compressive damage limit	Experimental	0° compression test
EPSifcu	Ultimate strain axial compressive damage limit	Experimental	0° compression test
Dfcu	Axial compressive damage limit	Damage factor	Recommended: 0
IBUCK	Buckling computation flag	Logic	N/A
ISHD	Shear damage function flag	Logic	N/A
ITRD	Transverse damage function flag	Logic	N/A
Y0	Initial shear damage	Experimental	Cyclic shear tension test
Yc	Critical shear damage	Experimental	Cyclic shear tension test
Y0p	Initial transverse damage	Experimental	Cyclic transverse tension test*
Ycp	Critical transverse damage	Experimental	Cyclic transverse tension test*
B	Shear/transverse coupling factor	Experimental	Cyclic transverse tension test*
Dsat1	Shear damage limit	Numerical	Cyclic shear tension test
Dsat2	Transverse damage limit	Numerical	Cyclic transverse tension test*
R0	Plasticity threshold stress	Experimental	Shear tension test
BETA	Plasticity power factor	Experimental	Shear tension test
m	Plasticity exponential factor	Experimental	Shear tension test
A	Coupling factor	Experimental	Default: 0

* test not performed, assumptions made

4.1.3. Waas Pineda Failure model

Defined as a failure mode, the Waas-Pineda progressive damage model described in Chapter 2 belongs in the ply card, and it's set using initiation threshold values (highlighted in blue in the table below) and fracture energy values (in green) for the 5 main in-plane fracture orientation and modes: fibre tension and compression, matrix tension and compression and shear. To finish, cut-off value D_{max} is used to activate the post-damage state, and the equivalent shear strain for element elimination, behaving in a similar way as described earlier. The D_{max} parameter is found to be very useful and sensitive for a crush type of simulation, influencing both numerical stability (degree of softening of the elements) and the specific deformation energy of the material.

Table 4.3 - Waas-Pineda failure type model

Name	Definition	Type	Measurement/Notes
IFL11	Axial initialisation mode flag	Logic	0: stress-based, 1: strain based
VAR11	Tensile axial limit	Experimental	Tensile test
VAR11c	Compressive axial limit	Experimental	Compressive test
IFL22	Transverse initialisation mode flag	Logic	0: stress-based, 1: strain based
VAR22	Tensile transverse limit	Experimental	Tensile transverse test
VAR22c	Compressive transverse limit	Experimental	Compressive transverse test
VAR12	Shear limit	Experimental	Shear test
ETA	Mixed mode exponent	Numerical	N/A
EFT11t	Axial tensile fracture energy	Experimental	Fracture toughness test
EFR11c	Axial compressive fracture energy	Experimental	Fracture toughness test
EFR22t	Transverse tensile fracture energy	Experimental	Delamination test
EFR22c	Transverse compressive fracture energy	Experimental	Delamination test
EFR12	Shear fracture energy	Experimental	Delamination test
Dmax	Maximum damage	Numerical	Requires calibration
EPSIslim	Equivalent shear strain limit	Numerical	Recommended: 0,15
Ifelim	Element elimination behaviour flag	Logic	

4.1.4. Tied interface model

Cohesive element definition requires a three stages setup: one material card to define the cohesive behaviour, one part card and one link to define the two bodies to put in contact with each other. The Link card requires a Master-Slave definition and the connection goes from the master body's nodes to the nearest element of the slave part. An appropriate research distance must be defined so that the search algorithm can perform the connection. The part and link cards are trivial, and don't contain any useful information, only the logic of the connection, the material card instead contains all the model parameters for the cohesive zone behaviour. The material card MAT303 input deck is shown in Table 4.4.

Table 4.4 – Select MAT303 user-defined input definition and required experimental data.

Name	Definition	Type	Measurement/Notes
RHO	Failure type identification number	Logic	N/A
IDBEAN	Flag to update tied normal	Logic	Recommended: based on mean rotation
I3DOF	Flag to tie rotational DOF	Logic	N/A
IDELA	Cohesive model flag	Logic	N/A
Ncycle	Cycles for bilinear law	Numerical	Requires calibration
hcont	Length for computation	Computational	Recommended: Set equal to shell distance
E0	Elastic modulus tearing	Experimental	Initial value from tensile 90° test
EFRAC1	Fracture energy tearing mode	Experimental	From DCB test
SIGMAst	Initialisation damage stress	Numerical	Requires calibration
SIGMApr	Propagation damage stress	Numerical	Requires calibration
G0	Elastic modulus shearing	Experimental	Initial values from tensile shear test
EFRAC2	Fracture energy shearing mode	Experimental	From ENF test
GAMMAst	Initialisation damage stress	Numerical	Requires calibration
GAMMApr	Propagation damage stress	Numerical	Requires calibration
IFUNGcont	Mixed mode interaction function	Function	From MMB test (optional)

4.1.5. Contact pairs definitions

Interaction between bodies are defined in the contact section. These algorithms are used to prevent penetration between and within bodies, guarantee deformations and allow forces transmission, thus play an important role in the correct simulation of a crush model. In particular, our numerical models often contain interaction between shell and solid bodies. Shell elements are used to simulate the layered composite, as extensively described previously, while solid bodies are better suited for rigid, undeformable elements (plates, blocks, pins) that apply deformation to the composite. In the more basic load cases, the deformation can be imparted directly as nodal displacement at the specimens' unconstrained ends, but wherever a sliding interaction or deforming behaviour of the composite is expected – as for example in a three-point bending configuration, as well as the crush simulation itself – it is necessary to impose the deformation through an in-between rigid body.

VPS contains several search algorithms for identification of contacting bodies and transmitted forces. In our models, we used the node-to-segment algorithm, that proved efficient in contact between shells and solid elements (Type 33 and 36). The software distinguishes whether the contact is of the master-slave type or a self-contacting type, though their working principles are basically identical. A self-contacting card is used to prevent the penetration of each laminae with themselves, important during crushing where deformations are significant and difficult to predict. A list of the properties that have to be defined in the contact card are reported in the table below. Master and slave entities can be parts or single elements (surfaces), and are defined additionally in the card, Self-contact only has one slave type definition.

Table 4.5 – Select Contact 33 and 36 user-defined input.

Name	Definition	Type	Notes
ITPRT	Interaction type definition	Logic	0: constant thickness (<i>Hcont</i>); 1: thickness by PART, zero contact thickness allowed; 2: thickness by PART, zero contact thickness not allowed.
Hcont	Contact height	Numerical	Define contact height for computation
IPCP	Flag for precise contact computation	Logic	N/A
SLFACM	Scale factor penalty	Computational	Default: 0,1
FSVNL	Nonlinear penalty stiffness	Computational	N/A
IKFOR	Flag for kinematic contact forces	Logic	0: deactivated; 1: activated
FRICT	Coulomb friction coefficient	Experimental	Requires calibration
IDFRIC	User-defined friction model	Experimental	For advanced calibration
IRMV	Initial penetration removal	Logic	0: no penetration removal; 1: modify geometry (nodal coordinates) to remove initial penetrations; 2: modify local contact thickness to remove initial penetrations; 4 (explicit only): remove local initial penetrations per contact pair.
IAC32	Compatibility with TIED link	Logic	0: treatment is suppressed. 1: treatment is active

4.2. Coupon level simulations with Ladevèze CDM

Each of the elementary load cases described in the previous chapter is simulated to build and verify the material card, familiarise with the software, and calibrate the damage model to match experimental results.

We will follow the same order introduced in Chapter 4, so starting from the simple tension and compression tests at various fibre orientations to verify the base undamaged lamina properties, moving on to the damage model specific load cases. In parallel, the calibration of cohesive elements is performed through simulation of DCB and ENF loads for tackling the specific interlaminar fracture modes. Compact tension and compression tests follow through for validation of the intra-laminar fracture mode, with a useful comparison between Ladevèze and Waas-Pineda modes.

As a general rule, where not specified, all simulations are run at a displacement rate of 1mm/ms. This rate is high enough to have short simulation times, since the time-step is imposed by the Courant condition and in our cases, is in the range of $1 \cdot 10^{-5}$ to $3 \cdot 10^{-5}$ ms.

4.2.1 Tensile load

A simplified model for tensile behaviour simulation is easily built to be representative of the tensile tests from the experimental campaign. While not matching the dimensions of the

experimental campaign, the intrinsic material properties are still identified correctly. Goal of this first run is to verify the behaviour of the FE model at failure.

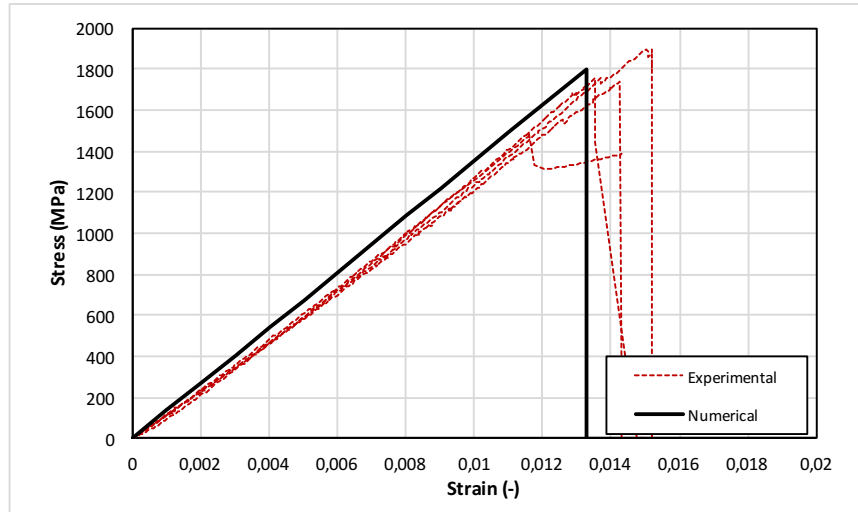


Figure 4.3 – Tensile model results (black) compared to experimental data.

As expected, the tensile coupon fails in brittle mode at the expected load of 1800MPa, a trial run with different mesh size (0.25, 0.5, 1 and 1.67mm) showed that there is no influence on the failure load, though the propagation of damage after element elimination remains unpredictable. Because there are no trigger mechanisms, any of the elements comprising the model could fail at the target load before the others, this is due to small stress fluctuations attributed to pressure wave propagation, intrinsic of the explicit solver. These variations are of small magnitude and do not represent a concern for the full-scale modelling.

4.2.2 Compressive load

Compression simulation does not require any particular attention, so we used the same file of the tensile case, with the only modification that the displacement of the free end nodes is in opposite direction, everything else is maintained the same. Highlight of this test is to verify the modulus softening, as visible in the plot below, the model behaves as expected. For a detailed description of the numerical model related to fibre damage, the reader should refer to Chapter 3. Model parameters used in these simulations are presented in Paragraph 4.4.

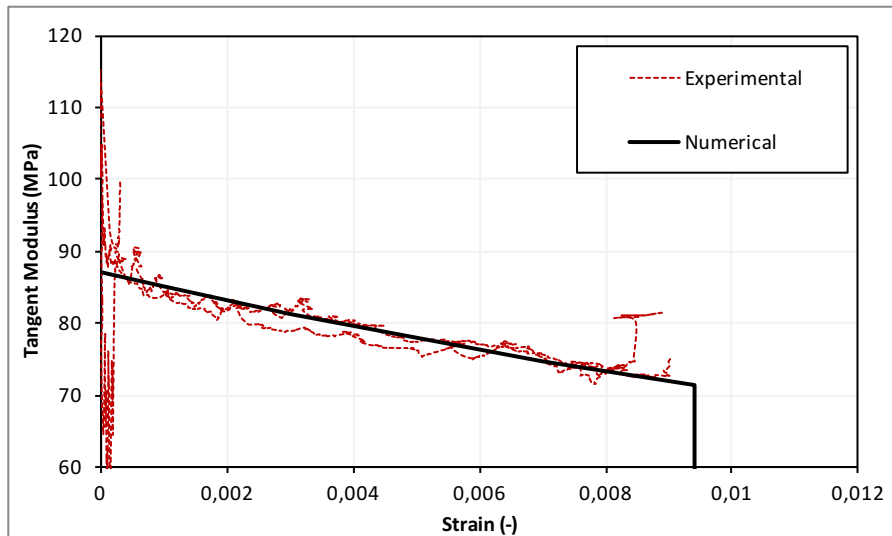


Figure 4.4 – Compressive modulus reduction model results (black) compared to experimental data.

4.2.3 Shear load

To simulate this load case, a simple square of 25x25mm dimensions with 1mm mesh size is built. Two numerical models are developed: a single multi-layered shell simulating the $[+45/-45]_{4s}$ layup and one with stacked shells for each lamina connected with TIED elements (this one, is done after calibrating the cohesive model, see below). This effort was justified to evaluate whether the cohesive interface played a role in the load transmission. The boundary conditions consist in a row of nodes constrained in 5 DoF, leaving the transverse contraction free, the opposite row is imposed a displacement at constant rate. To avoid under-constraining the model, a central symmetry plane is fixed in transverse displacement, as shown picture.

The two numerical models have perfectly equivalent stress results, indication that the cohesive model does not affect this simple loading mode. The results presented hereafter refer to the single shell model. The numerical output, as expected, does not contemplate the nonlinearities observed in the experimental results, nevertheless, the numerical results match correctly with the experimental data.

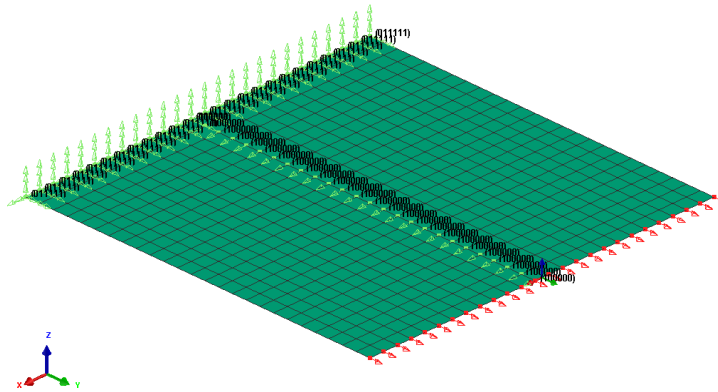


Figure 4.5 – In-plane shear tensile model representation with highlighted BC.

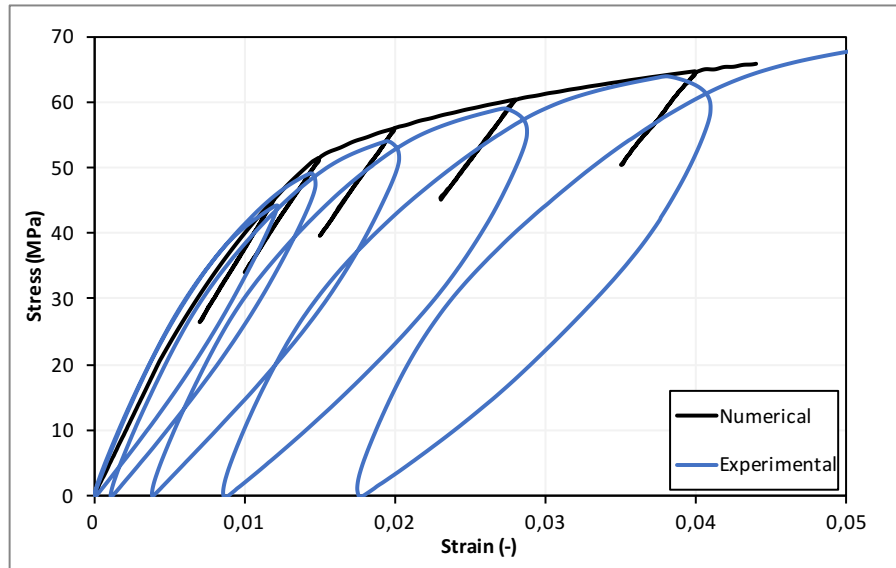


Figure 4.6 – Comparison of tensile shear numerical results with experimental test.

4.2.4 Mode I delamination

Because of the mesh sensitivity of cohesive elements, the correct mesh size for simulation of the cohesive zone must be identified first: the maximum allowed mesh size is imposed by the interface strength and the maximum stress through the following relation

$$LPZ = m \frac{E_0 G_{IC}}{\sigma_{max}} \quad 4.xx$$

Where LPZ indicates the length of the process zone in unit length, E_0 is the elastic constant of the interface, set equal to the measured transverse modulus of 14,5GPa, G_{IC} is the interface strength and σ_{max} is the maximum allowed stress, evaluated at 36MPa. The nondimensional parameter m , which depends on the cohesive model, is typically close to

unity (Falk, Rice [45-46] Hillerborg [47]). The relation above gives an indication of the number of elements in the process zone. When the cohesive zone is discretized by too few elements, the distribution of tractions ahead of the crack tip is not represented accurately, therefore, a minimum number of elements is needed in the cohesive zone to get successful FEM results. The minimum number of elements needed in the cohesive zone is not well established: in their parametric study [48] Turon, Davila and Camanho found that for predicting the delamination in a DCB specimen, a process zone of 3 elements was sufficient. This criterion is considered valid, and results indicate that a mesh size of 0,8mm is sufficient for correct load representation.

The fully determined cohesive model is shown graphically in picture, the following table summarises the parameters of the TIED interface.

Table 4.6 – Numerical TIED mode I user-defined input definition.

Name	Definition	Unit	Value
RHO	Failure type identification number	kg/mm ³	1,2E-6
hcont	Length for computation	mm	0,16
E0	Elastic modulus tearing	GPa	14,5
EFrac1	Fracture energy tearing mode	J/mm ²	0,00047
SIGMAst	Initiation damage stress	GPa	0,036
SIGMApr	Propagation damage stress	GPa	0,036

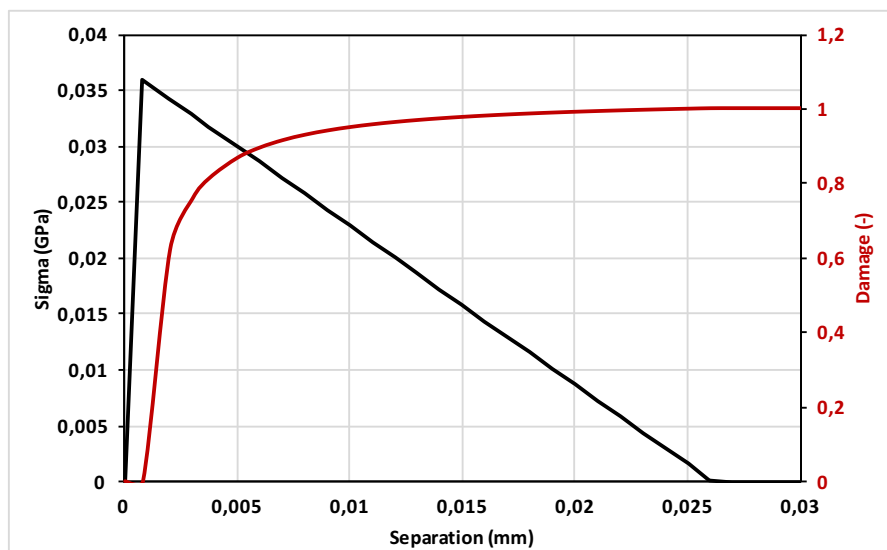


Figure 4.7 – Representation of the Mode I cohesive traction-separation law.

The numerical model is built using shell elements and tied interfaces between each lamina, to verify that no unexpected behaviour of the interfaces occurs. The delaminated area is created removing the links between elements up to 60mm length, mimicking the experimental setup. The loading blocks are also simulated, to get information about the bonding stresses.

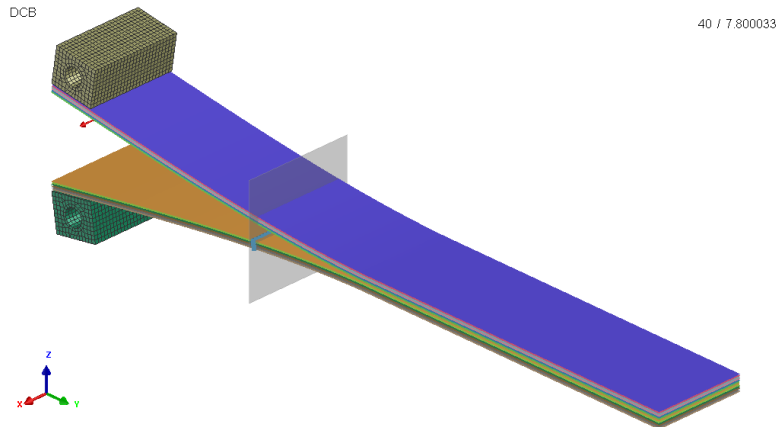


Figure 4.8 – DCB numerical model representation.

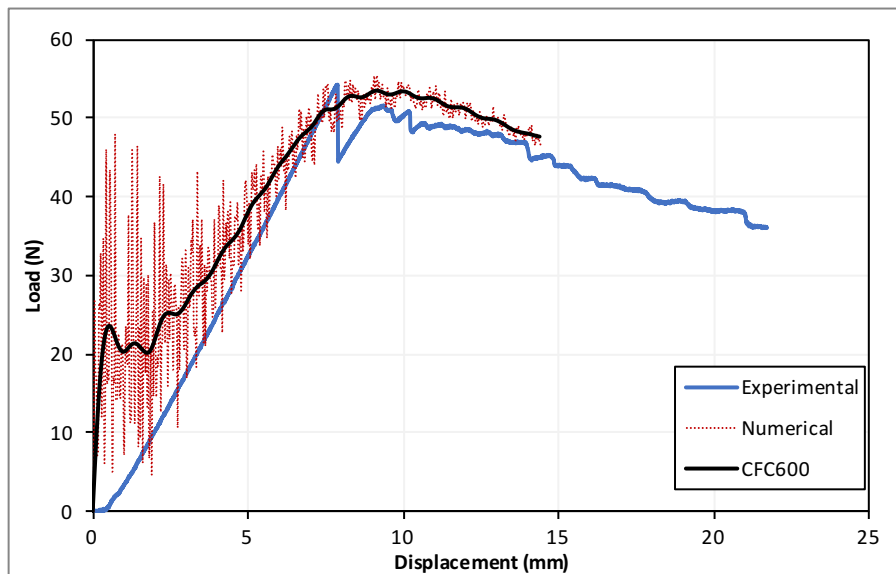


Figure 4.9 – Comparison of DCB simulation with experimental test.

4.2.5 Mode II delamination

This coupon test simulation is also modelled as the full specimen, comprising the loading pins through which the displacement is imposed, fully replicating the experimental setup in high detail. The specimen dimensions are equal to the experimental case, only the 30mm crack length test is simulated (see Chapter 4 for more details on the test setup).

The same considerations on mesh size used in DCB simulation are repeated here, with the only difference that in Eq.4.xx the elastic modulus E_0 is replaced with the shear modulus G_{12} , the interface strength is the one relative to Mode II loading, and the allowed stress is $\tau_{max} = 43,5MPa$. Mesh size considerations are similar to the DCB case, with the condition of a sufficient process zone of 3 elements, a mesh size of 1mm is acceptable. Note that in general,

the full-scale model mesh size will be imposed by the smaller of the two calculated mesh sizes for mode I and II delamination.

Table 4.7 – Numerical TIED mode II user-defined input definition.

Name	Definition	Unit	Value
RHO	Failure type identification number	kg/mm ³	1,2E-6
hcont	Length for computation	mm	0,16
G0	Elastic modulus tearing	GPa	4,95
EFrac2	Fracture energy tearing mode	J/mm ²	0,001792
GAMMAst	Initiation damage stress	GPa	0,0435
GAMMApr	Propagation damage stress	GPa	0,0435

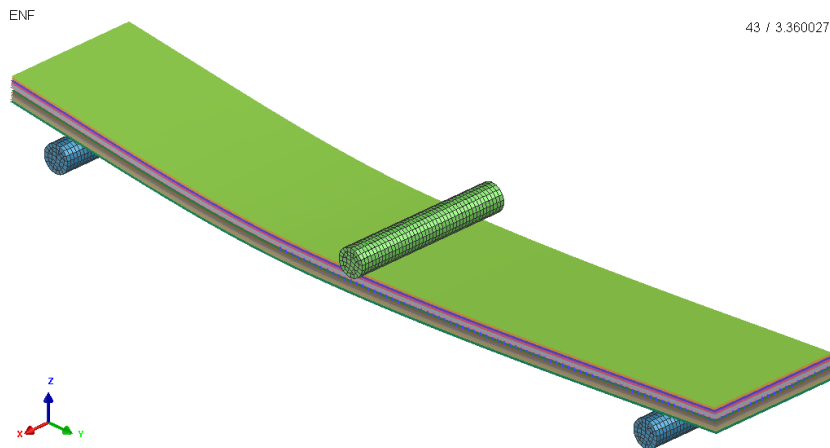


Figure 4.10 – ENF model representation, with pins modelled with brick elements.

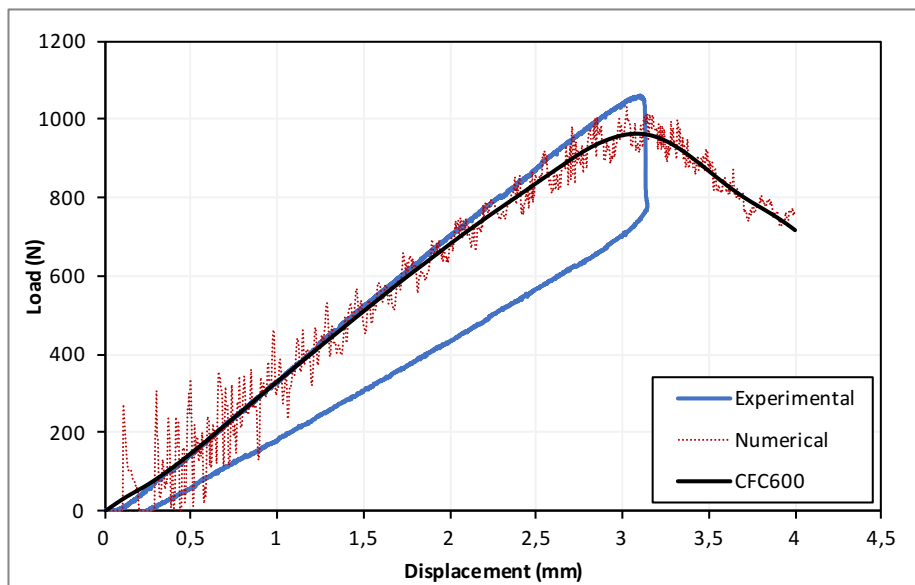


Figure 4.11 – Comparison of ENF simulation with experimental test.

4.2.6 Inter-ply fracture

Simulation of inter-ply failure is done for the compact tension and compact compression tests described in the previous chapter. A multi-layered model and a single shell one were created and compared, As for the in-plane shear loaded model, no appreciable differences were observed, again, indicating that the tied connection don't work under this loading fashion.

In order to appreciate the fracture region correctly, a mesh refinement to 0,5mm is present at the crack tip region, through the whole midline, as can be seen in Figure 4.12. Load is applied through the two loading pins that have an imposed displacement rate. This was done to evaluate the stress transfer around the hole region.

Results indicate that the initiation of fracture is somewhat identified, although the peak load is overestimated at by 20% at 2788N, because of plasticisation at the crack tip in the experimental case. Furthermore, the propagation of damage is more drastic than in the real case, with the load rapidly falling near zero after just 2mm of displacement, whereas the experimental test sustained a moderate load up until at least 4mm of crack opening displacement. This discrepancy is motivated by the brittle behaviour in the fibre direction as seen in paragraph 4.2.1, causing elimination of elements near the crack tip and rapid loss of sustained load.

Similarly, in compression load, the model fails abruptly, and loss of contact due to elimination of elements at the crack tip causes a load curve with spikes and typical saw tooth behaviour.

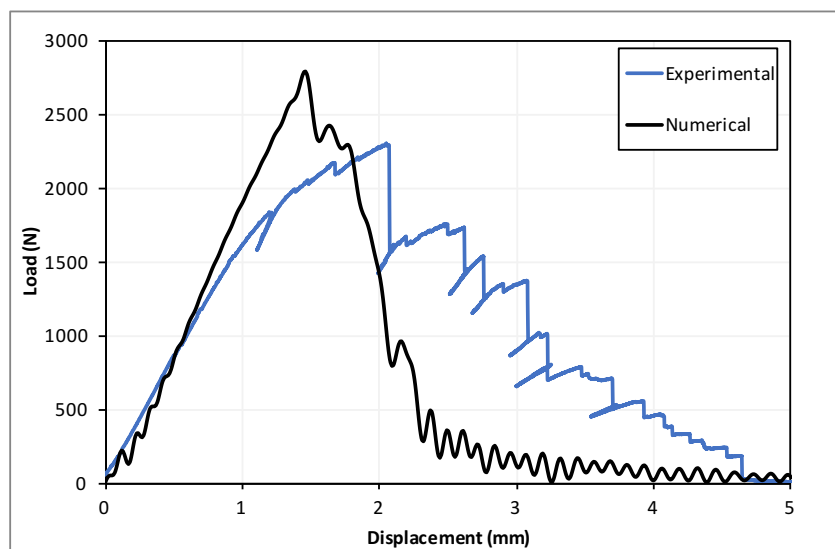


Figure 4.12 – Numerical LV model results for compact tension geometry load, compared to experimental data.

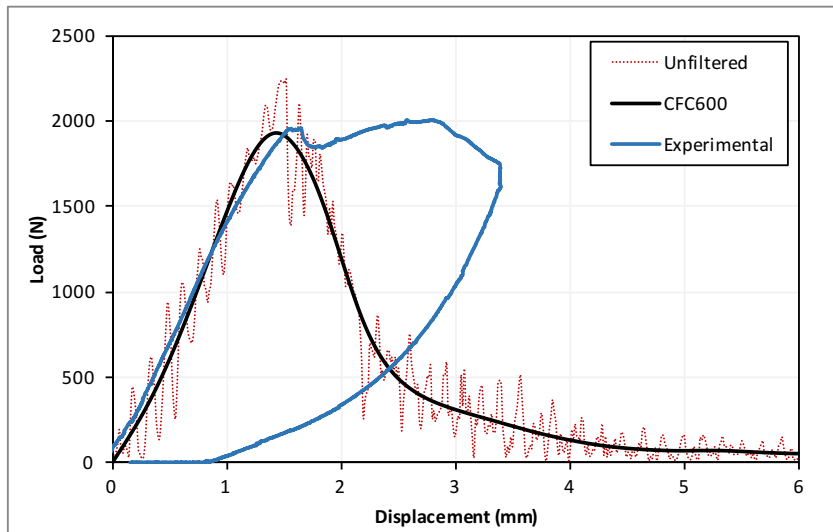


Figure 4.13 – Numerical LV model results for compact compression geometry load, compared to experimental data.

4.3. Coupon level simulations with WP model

A quick comparison of Ladevèze and WP models indicate that the initiation of failure for both is similar, since the definition is for both cases on a strain-level. The damaged – or cohesive – behaviour though is different, since Ladevèze cannot accept a gradual softening, due to equilibrium stability of the explicit solver, while WP, with its localisation algorithm, accepts a cohesive-like softening as prescribed by the material card.

Building up a validated material card with the WP model is different than for the Ladevèze, meaning that the coupon tests that were simulated in the previous paragraph using Ladevèze CDM will appear wrong with the WP failure model. This comes from the different damage behaviour of the two models. The damaged behaviour of Ladevèze CDM cannot accept a gradual softening, due to numerical convergence of the explicit solver, the WP model instead, with its localisation algorithm, accepts a cohesive-like softening, and will therefore give a different straining curve. In the following paragraphs are reported briefly the most representative load cases, compared to the experimental data and with Ladevèze damage model.

4.3.1 Tensile load

If we look at the simple tension case with a $[0]_n$ laminate, again, where the Ladevèze model failed in brittle fashion, as expected, the WP model follows a cohesive-like stress reduction, until the cut-off limit, where the post-damage state with imposed constant stress arises. This is consistent with the numerical model and it's not unexpected, the way WP works makes it unsuited to simulate simpler cases like this one, but it is expected to yield better results for more advanced load scenario.

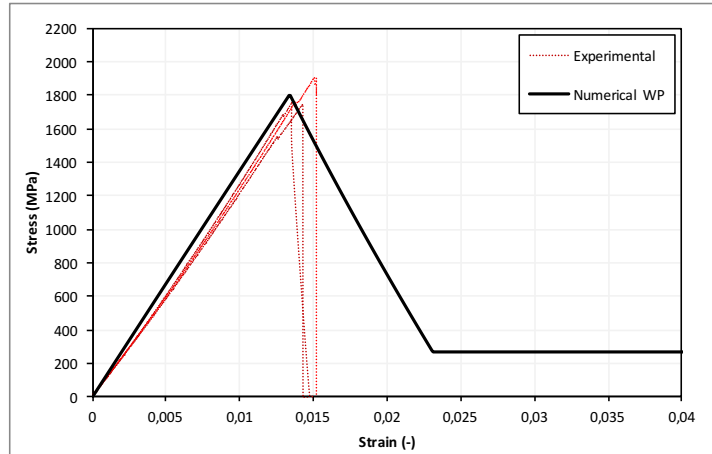


Figure 4.14 – Numerical WP model results for tensile load, compared to experimental points.

4.3.2 Shear load

In this example, the in-plane shear tensile test (paragraph 3.2.3) simulated using both models is compared. As one can see, the WP model (green line) does not correctly simulate the plasticisation and “hardening” of the experimental case. This is again a necessity of the WP model, as it fails to correctly simulate most of the elementary load cases, in favour of more complex real case conditions.

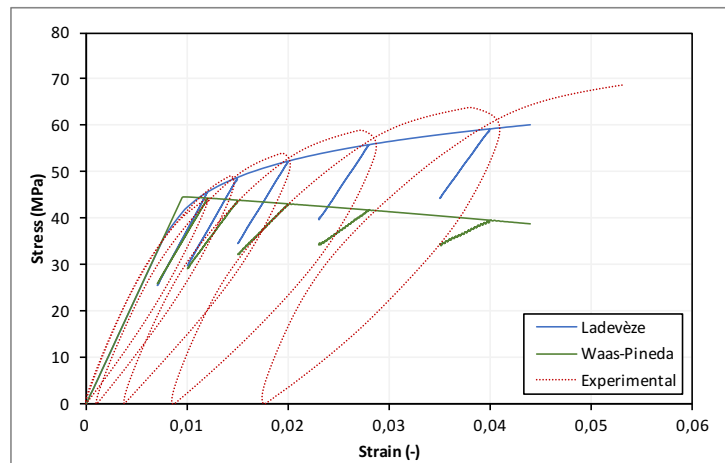


Figure 4.15 – Numerical WP model results for shear load, compared with Ladevèze and experimental points.

4.3.3 In-plane fracture load

Where the WP failure model shows advantages compared to the Ladevèze damage, is in load cases that requires a gradual stress reduction due to propagation of fractures and damages, like in the examples here for the CT and CC specimens. Again, the initiation of failure is overestimated, because the numerical run cannot simulate the plasticity at the crack tip, but the propagation in the tension load case is closer to the experimental results. In addition, we observe that the marked load drop after 3mm displacement (Figure 4.16) matching the experimental curve, indicates that the failure of the constrained end in compressive mode is also correctly depicted in the numerical example.

Regarding the compressive load – recalling results of Chapter 3 – it is expectable that the increase of fracture toughness observed in the physical test cannot be identified in the numerical example, hence the drastic reduction of load after 1,5mm displacement. Nevertheless, the initiation and first propagation are correctly matched. This point will remain an open issue, since the frictional effects of two unconstrained parts penetrating through each other is a difficult phenomenon to simulate in a numerical environment. The need to eliminate elements and guarantee numerical stability goes the opposite way to the experimental evidence of the material crumbling under compression and causing high frictional forces. We will express qualitatively this contribution in the final validation effort of the crush specimen.

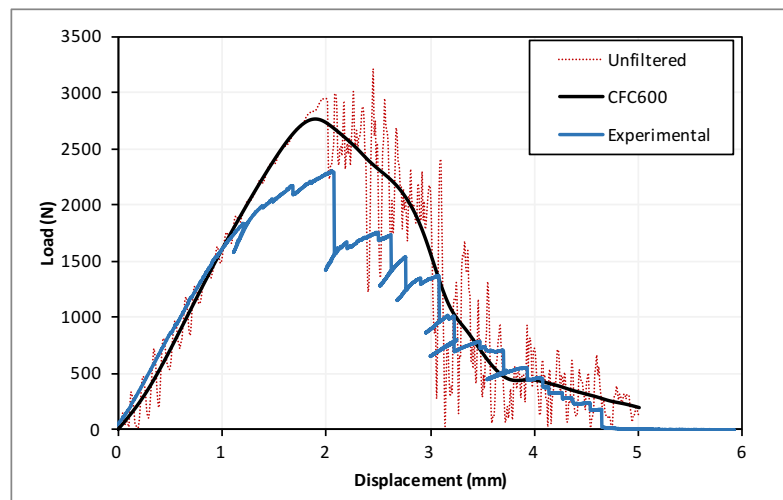


Figure 4.16 – Numerical WP model results for compact tension geometry load, compared with experimental points.

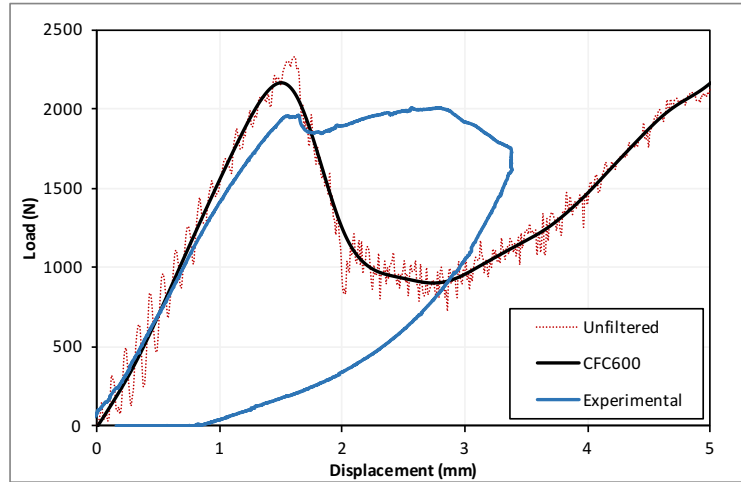


Figure 4.17 – Numerical WP model results for compact compression load, compared with experimental points.

4.4. Setup of crush loading simulations

The experimental campaign was defined in order to build and define a comprehensive meso-model for the damaging phenomena of a specific composite material during dynamic destructive load cases, like a crush event. From analytical analysis of each test, the damage evolution laws for fibre tensile, compressive, matrix shear and transverse damage are defined: strain threshold values are used for fibre damage and linear degradation of the elastic modulus, while matrix damage is based on the strain energy, and a logarithmic evolution is found to fit the experimental sets with high precision. Each test case simulated in the numerical code allowed to gain more confidence with the numerical tool. Final validation is performed on the specific crush load case of the corrugated specimen geometry. A model is built with stacked shells representing the single lamina, connected with cohesive elements to evidence the delamination phenomena. Some of the numerical solutions applied to the crush load case are described before presenting the results. Parameters that are addressed can be divided in two main categories: first some variables that we're unable to identify through experimental testing, and second, purely numerical factors strictly related to the solver, and are not deducible from experimental evidences and investigations. In this paragraph, we will illustrate some of these additional calibration tools, and their influence on results.

4.4.1 Contact algorithms

Contact algorithms were used to ensure that during the simulation, undesired penetration between the geometric boundaries during deformation is prevented. To represent the interaction of the metal loading platen with the specimen, a symmetric node to segment contact with edge treatment was selected. A standard Coulomb friction model with a friction coefficient of 0,3 was used for this interaction. To prevent the stacked shells from colliding and penetrating into each other during the crushing process, a self-contact with edge

treatment was introduced with a friction coefficient of 0,6 to represent the high friction between the delaminated plies which cannot easily slide over each other due to debris friction and fibre bridging.

4.4.2 Boundary conditions

To provide stability during the crush tests, the nodes on the base of the numerical model of the specimen were constrained in all degrees of freedom. The loading platen, was modelled numerically as a rigid body entity with displacement boundary conditions assigned to a single Centre of gravity (COG) artificial node which represents entirely this rigid body. This node was constrained in all degree of freedom except in translation along the axial loading direction, which is assigned a constant velocity of 1mm/ms.

4.4.3 Element elimination strategy

As the shell elements distort due to the degradation of the ply properties, implementation of an element elimination method at ultimate failure was necessary to prevent numerical instability. When using the Ladevèze damage model, the limit strain criterion was selected to eliminate the shell elements when they had reached a prescribed equivalent strain value after damage had propagated in all the plies in each shell element. The limit strains are chosen and calibrated individually for each strain direction to replicate the fracture energies associated to each specific mode of failure and guarantee correct energy absorption.

The WP failure model only allow one equivalent shear strain limit, and this was set to surface in the post-damage state (triggered by the maximum damage limit) and assure stability of the numerical simulation, this value is set to 0,15.

4.4.4 Numerical trigger

Numerical triggers were developed to accurately represent the initiation and propagation of a numerically stable crushing process as observed from visual inspection of crushed specimens. This consist in initiating the splaying of the laminate by offsetting the nodes with respect to the mid-plane. This was used to initiate a central delamination crack which led to a splaying failure with debris wedge. In addition, to limit compressive in-axis instabilities, a chamfer-like solution is created, removing top rows of elements for the outer plies. This prevents to identify the peak load before stable crush initiates, but it is found necessary for avoiding numerical instabilities causing catastrophic crush of the whole structure but ensure a progressive collapse.

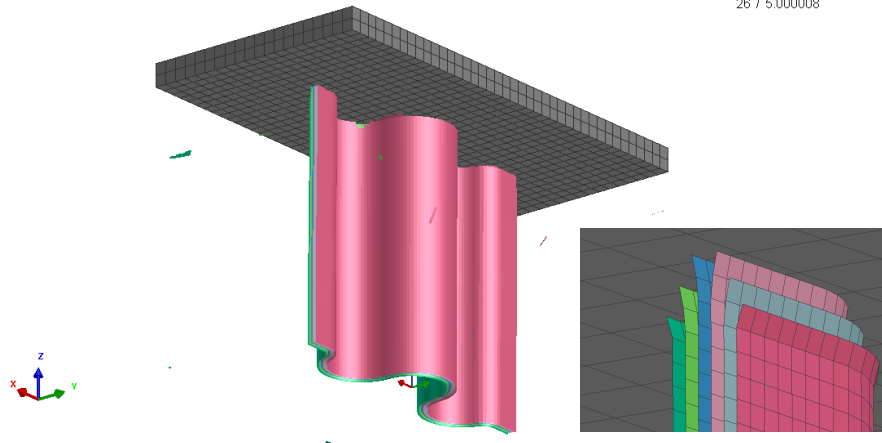


Figure 4.18 – Numerical crush model representation, highlight of the trigger region.

4.5. Validation of crush simulations

At first, we will show the numerical results for sustained load and SEA of the unmodified numerical models as defined during the experimental campaign. As we see, both methods fail to simulate both the crush load and the SEA. In particular, the brittle mode of fibre failure for the LV damage model produces a sawtooth-like crush load where contact is lost at element elimination and restored after displacement of the crush plate progressed. As for the coupon cases above, it is widely accepted to filter the load results to show a smoother curve, at any rate, the filter does not affect the values for the SEA, which have a flat response after a limited transition region. Preliminary results are only slightly better for the WP model, for which the SEA lies at values just above 32J/g, still an underestimation greater than 60%.

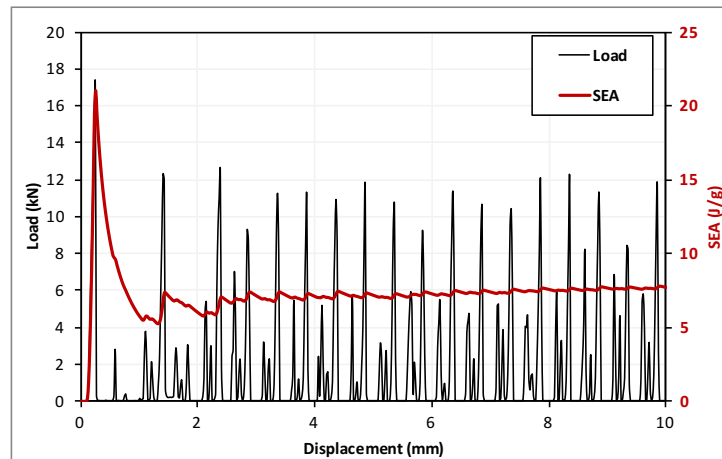


Figure 4.19 – Numerical Ladevèze damage model results for crush specimen load, compared with experimental points.

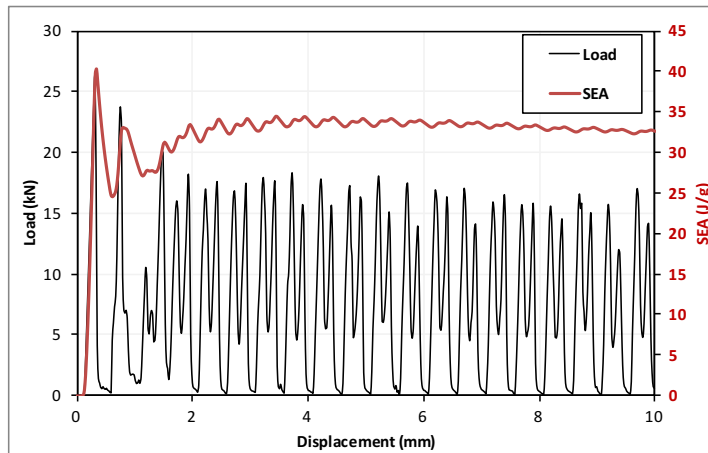


Figure 4.20 – Numerical WP model results for compact compression load, compared with experimental points.

The results shown above indicate that a significant modification for both material models is necessary. To operate this correction, the specific energies associated to fibre compressive and matrix shear damage are increased, without altering the maximum sustained stress, that is saturated at the level of damage initiation. In the LV model, if we express the strain energy with respect to the mesh size and material density, it is possible to calculate the specific energy associated to the given failure mode. This way, using an element length of 0,5mm the specific strain energy before element elimination is set to 110J/g and 50J/g for tensile and compressive load directions, to match the energy levels obtained in experimental tests and better capture the crush energy absorption of the compressive load case. This way, we overcome the limitation of the LV model and get closer to the way WP works, though still not allowing for a softening in the stress-strain behaviour. A similar approach is used also for the shear and transverse damage modes, with an increase in damage thresholds that relate to an overall increase in strain energy to elimination from 14J/g to 23J/g for the shear mode, justified by the weak shear response of the real case.

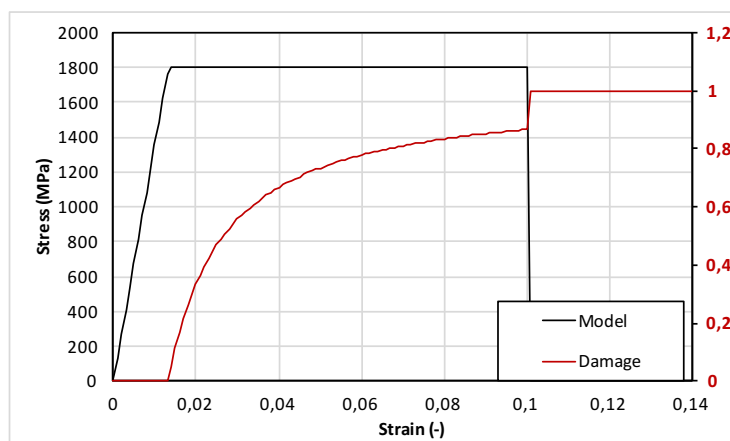


Figure 4.21 – Modified damage model for LV tensile fibre loading.

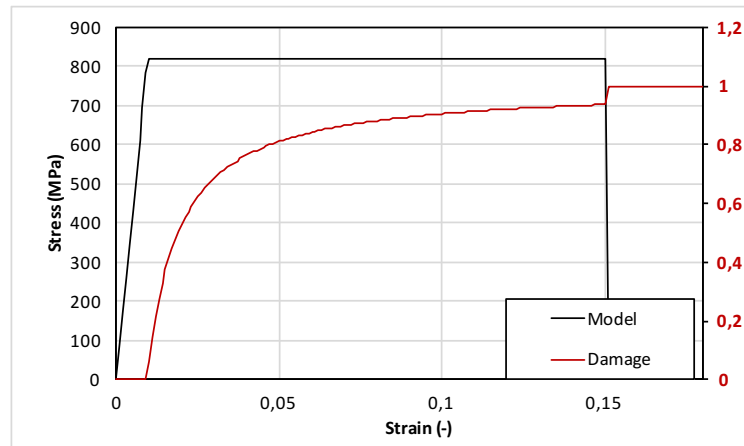


Figure 4.22 – Modified damage model for LV compressive fibre loading.

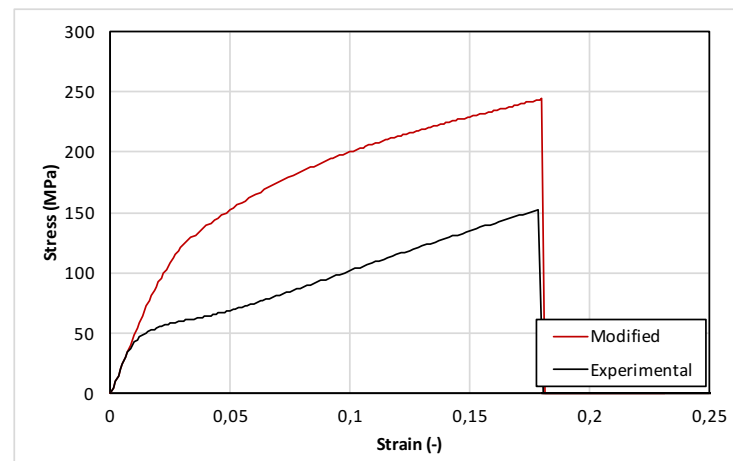


Figure 4.23 – Modified damage model for LV matrix shear loading.

The drawback of this approach, is that it is totally dependent on the mesh size, and element elimination strains must be defined each time the element dimension is changed. The full modified material card for LV model is reported below. Updated results indicate that even after applying some coherent modification, the output loads is still unable to predict correctly the response of the crush tests, indicating a SEA equal to 25J/g, thus closing the gap with the base WP model. The main reason for this is that the numerical models are intrinsically unable to simulate the central debris wedge composed by fragments of material that fails under micro-buckling. Moreover, since the numerical model operates an element elimination at excessive deformation to preserve computational stability, this goes in opposite way to the evidence of a central region consisting of fibre fragments that contribute to the load carrying, that isn't possible to simulate in a numerical environment.

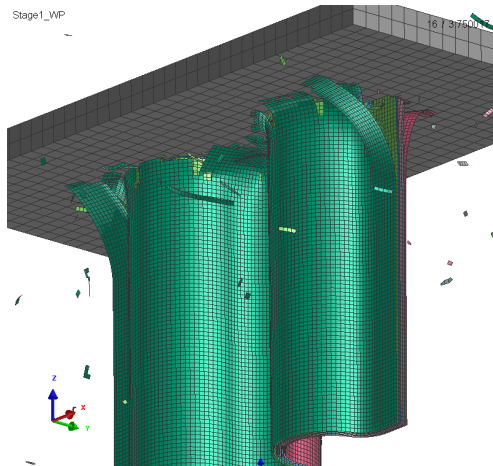


Figure 4.24 – Numerical crush model contour plot, with splaying of outer plies and crushing of the central ones

Table 4.6 – Modified Ladevèze damage user-defined input definition.

Name	Definition	Unit	Value
E0t1	Tensile axial Young's modulus	GPa	135,5
E0c1	Compressive axial Young's modulus	GPa	87
GAMMA	Compressive softening factor	GPa ⁻¹	0
EPSifti	Initial strain axial tensile damage limit	-	0,0133
EPSiftu	Ultimate strain axial tensile damage limit	-	0,0133
EPSifci	Initial strain axial tensile damage limit	-	0,0094
EPSifcu	Ultimate strain axial tensile damage limit	-	0,0094
Dftu	Ultimate tensile damage	-	0,0
Dfcu	Ultimate compressive damage	-	0,0
Y _{0 shear}	initial shear damage limit	GPa ^{1/2}	0,022
Y _{C shear}	Ultimate shear damage limit	GPa ^{1/2}	0,1
d _{max shear}	Ultimate shear damage	-	0,75
Y _{0 trans}	initial transverse damage limit	GPa ^{1/2}	0,1
Y _{C trans}	Ultimate transverse damage limit	GPa ^{1/2}	0,2
d _{max trans}	Ultimate transverse damage	-	0,75
R ₀	Initial plastic yield stress	GPa	0,12
β	Hardening law multiplier	GPa	1,6
m	Hardening law exponent	-	0,6
EPSltu11	Fibre tensile strain for element elimination	-	0,1
EPSlcu11	Fibre compressive strain for element elimination	-	0,15
EPSltu22	Transverse tensile strain for element elimination	-	0,1
EPSlcu22	Transverse compressive strain for element elimination	-	0,15
GAMMApu	Positive shear strain for element elimination	-	0,18
GAMMANu	Negative shear strain for element elimination	-	0,18

In order to obtain results closer to reality using the LV model, we should further increase the ultimate strains to unrealistic values, that in addition lead to unstable runs due to excessive

element deformations. For this reason, we discourage pursuing a better calibration of the LV model, that shows its natural limits with this kind of load cases.

For these reasons, further calibrations are carried out using only the WP model. It is shown that the most sensitive parameters for the load case in object are those related to the relevant failure modes of the structure: the two compressive modes and the matrix shear, the tensile failure modes have a negligible influence. Also, to maintain the efforts under control and limit the computational times, a full factorial design of experiment shown in Table 4.7 is not feasible, but a reduced procedure is applied.

Table 4.7 – Sensitivity analysis of significant Waas-Pineda damage user-defined inputs.

Input	Investigated Values
EFR11c	Base, +50%, 2x, 3x, 4x
EFR22c	Base, +50%, 2x, 4x, 8x
EFR12	Base, +50%, 2x, 4x, 8x

The strength of the WP model is that the user can directly alter the specific fracture energies while maintaining the initiation unchanged. In addition, since the solver solves internally the equivalent traction-separation behaviour for the specific element size, it overcomes the mesh-sensitivity of the LV model. This allows to have a more straightforward correlation between the input parameters and the ultimate SEA of the model. Numerical input parameters for ultimate damage (Dmax) and element elimination (EPSIslim) are left unchanged, since the stability of the run, affected by the deformations and stiffness of the elements, is determined by these two parameters.

Table 4.9 – Test chart sensitivity analysis for selected WP damage user-defined input definition.

ID	EFR11c	EFR22c	EFR12	SEA (J/g)
0	Base	Base	Base	33,3
1	Base	Base	Base	34,7
2	50%	Base	Base	46,3
3	Base	2x	Base	36,8
4	Base	Base	2x	36,0
5	2x	Base	Base	61,4
6	Base	4x	Base	47,2
7	Base	Base	4x	44,1
8	2x	4x	Base	70,2
9	2x	4x	4x	80,4
10	4x	Base	Base	123,9
11	Base	8x	Base	53,7
12	Base	Base	8x	58,0
13	3x	8x	8x	130,0
14	3x	2x	2x	100,1

Table 4.8 – Base Waas-Pineda damage user-defined input definition.

Name	Definition	Unit	Value
IFL11	Axial initialisation mode flag	-	0
VAR11	Tensile axial limit	GPa	1,8
VAR11c	Compressive axial limit	GPa	0,82
IFL22	Transverse initialisation mode flag	-	0
VAR22	Tensile transverse limit	GPa	0,036
VAR22c	Compressive transverse limit	GPa	0,185
VAR12	Shear limit	GPa	0,075
ETA	Mixed mode exponent	-	1
EFT11t	Axial tensile fracture energy	J/mm ²	0,1075
EFR11c	Axial compressive fracture energy	J/mm ²	0,048
EFR22t	Transverse tensile fracture energy	J/mm ²	0,00047
EFR22c	Transverse compressive fracture energy	J/mm ²	0,001792
EFR12	Shear fracture energy	J/mm ²	0,001792
Dmax	Maximum damage	-	0,5
EPSslim	Equivalent shear strain limit	-	0,15
Ifelim	Element elimination behaviour flag	-	1

The sensitivity analysis indicates that, of the three parameters investigated, EFR11c is by far the most important, contributing to more than 80% of the total energy using the base energy values., Second is EFR22c, the compressive fracture energy in direction parallel to the fibre, accounting for around 10% of the crush force, other parameters, including delamination modes, account globally for the remaining 10% of the crushing load.

Following the scheme indicated in Table 4.9, the SEA level for various modified parameters is shown. Iteratively, the target value of 100J/g is found by increasing the fracture energies to three times the initial value for EFR11c, and twofold for EFR22c and EFR12, respectively to 144J/m² for the former and 3,6J/m² for the latter ones. It must be noted that this approach is purely numerical and should be further validated on multiple geometries, at the time of writing unavailable, but planned for future activities.

It must be further noticed that with these modifications, the simulation always accomplished to give a correct macroscopic reproduction of the deformed shape of the specimen, with a relative constant value for specific energy absorption throughout the stroke, practically always establishing a quasi-static mode of crushing. This is motivated by the fact that the parameters governing the element elimination and the post-damage state are maintained throughout all simulations. A comparison of simulation run ID 14 with the experimental plot is offered in Figure 4.26, where it is appreciated how the unfiltered load maintains the sawtooth-like shape, oscillating equally between 0 and 40kN, resulting in an average crush load of 20kN, similar to the physical case.

In conclusion, we appreciate the fact that this damage model is fully flexible in the definition of the crushing load, and is able to guarantee similar and stable run for varying input parameters. The main obstacle though, is that the determination of some input parameters required for the definition of the material characteristics is difficult. In fact, besides properties easily obtainable with standard test methods, the determination of certain fracture energies requires complex procedure, still not described in a standard reference, and specific

expensive equipment, or in alternative, a long tuning procedure focused on the particular material system used in the analysis. This aspect, therefore, interferes with the expectations of a quick and economic tool to speed up the building block approach process.

Further investigation suggested, regard for example the influence of the profile geometry on the global crush response, the layup – in particular, the ratio of plies at 0° orientation on the total laminate – and only on a later moment, the investigation of different materials.

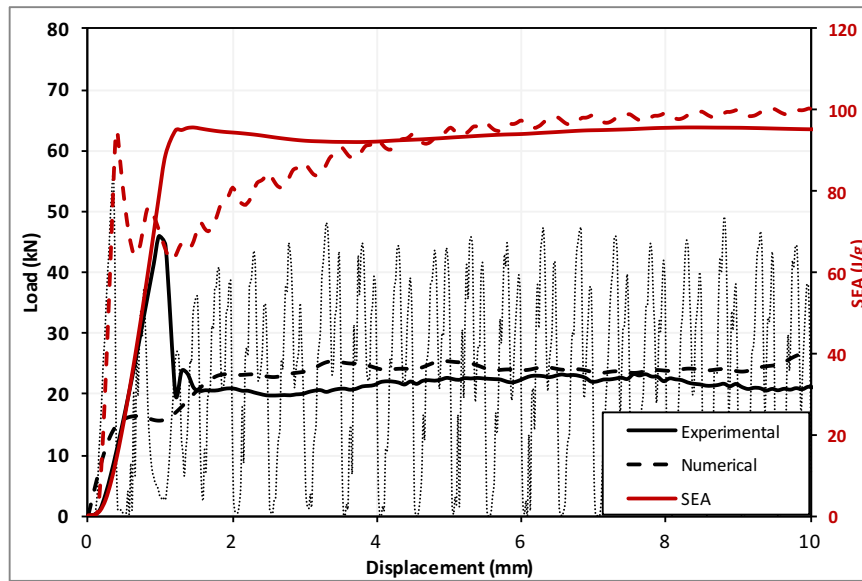


Figure 4.26 – Numerical WP modified damage model results for crush specimen load, compared with experimental points. full lines represent experimental data, dashed lines numerical, SEA curves in red (right axis).

CHAPTER 5

MEASUREMENT OF TEXTILE PERMEABILITY IN COMPOSITE INJECTION PROCESSES

Resin injection processes are gaining a lot of interest in the composite industry because they allow significant cost savings thanks to the vast increase in production rates and reduction of the sheer cost of materials, and can ultimately offer interesting performance.

With resin transfer moulding (RTM) we typically indicate a family of manufacturing processes that consist in the injection of the curing resin, typically thermoset, in a closed mould, where the “dry” reinforcement are placed beforehand. Advancement in the RTM technology, through the increase of injection pressures, made possible to reach fibre volume fractions comparable to those obtained in autoclave technology, until recently, the benchmark regarding composite material performances.

The interest in this technology is also due to the vastly superior production rate, when compared to traditional manufacturing methods. Whereas a part produced in autoclave will require a cycle time of a couple of hours for the curing of the resin, this limit is overcome in RTM technologies, where resin kinetics can be much faster, and parts can be infused and cured in a matter of few minutes.

A natural issue of this technology is the need to precisely predict the flow front advancement in the closed mould, to avoid the presence of dry spots, areas with poor resin filling, porosities, and so on. This is achieved through the correct positioning of injection and venting ports (points where vacuum is drawn) and the precise characterisation of the textile reinforcement.

The latter, can be considered like a porous medium through which the fluid flows, and the physical model governing this phenomenon is taken from the experimental studies of Darcy in the late '800 [49], and subsequently adopted in geological and oil engineering to study the flow of fluids through rocks. The basic formulation of the physical phenomenon can be summarised in the following expression:

$$\mathbf{V} = -\frac{\mathbf{K}}{\mu}\nabla P \quad 5.1$$

where the three-dimensional velocity of the flowing fluid \mathbf{V} is proportional to the pressure gradient times the 3x3 permeability matrix \mathbf{K} over the dynamic viscosity of the fluid μ .

In the general case, the permeability matrix is a dense matrix, but thanks to the tensorial nature of the problem, it is found that a coordinate system exists which renders the matrix diagonal. This coordinate system describes the principal directions for the permeability of the

fibre reinforcement, which is the porous medium of the RTM process. The simplified matrix will then require the determination of only three distinct values, representing the directional permeabilities in the principal directions.

$$[K] = \begin{bmatrix} K_1 & 0 & 0 \\ 0 & K_2 & 0 \\ 0 & 0 & K_3 \end{bmatrix} \quad 5.2$$

Aim of the process designer is the determination of the permeability matrix of a fibrous reinforcement, with the goal of predicting the fluid flow in a complex component geometry, and optimise the process conditions, as well as the distribution of the injection points in order to maximise the filling factor, reduce dry spots and doing so in the shortest time possible.

5.1 Experimental determination of permeability

Several simplified experimental procedures have been proposed for the determination of the permeability tensor that rely on closed form solutions of the Darcy problem [50-54], we can organise them according to these boundary conditions:

- Nature of the driving force:
 - o Imposed pressure (Dirichlet)
 - o Imposed flow (Neumann)
- Flow morphology:
 - o Linear
 - o Radial

Regarding the driving force, in the case of imposed pressure, we will refer to an unsaturated flow, where the cavity is filled during the test and the flow front is measured vs time. In the case of imposed flow, the resulting experimental case is that of a saturated flow, that is, when the cavity is filled during the whole test, and in stationary flow conditions, the pressure drop in the cavity is measured to infer the permeability.

With respect to the second point, the morphology of the flow can be either linear, in the case of mono-dimensional problem, or radial, where the flow is allowed to exist in a 2D plane.

The combination of these BC results in four different experimental setups that can be used for the complete determination of the permeability tensor and the orientation of its principal directions. In particular for the case of composite materials, because of a symmetry plane in the reinforcement along its plane, we can already identify the third principal direction (along Z) to be orthogonal to the plane containing the plies. The permeability in this direction is the most difficult to measure, but it is often discarded altogether because the thickness of the reinforcement is typically very small, compared to the other two dimensions, therefore, we often assume the permeability to be only a 2D problem.

This leaves us to the determination of only two permeabilities and one principal direction (the second being orthogonal to the first within the reinforcement plane). With respect to the natural orientations of the reinforcement, given by the direction of the fibres, the

permeability tensor will generally be offset by a certain angle. It is therefore common to refer the principal permeabilities direction with respect to the fibre orientations through an angle.

5.1.1 Unsaturated linear flow

The closed form solution of Darcy's equation for the unsaturated linear flow has the following form:

$$\frac{dx}{dt} = \frac{K_{xx}}{\mu \varepsilon} \frac{\Delta P}{x(t)} \quad 5.3$$

Where terms still not described are on the left hand, the position x of the flow front at time t , on the right hand the permeability in the main flow direction K_{xx} , the pressure difference between inlet and outlet ΔP , and $\varepsilon = 1 - v_f$ is the void ratio, that is the portion of volume not occupied by the fibres. This term appears because the term on the left hand is the apparent velocity of the fluid, as seen by an observer, not to be mistaken with the intrinsic velocity of the fluid V . A schematic representation of the problem is shown below.

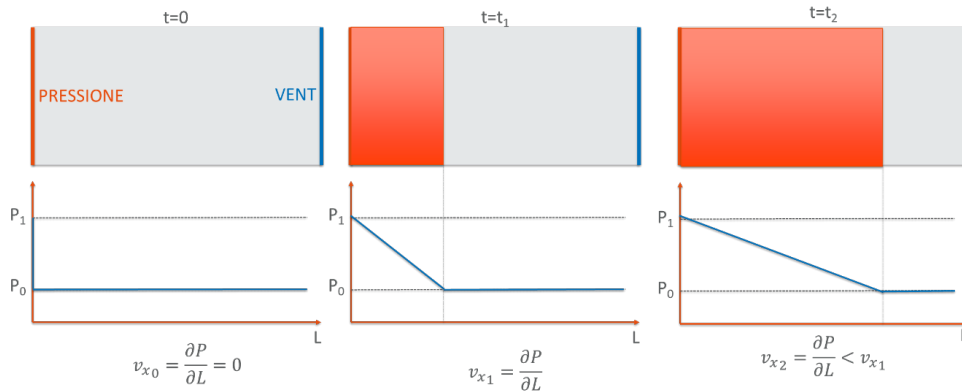


Figure 5.1 – Visual schematisation of the unsaturated linear flow with pressure distribution along the length.

Imposing the initial conditions $x_0=0$ and $t_0 = 0$, we solve the 5.3 to obtain the integral form of the differentials:

$$\int_0^{x_i} x(t) dx = \int_0^{t_i} \frac{K_{xx} \Delta P}{\mu \varepsilon} dt \quad 5.4$$

$$\frac{x_i^2}{2} = \frac{K_{xx} \Delta P t_i}{\mu \varepsilon} \quad 5.5$$

That gives a quadratic relation between time and flow position. Rearranging 5.5, the permeability in the mono-dimensional case is found:

$$K_{xx} = \frac{x_i^2 \mu \varepsilon}{2 \Delta P t_i} \quad 5.6$$

In order to identify the principal directions and the offset using linear injection experiments, we have to perform tests at least in three directions in the plane; for simplicity, 0, 45, and 90 degrees orientations are chosen. The principal directions are then found by:

$$K_1 = K_{exp}^0 \times \frac{\alpha_1 - \alpha_2}{\alpha_1 - \frac{\alpha_2}{\cos(2\beta)}} \quad 5.7$$

$$K_2 = K_{exp}^{90} \times \frac{\alpha_1 + \alpha_2}{\alpha_1 + \frac{\alpha_2}{\cos(2\beta)}} \quad 5.8$$

$$\beta = 0,5 \times \tan^{-1} \left(\frac{\alpha_1}{\alpha_2} - \frac{\alpha_1^2 - \alpha_2^2}{\alpha_2 \times K_{exp}^{45}} \right) \quad 5.9$$

Where the two parameters α_1 and α_2 are defined as follows:

$$\alpha_1 = \frac{K_{exp}^0 + K_{exp}^{90}}{2} \quad \alpha_2 = \frac{K_{exp}^0 - K_{exp}^{90}}{2} \quad 5.10$$

The procedure to obtain the equations 5.7 to 5.10 is taken from the works of Weitzenbock [54]. The mathematics behind this demonstration are quite lengthy and elaborated, therefore the details are left to the reader for in-depth analysis.

5.1.2 Unsaturated radial flow

The experimental setup corresponding to a radial flow with unsaturated condition is more complex to realise compared to the linear case, but offers the advantage of needing only one experimental test to determine in one step the two directional permeabilities and the offset angle. The closed form solution takes the following form

$$K = \left\{ b_i^2 \left[2 \ln \left(\frac{b_i}{a} \right) - 1 \right] + a^2 \right\} \frac{1}{t_i} \frac{\mu \varepsilon}{4 \Delta P} \quad 5.11$$

where a is the inlet diameter and b is the radius of the flow front. It is interesting to notice that as a consequence of this expression, the flow front of this radial injection takes the form of an ellipse with the local radius proportional to the square root of the directional permeability. The principal axes of the ellipse then indicate the principal permeabilities, and the offset is also easily found visually.

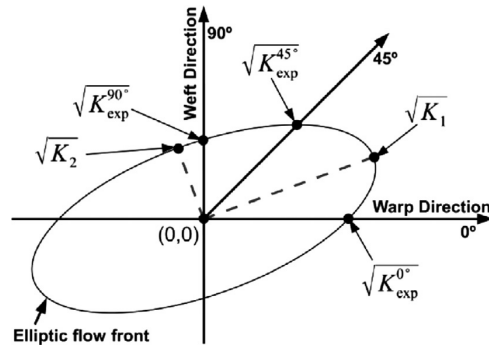


Figure 5.2 – Visual schematisation of the unsaturated radial flow front with graphical representation of the axes of principal permeabilities.

5.2 Experimental setup

Goal of this experimental campaign is to characterise a fibre layup for the future simulation of an RTM process. The testing material consists of a biaxial 600gsm glass fibre stitched with 18g PP and a 450gsm short fibre MAT with random orientation attached to one side. The global thickness of the textile is 3mm.

We agreed to conduct all our tests using a simplified 1D linear flow test bench, since the radial flow setup comes with an increased complexity. Important aspect of this setup is the geometric proportions of the mould cavity. Thanks to the efforts of the group that participated in the two permeability benchmarks [55] and [56], an empirical requirement for the mould indicates a minimum length to width ratio of 4:1 and a goal thickness of 4mm. These dimensions come from a compromise between through the thickness and edge boundary effects.

Two mould cavities are machined from a steel block with 4 and 6mm depth, the final dimensions are 440x100mm with a useful length for the textile of 400mm length. The 20mm free space for inlet and outlet are required to initiate a stable flow front and prevent potentially dangerous migrations of the fluid to the vacuum apparatus. To this end, a buffer volume is realised, this works additionally as a device to reduce fluctuations of pressure at the vent. On top of the mould, a Plexiglas cover is positioned and fixed using a set of screws, a ring sealing rubber guarantees the contact between the two mould halves and avoids leakages. Inlet and outlet ports are connected to the top plate for ease of construction. Marks at 10mm intervals are drawn on the Plexiglas covers to aid identification of the flow position. The full setup is shown in picture below, note the two connecting hoses, the sealing gasket, the buffer volume (top right) with a Y junction to reverse the flow for convenient oil expulsion.



Figure 5.3 – Permeability setup manufactured and installed.

The pressure gradient of the setup is done using a vacuum pump that can be regulated at an arbitrary value between 0 and 1 bar gauge. As a compromise between sufficiently slow flow front and minimal pressure losses a value of 0,5bar is chosen. Another advantage of the vacuum pump compared to a positive pressure one is that the closing of the mould is inherently guaranteed.

As target fluid for the experiments we chose a synthetic oil 15W40, this proved to be better than tests using resin because the oil is non-reactive and much easier to clean after impregnation, overall it requires less time and effort. The viscosity of the fluid is characterised at room temperature using a Brookfield viscosimeter and is measured at 188cPs.

The fibre volume fraction is measured by submerging a sample of the material in a graduated cylinder and measuring the increase of water level V_{tex} . By knowing the areal dimension of the sample $L*w$, we can identify the specific areal volume of the textile expressed as volume per unit area (m^3/m^2):

$$\phi = \frac{V_{tex}}{L * w} \quad 5.12$$

At this point, the volume fraction occupied by the textile in a given mould is simply equal to the number of plies times ϕ divided by the thickness t of the mould cavity:

$$V_f = \frac{n_{plies}\phi}{t} \quad 5.13$$

5.3 Test results

Samples of the materials are cut to dimension and laid up to fill the 6mm cavity (2 layers required). Three repeated measures are done at three prescribed orientations for a total of 9 trials. The test is monitored using a camera to acquire a full video of the injection process and a chronometer is used to mark the time. Stopping at each frame when the flow passes the 10mm marks, we can plot up to 40 points to get a plot of the flow position vs. time, an example plot is shown.



Figure 5.4 – Example of acquired frame during the impregnation test, notice the uniform linear flow front.

In some cases where race tracking occurred, it is important that the region affected by improper filling is limited, and that the measure of the flow position is done ideally at the middle section of the width. In case of highly non-uniform flow front shape like in Figure 5.5, the measure cannot be considered acceptable. The reasons correlated to this effect can be many, but are mainly due to improper filling of the cavity, when the textiles don't fill perfectly the side of the mould, or when the closure is not perfect because of fibre bundles overlapping the sealing, or ultimately – when this effect is persistent – can signify a poor setup configuration. In this experience, several configurations of the sealing gasket were tested until a satisfactory filling was achieved.

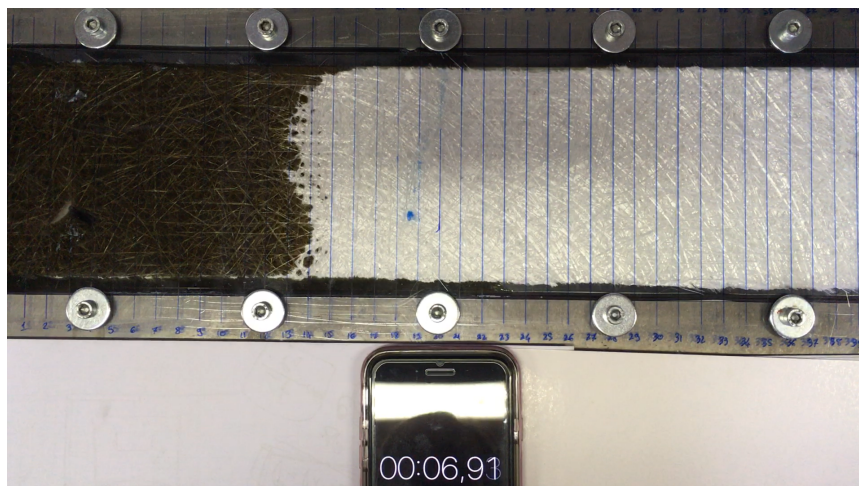


Figure 5.5 – Example of acquired frame during the impregnation test with non-uniform flow front and race tracking on both sides.

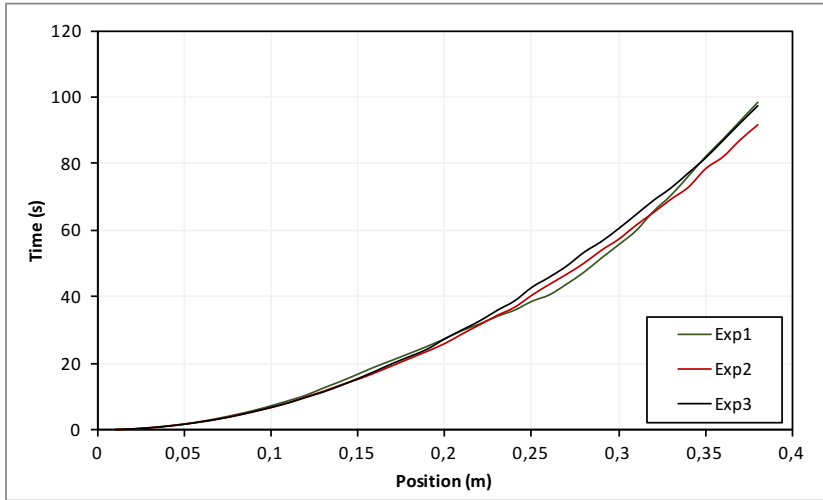


Figure 5.5 – Example of acquired frame during the impregnation test, notice the linear flow front.

The permeability can be calculated directly using the 5.6 for each data point $x_i(t_i)$ and plotting the curves like shown in Figure 5.5. This method is useful to identify possible issues during the test, for example, high oscillations of the permeability during the test can signify that the test boundary conditions were not constant throughout the test (see curve Exp 1 below). These oscillations can for example be caused by variations in the applied pressure difference, improper filling flow, or small discrepancies in the textile weight and layup.

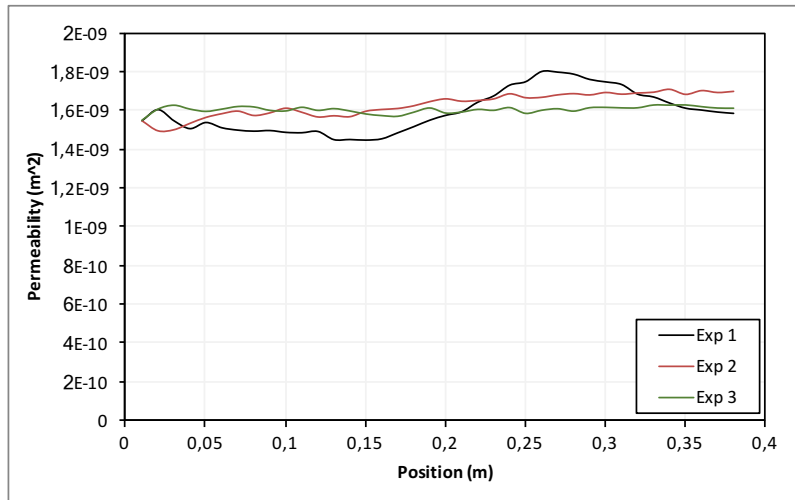


Figure 5.5 – Example of acquired frame during the impregnation test, notice the linear flow front.

To compensate for these oscillations and possible measurement errors, it is advised to calculate the permeability using a least square fit method like the one proposed by [57]. The method, simplified for constant pressure difference $P(t) = P$ yields:

$$x_i(t_i) = \left[\frac{2K}{\mu\varepsilon} P * t_i \right]^{1/2} \quad 5.14$$

Then the least square fit, is obtained by defining the squared error function ϵ^2 , where it is set $a = \sqrt{2K/\mu\varepsilon}$ goal of our nonlinear fit and imposing its derivative with respect to a equal to zero:

$$\epsilon^2 = \sum_{i=1}^n (x_i - a\sqrt{Pt_i})^2 \quad 5.15$$

$$\frac{d\epsilon^2}{da} = \sum_{i=1}^n (x_i - a\sqrt{Pt_i}) \sqrt{Pt_i} = 0 \quad 5.16$$

This can be finally solved for a :

$$a = \frac{\sum x_i \sqrt{Pt_i}}{\sum Pt_i} \quad 5.17$$

To give the least square fit permeability:

$$K_{LSF} = \frac{a^2 \mu\varepsilon}{2} \quad 5.18$$

Values obtained with this method for all nine experimental tests are summarised in Table 5.1. As last step, the principal permeabilities are found using the expressions 5.7 to 5.10 introduced above, starting from the average values of three repetitions of K for each direction. Values are reported in Table 5.2.

Table 5.1 - Summary of determined experimental directional permeabilities.

Permeability	$K 0^\circ (10^{-9} \text{ m}^2)$	$K 45^\circ (10^{-9} \text{ m}^2)$	$K 90^\circ (10^{-9} \text{ m}^2)$
Trial 1	1,459	1,640	1,646
Trial 2	1,461	1,675	1,726
Trial 3	1,511	1,605	1,723
Average	1,477	1,640	1,698

Additionally, we can represent graphically the distribution of permeabilities at various orientations. This is obtained by calculating the effective permeability K_{eff} at a certain orientation θ using the following:

$$\sqrt{K_{eff}} = \frac{\sqrt{K_1 K_2}}{K_1 \sin(\theta) K_2 \cos(\theta)} \quad 5.13$$

which is the geometrical description of the ellipse introduced in figure 5.2. This graph is useful to have a qualitative idea of the flow distribution of the given layup, because it mimics the real flow propagation in case of radial flow propagation.

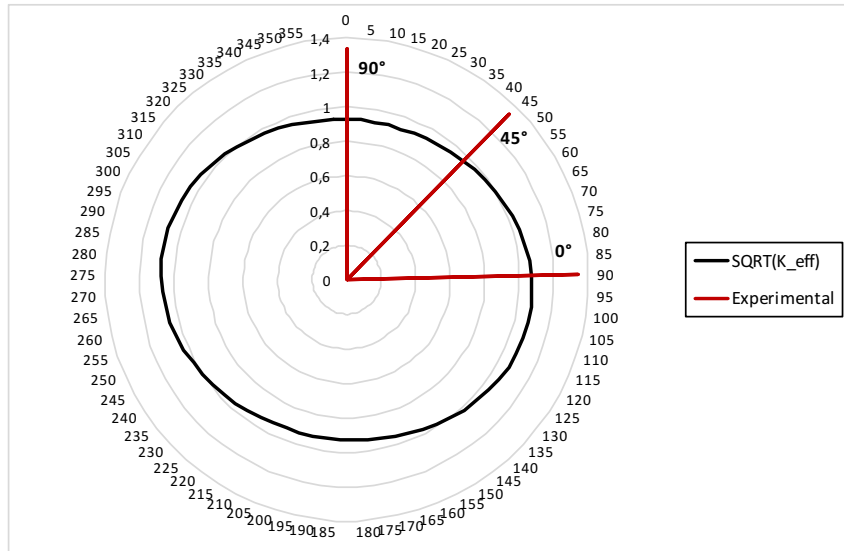


Figure 5.5 – Graphical representation of radial flow front propagation, with highlighted the directions measured in linear channel flow.

Table 5.2 – Summary of calculated principal textile permeabilities.

	$K_1 (10^{-9} \text{ m}^2)$	$K_2 (10^{-9} \text{ m}^2)$	β (deg)
Principal permeability:	1,715	1,465	-14°

5.4 Validation

This experimental activity described represent only one section of a broader activity that took part in a collaboration between an industrial manufacturer of nautical components and the software developer ESI. The material characterisation was used as input to the FE software Pam-RTM and validated a real component produced by RTM. The numerical model developed also dealt with the discretisation and numerical modelling of a sandwich structure, and additionally considered the resin cure kinetics and viscosity curves identified thanks to the department of industrial chemistry at the University of Bologna.

Final results indicate a perfect agreement in the filling time between numerical simulation and experimental case, with minor differences of filling time within 7%, intrinsic of the manufacturing process, attributed to the imprecisions of hand-layup and uncertainties of the process to be expected in a production environment, like imposed pressure, process temperature, deviation in the resin composition, and so on.

CHAPTER 6

3D REINFORCEMENT TECHNIQUES FOR CFRP TO METAL JOINTS

In the past few years, great advancements have been done in the aeronautics and automotive industry regarding design and assembly of composite structural parts, nevertheless, their inherent poor through the thickness strength and limited resistance at high temperature, means that metal components are still necessary for a significant number of key components. This leads to the requirement of efficient and safe joining solution between composite and metal components. Due to the different elastic and thermal properties of composite and metals, it typically results that the connecting regions represent the weak link of the assembled structure. Traditionally, these joints are made using mechanical fasteners such as bolts or rivets, but this method is fundamentally flawed, as drilling through the composite reduces the load carrying capability of the material, creates stress concentrations and initiates delaminations, often already at the drilling process. To minimise these drawbacks, the joining sections, contact areas and number of fasteners are increased, often incurring in unwanted weight penalties. Adhesive bonding presents a potential alternative, having negligible increase in weight, but require careful surface preparation and is limited by the strength of the interface material. In addition, it offers poor safety measures, as once failure propagates at the interface, it will lead to complete detachment of the adherends. In this scenario, a hybrid bonded-bolted approach offers the best compromise between weight minimisation and structural redundancy, though carrying over costs and time disadvantages of both solutions. For this reason, several novel technologies are under development as potential alternatives to traditional joining methods, to improve the integration between metal and CFRP components.

Taking advantage of the geometrical flexibility and freedom of design opened by recent manufacturing processes like additive manufacturing, several concepts appeared in recent years, with the aim of improving on the concept of adhesive bonding by maximising the surface contact area, thus the shear strength, and introducing geometrical features to also increase the peel toughness, when compared to a standard bonded joint.

6.1 Classical 3D-reinforcement techniques

Among non-traditional joining techniques involving 3D reinforcements [58], the first example is stitching. This involves sewing a high tensile yarn (carbon, glass or aramid) through the thickness of the laminate structure using a sewing machine. Aramid and glass are the preferred materials to be employed as the reinforcement yarn because of greater flexibility. Prior to curing, a stack of plies is penetrated and locked together with the aid of a hollow needle and bobbin threads. The final stitched composite is then consolidated via resin

film infusion or resin transfer moulding. Important aspects of the style of stitching is that it should cause the least fibre distortions and therefore less weakening of in-plane mechanical properties. However, distortions of both in-plane fibres and fibres within the stitches are unavoidable as fibres are bent to accommodate the stitches, and stitches are crimped during laminate consolidation/compaction.

Hence, a more advanced technology, similar to stitching, was developed – “tufting”. Tufting is a single-thread sewing method in which the formation of loops is possible with a loose and tension-free insertion of a threaded needle that has less adverse effects on the material. The needle pushes the yarn inside the preform using an elastic foam tool and its removal is made along the opposite trajectory; thus, only access to one side of the structure is required. Prior to resin infusion, the thread pathway allows the formation of a loose loop that remains in place relying on the friction between the yarn itself and the host fabric preform. The actual reinforcement comes only after resin injection from the bonding between matrix and thread. Stitching reduces in-plane properties by up to 20%, while drop-downs with the Tufting method are below 10%. On the other hand, “tufts” and “stitches” have shown to improve compression strength after low velocity and ballistic impacts of around 95% and 50%, respectively. The presence of stitches on CFRP laminates was also found to improve the delamination resistance against crack propagation under both modes I and II of about 15 times and 4 times, respectively.

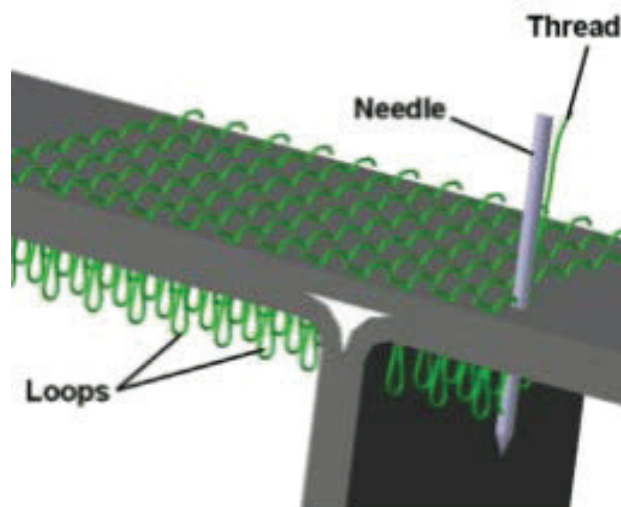


Figure 6.1 –Tufting on a T joint.

Alternative to stitching and tufting is a technology named Z-pinning. In contrast with previous technologies, that are only suitable for textile laminates made by using dry fabric plies, Z-pinning can be used to reinforce prepreg materials, thus are of great interest in aeronautics, where this technology is still the most used. Z-pins are short rods or pins made from extruded wire material with high strength-to-stiffness ratio, (titanium alloy, steel or fibrous carbon composite) that act as thin nails capable of locking the different laminate layers together by a combination of friction and adhesion. With this technology, access to only one side is possible, which is a great advantage in relation to other classical techniques. Z-pins are used in a diameter range of 0.15 to 1.0 mm and are present in laminates with a volume density in the

range of 0.5 to 4%, which is equivalent to about 8 to 70 pins/cm². This is an effective and simple way to enhance delamination resistance, damage tolerance, out-of-plane stiffness and joint strength of prepreg laminates. The bridging effects produced by z-pins can increase the delamination resistance of up to 160% and 100% under modes I and II loadings, respectively. The improved delamination toughness also increases the impact resistance and reduces the damage area, with the z-pinned laminates displaying damage areas of up to 64% smaller than the unpinned laminates. Suppression of very short delaminations is not within the expected benefits provided by this technique; this means that z-pinning is only effective in the propagation stage rather than the damage initiation stage. Residual compression- after-impact (CAI) strength is also improved by z-pinning, with the pinned laminates presenting approximately 45% higher residual strength than the unpinned counterparts. Important improvements in the z- properties of CFRPs, such as tensile modulus, can also be achieved by introducing z-pins, with the out-of-plane stiffness of such laminates being increased by 50% or more with relatively modest amount of pins (2 to 4% by volume). Effectively, such gains on the through-thickness properties are only possible by sacrificing the in-plane mechanical properties. Although a general agreement on the causes for deterioration of such properties exists, the extent of damage induced to the in-plane properties due to the presence of z-pins, reported on the available papers, is not consistent. To be able to understand the benefits and damage induced to laminates caused by z-pinning, a full understanding of the microstructural changes is essential. It is believed that the harm induced to the in-plane elastic and strength properties is due to the microstructural damage caused by z-pinning, particularly fibre breakage, waviness and crimping, resin-rich zones, pin offset, swelling of the laminate and cure stresses.

6.2 Bonding techniques using additive manufacturing

In contrast to conventional manufacturing methods, additive manufacturing (AM) is based on an incremental layer-by-layer material deposition [59]. As such, most relevant AM technologies commonly use powder or wire as a feed material, which is selectively melted by a heat source and consolidated through cooling to form the part. AM has attracted much attention over the past years due to its inherent advantage of unmatched design freedom. These techniques, at first limited to the rapid manufacturing of prototypes is now an available alternative to standard manufacturing technologies, thanks to advancement that made possible to reach higher densities and production rates, so that today it has become possible to reliably manufacture parts with certain AM processes for a number of materials of engineering interest like steel, aluminium and titanium.

Taking inspiration from the joining techniques introduced above, and with the advantage of recent AM technologies, a series of innovative metal to composite joining solution became possible. Common denominator of these solutions is the use of small pins (<1mm diameter) of various shape and structure to maximise the areal contact and load transfer between the two bodies. The following paragraph offers a review of techniques proposed in literature for joining metal with fibre reinforced composites taking advantage of additive manufacturing for the metal part.

ratio that maximises fracture energy is found at $L/D = 3.6$.

Table 6.1 – Single pin pull-out specimen configurations

Test type	D (mm)	L (mm)
Single_05/2	0,5	2
Single_05/3	0,5	3
Single_05/4	0,5	4
Single_1/3,5	1	3,5

6.2.2 Pin shape investigation

Another published research from Nguyen [61] dealt with differing pin shapes, testing differing features while maintaining the overall pin dimensions. These four geometries are (see picture for specification):

- Cylindrical (baseline) with $D = 1\text{mm}$ and $L = 3,5\text{mm}$;
- Grooved profile
- Pyramid head
- Helical shape

Once again, experimental tests rely on single-pin pull-out traction tests. Results are discussed below.

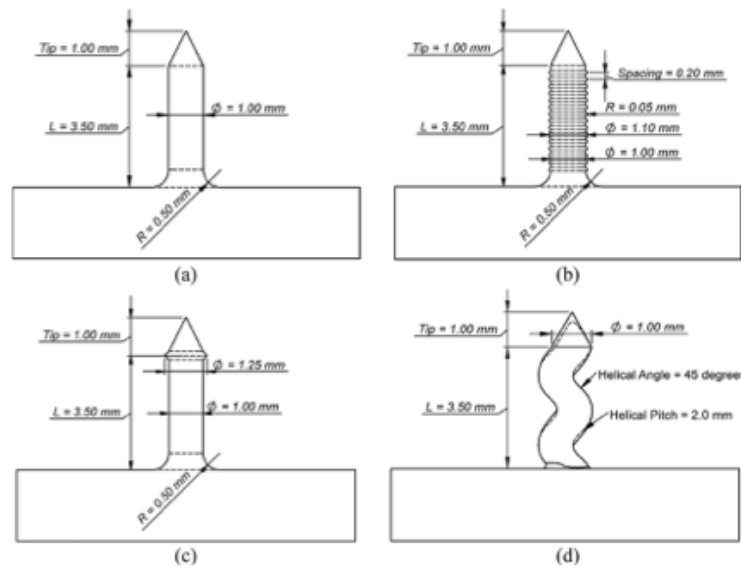


Figure 6.3 - Single pin specimen pin geometries. (a) Cylindrical, (b) grooved, (c) pyramid, and (d) helical.

In terms of single pin pull-out, cylindrical pins and grooved surface pins exhibited progressive pull-out while pins with pyramid tip and helical shape led to composite fracture. Despite the difference in failure mode, all the pins studied had higher maximum load and pull-out energy than the baseline geometry.

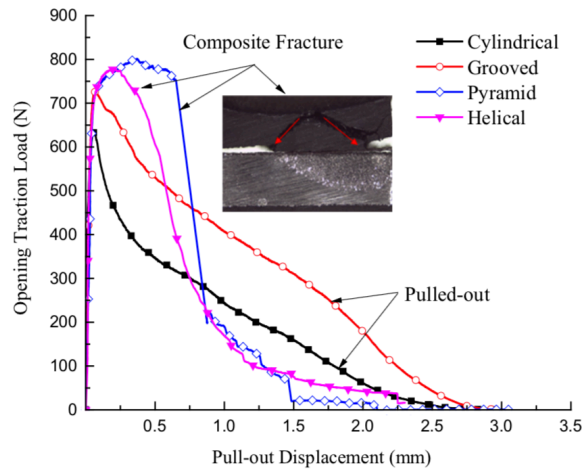


Figure 6.4 - Single pin pull-out test results for four different geometries

The pull-out response of the grooved pin was similar to the cylindrical pin, however, the maximum load increased by 14%, and the ultimate energy absorption increased by 60% as a result of the different post-peak stress reduction. This increase in load-carrying capability follows a calculated 30% increase in contact area, and an interlocking phenomenon in the surface grooves. This demonstrates that there exist three energy absorbing mechanisms at different length scales: the pin surface bond, the pin features and the composite fracture.

For the pyramid tip and helical pin, cracking in the composite was favoured, which caused a reduction in slope of the load-displacement curve. Following this, there was a small increase in load, before further cracking led to rapid loss of load. For the pyramid pin the cracking was observed in the composite around the pin tip and for the helical pin the cracking was midway along the pin. The maximum load of both geometries was around 20% higher than the baseline. In this respect, the use of geometry features increases the pin strength such that the composite adherend strength becomes the limiting factor for joint behaviour. In terms of energy though, the helical pin is on the same level as the baseline, while the pyramid pin gave 30% higher values.

6.2.3 - Pin offset angle investigation

In this study from Parkes et. al. [62], single pin specimens of varying offset angle are used to characterise the composite microstructure and the response of the single pin as it is pulled out of the composite under different loading combinations. Tested configurations are offset angles of 10°, 20°, and 30°.

As the mixed mode loading conditions are introduced with the use of offset pins, the load displacement behaviour and the corresponding absorbed energy varied significantly. The softening region of load-displacement curve changed from exponential to linear, producing a significant increase in total energy absorption even for small offset angles, with 63%, 87% and 93% increases for the 10°, 20° and 30° pins respectively. Reason for this increase in energy, is due to the crushing of fibres in the wedge zone, constrained by the displacement of

the two adherends, causing fragmentation of small regions, and compensating the decrease of friction forces due to a reduction of contact area. Again, the maximum force is not greatly affected by the offset angle, showing only minor increase compared to the straight pins. Nevertheless it is suggested to verify the optimal offset angle also in combination with the type of composite layer, as the wedge could cause excessive fibre bending and an extended resin rich area at the base of the pin, counterbalancing the positive effects of the angled pin layout.

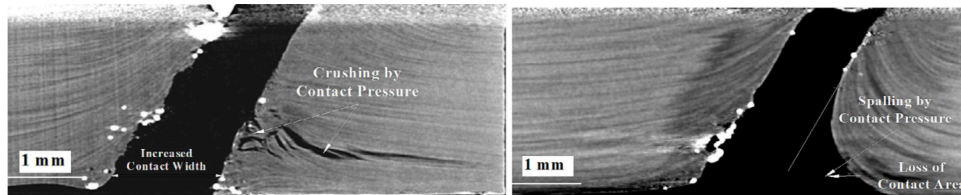


Figure 6.5 – Fibre alignment around the offset pin: good adhesion and crushing (left) vs, fibre curvature and poor adhesion (right).

6.2.4 Hybrid Penetrative Reinforcement (HYPER)

The technology presented is being developed by Airbus Group Innovations [63], and makes use of direct metal laser sintering is used to build pin arrays from a bed of titanium powder. The main advantage that sets apart this technology from the others is the particular pin geometry that offers unmatched capabilities. The pins provide a mechanical interlock, whilst the epoxy matrix provides adhesion around the pins and at the planar interface between adherends. At present, demonstrators are manufactured with pins built onto stock adherend material, however, it is anticipated that future applications will be designed from the ground up with integrated HYPER pins, allowing very significant weight savings (claimed up to 60%). The additional advantage of using AM with titanium alloys is the high tool wear with traditional machining manufacturing, thus adding to the overall feasibility of the solution.



Figure 6.6 – An array of additively manufactured, titanium HYPER pins.

Investigations to date have shown impressive results over unpinned counterparts and other technologies. This is due to the peculiar complex pin shape that can only be produced through AM technology. Under shear loading, the tests performed showed an increase of 300% and 128% in ultimate load when compared with bolted and bonded joints, respectively. The mean elongation at maximum load can be increased by over 400% and the energy absorbed can be

more than 80 times higher. Also, significant improvements of up to 6.5 times were revealed in terms of shear strength. Failure mode in single lap shear occurs by shear failure at the base of the metallic pins. In terms of pull-off strength and ultimate force, bolted joints and HYPER joints reveal an equivalent performance with the failure mode being dependent upon the feature geometry and array density. Preliminary investigations also showed no corrosion issues and good fatigue performance.

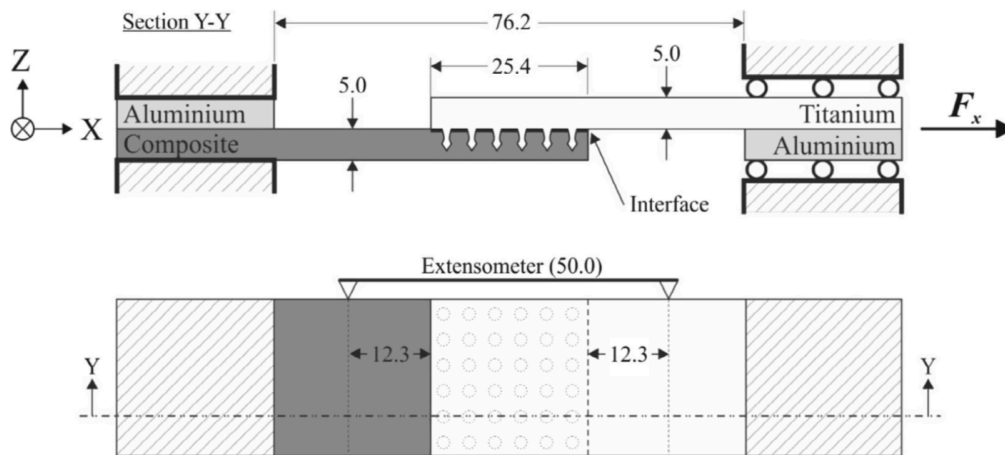


Figure 6.7 – Schematisation of single lap shear test of a HYPER joint solution.

Two pin designs were tested, both with the same conical head feature to increase the “locking” of fibres providing a strong mechanical bond following consolidation. The height and angles of the pin head were identical for both types and all pins penetrated approximately 75% through the laminate. The root diameter of the pins was the difference between the two designs and the alternative geometry was approximately 17% larger than that of the baseline pins.

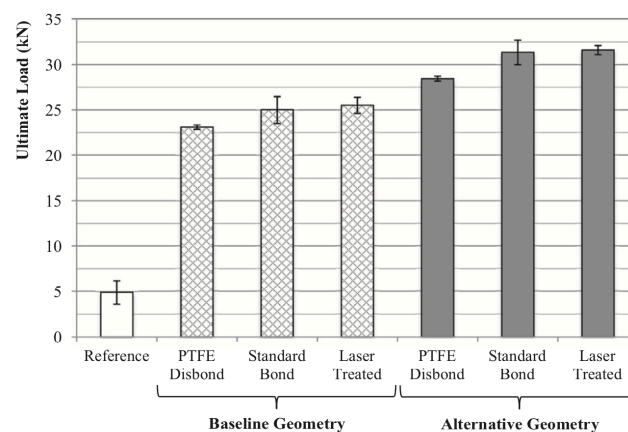


Figure 6.8 – Comparison of ultimate shear lap test load for tested configurations.

CONCLUSIONS

This thesis illustrates the results achieved during the three years of doctorate program.

The first topic addressed dealt with the identification of a reliable experimental procedure for the quantification of the energy absorption capability of composite materials. First, two analytical damage models are described in detail and the fundamental working and limitations are highlighted. The two numerical models are implemented in the numerical FE software Virtual Performance Solution from ESI-software. An experimental campaign was defined to find the necessary material properties to populate the two numerical models: a carbon fibre prepreg with high toughness epoxy resin is used for all coupon level activities. Simplified tests for elementary load cases are used to define the basic undamaged lamina properties, then specific tests are used to express the principal damaging mechanisms offered in the software. Each one of the experimental test is simulated in the numerical environment, following the principles of the building block approach. This allows to constantly verify the capability of the numerical models and the precision of the simulations with respect to real cases. The older Ladevèze continuum damage model uses a phenomenological approach to damage, and is able to capture the stiffness reduction of the laminate with good precision. On the other hand, the more recent Waas-Pineda progressive damage model uses an innovative approach to simulation consisting in the localisation of fracture planes within the continuum of the finite element representation. It allows to overcome the limitation of explicit numerical codes that require definite positiveness in the constitutive tangent modulus, and applies a cohesive-like behaviour to simulate fractures in the material. This model proved less accurate for elementary load cases, but is more accurate when simulating real components.

Finally, a corrugated specimen is manufactured and tested in axial compression until a quasi-static crushing behaviour appears. This geometry is chosen to perform the validation of the numerical models. It is clear that the Waas-Pineda model is superior in capturing the energy absorption mechanism of the crush test, although calibration is still an open key point. The model allows to input the fracture energies of each damage mode, a convenient procedure that translates directly to the crush force of the full geometry.

In a following activity, an experimental test bench for the measurement of the permeability of textile reinforcement is manufactured. This activity goes toward narrowing the gap between the promising, emerging liquid composite moulding technologies versus the traditional autoclave process. The formers are expected to bring composite materials to a broader market, by lowering the costs while increasing the manufacturing volumes. The equipment generates a linear infusion flow, solved in close form from the Darcy's law. Infusion is done using a synthetic oil with known viscosity, and the volume fraction – another required input – is calculated by submersion of the textile in a graduated cylinder. By repeating the measurement in three orientations of the textile, one is able to determine the full in-plane permeability tensor, with principal directions and offset angle with respect to

the fibre direction. The values of principal permeability are used as input in a FE model to solve complex infusion problems. The validation – described in a separate work – indicates that the correlation between experimental values, numerical simulations, and real case infusion of a marine component, is excellent.

Last topic, we presented an overview of emerging technologies for the bonding between metals and composites, which typically represent a weak link in the assembly of structures. Typical joints make use of fasteners or adhesive layers, that generally offer inferior strengths compared to the base materials. The introduction of additive manufacturing processes for metals, opened the possibility to design novel geometries that were not possible before. These techniques consist in creating a pattern of pins on the metal side, onto which the fibre reinforcement of the composite can set-in and provide “locking” effect, increasing the toughness tenfold compared to traditional solutions. Current research focused on the effects of different pin dimensions, shape, and offset angles, and indicate that a unique design principle is not available, but can be optimised for the specific load case of the joint.

REFERENCES

- [1] A.G Mamalis, D.E Manolakos, M.B Ioannidis, D.P Papapostolou, Crashworthy characteristics of axially statically compressed thin-walled square CFRP composite tubes: experimental, In *Composite Structures*, Volume 63, Issues 3–4, 2004, p.347-360.
- [2] A.G. Mamalis, D.E. Manolakos, M.B. Ioannidis, D.P. Papapostolou, On the experimental investigation of crash energy absorption in laminate splaying collapse mode of FRP tubular components, *Composite Structures*, Volume 70, Issue 4, 2005, p.413-429.
- [3] L Daniel, P.J Hogg, P.T Curtis, The crush behaviour of carbon fibre angle-ply reinforcement and the effect of interlaminar shear strength on energy absorption capability, *Composites Part B: Engineering*, Volume 31, Issue 5, 2000, p.435-440.
- [4] O. Allix, P. Ladeveze, E. Le Dantec, E. Vittecoq, Damage mechanics for composite laminates under complex loadings, *Symposium: Yielding Damage Failure of Anisotropic Solids, IUTAM/ICM (1988)*.
- [5] P. Ladevèze, A damage computational method for composite structures, *Computers & Structures*, Volume 44, Issues 1–2, 1992, p.79-87
- [6] P. Ladeveze, E. LeDantec, Damage modelling of the elementary ply for laminated composites, *Composites Science and Technology*, Volume 43, Issue 3, 1992, p.257-267.
- [7] P. Ladevèze, O. Allix, L. Gornet, D. Lévêque, L. Perret, A computational damage mechanics approach for laminates: Identification and comparison with experimental results, *Studies in Applied Mechanics*, Volume 46, 1998, p.481-500
- [8] L.M. Kachanov., Time of the rupture process under creep condition, *Izv Akad Nauk S.S.R. Otd Tech Nauk*, 8,1958, p. 26-31.
- [9] J. Lemaitre, How to use Damage Mechanics, *Nuclear and Design*, Volume 80, 1984, p.233-245.
- [10] P.P. Camanho, C.G. Dávila, S.T. Pinho, L. Iannucci, P. Robinson, Prediction of in situ strengths and matrix cracking in composites under transverse tension and in-plane shear, *Composites Part A: Applied Science and Manufacturing*, Volume 37, Issue 2, 2006, p.165-176.
- [11] Talreja, R. (1985b), Transverse cracking and stiffness reduction in composite laminates, *Journal of Composite Materials*, Volume 19, p.355–275.
- [12] A.F Johnson, A.K Pickett, P Rozycki, Computational methods for predicting impact damage in composite structures, *Composites Science and Technology*, Volume 61, Issue 15, 2001, p.2183-2192.
- [13] Schapery, R. A., On a Thermodynamic Constitutive Theory and Its Application to Various Nonlinear Materials, *Thermoinelasticity: Symposium East Kilbride, June 25--28, 1968*, p.259-285.
- [14] Schapery, R. A. (1990), A theory of mechanical behaviour of elastic media with growing damage and other changes in structure, *Journal of Mechanics and Physics of Solids*, Volume 38, Issue 2, p.1725–1797.

- [15] R.A. Schapery, D.L. Sicking, A theory of mechanical behaviour of elastic media with growing damage and other changes in structure, *Mechanical Behaviour of Materials*, 1995, p. 45–76.
- [16] Z.P. Bažant, B.H. Oh, Crack band theory for fracture of concrete, *Matériaux et construction* Volume 16, p.155-177.
- [17] E.J. Pineda, A Novel Multiscale Physics-Based Progressive Damage and Failure Modeling Tool for Advanced Composite Structures, Ph.D. thesis, University of Michigan, 2012.
- [18] E.J. Pineda, A.M. Waas, Numerical implementation of a multiple-ISV thermodynamically-based work potential theory for modeling progressive damage and failure in fiber-reinforced laminates, *International Journal of Fracture*, 2013, Volume 182, Issue 1, p.93-122
- [19] S. Müller, A. Tramecon, P. De Luca, A Mesh Insensitive Composite Damage Model for Crash Simulations, *Proc. American society for composites*, 31st Conference, 2016.
- [20] A.F. Johnson, A.K. Pickett, P. Rozycki, Computational methods for predicting impact damage in composite structures, *Composites Science and Technology* Volume 61, 2001, p.2183–2192.
- [21] L. Greve, A.K. Pickett, Modelling damage and failure in carbon/epoxy non-crimp fabric composites including effects of fabric pre-shear, *Composites Part A: Applied Science and Manufacturing*, Volume 37, Issue 11, 2006, p.1983-2001.
- [22] VV. AA. Volume 3 - Polymer matrix composites materials usage, design and analysis. MIL-HDBK-17-3F, p.1–693, Jul 2002.
- [23] VV. AA. Chapter 14 – Crashworthiness and energy management. MIL- HDBK-17-3F, 3:1–10, Dec 2005.
- [24] US Dept. of Transportation FAA. Advisory Circular 20-107b. pages 1–37, Sep 2009.
- [25] L. Giorgini, T. Benelli, L. Mazzocchett, C. Leonardi, Recovery of carbon fibers from cured and uncured carbon fiber reinforced composites wastes and their use as feedstock for a new composite production, *Polymer Composites*, Volume 36, p.1084–1095.
- [26] NIAR (WSU), NCAMP Test Report Number: CAM-RP-2009-015 Rev A, Hexcel 8552 IM7 Unidirectional Prepreg 190 gsm & 35%RC Qualification Material Property Data Report, 2011.
- [27] Standard Test Method for Tensile Properties of Polymer Matrix Composite Materials, ASTM D3039/D3039M – 14.
- [28] Standard Test Method for Compressive Properties of Polymer Matrix Composite Materials with Unsupported Gage Section by Shear Loading, ASTM D3410/D3410M – 03.
- [29] Standard Test Method for In-Plane Shear Response of Polymer Matrix Composite Materials by Tensile Test of a +/-45° Laminate, ASTM D3518/D3518M – 13.
- [30] A.F. Johnson, 14 - Modelling impact damage in composite structural elements, In C. Soutis, *Multi-Scale Modelling of Composite Material Systems*, 2005, p.401-429.
- [31] Standard Test Method for Mode I Interlaminar Fracture Toughness of Unidirectional Fiber-Reinforced Polymer Matrix Composites, ASTM D5528 – 13.
- [32] Standard Test Method for Determination of the Mode II Interlaminar Fracture Toughness of Unidirectional Fiber-Reinforced Polymer Matrix Composites, ASTM D7905/D7905M – 14.
- [33] Standard Test Method for Linear-Elastic Plane-Strain Fracture Toughness K_{Ic} of Metallic Materials, ASTM E399 – 12.
- [34] Standard Test Method for Translaminar Fracture Toughness of Laminated and Pultruded Polymer Matrix Composite Materials, ASTM E1922 – 04.
- [35] M.J. Laffan, S.T. Pinho, P. Robinson, A.J. McMillan, Translaminar fracture toughness testing of composites: A review, *Polymer Testing*, Volume 31, 2012, p. 481–489.
- [36] S.T. Pinho, P. Robinson, L. Iannucci, Fracture toughness of the tensile and compressive fibre failure modes in laminated composites, *Composites Science and Technology* Volume 66, 2006, p. 2069–2079.

- [37] M.J. Laffan, S.T. Pinho, P. Robinson, L. Iannucci, Measurement of the in situ ply fracture toughness associated with mode I fibre tensile failure in FRP. Part I: Data reduction, *Composites Science and Technology* Volume 70, 2010, p.606–613.
- [38] M.J. Laffan, S.T. Pinho, P. Robinson, L. Iannucci, Measurement of the in-situ ply fracture toughness associated with mode I fibre tensile failure in FRP. Part II: Size and lay-up effects, *Composites Science and Technology* Volume 70, 2010, p.614–621.
- [39] N. Zobeiry, R. Vaziri, A. Poursartip, Characterization of strain-softening behavior and failure mechanisms of composites under tension and compression. *Composites Part A Applied Science Manufacturing*, Volume 68, 2015, p.29–41.
- [40] P. Feraboli, F. Garattoni, Development of a test method for composite materials energy absorption: corrugated specimens, 48th AIAA/ASME/ASCE/AHS/ASC Structures, Dynamics and Materials Conference, No. 2007-2011, Waikiki, HI (USA) – Apr. 2007
- [41] F. Garattoni, Crashworthiness and composite materials: development of an experimental test method for the energy absorption determination and implementation of the relative numerical model, Ph.D. Thesis, University of Bologna, 2011.
- [42] A. F. Johnson and M. David, Failure Mechanisms and Energy Absorption in Composite Elements under Axial Crush, *Key Engineering Materials* Volumes 488-489, 2012, p.638-641.
- [43] ESI-software VPS 2017 Standard reference manual.
- [44] G. Barenblatt, The mathematical theory of equilibrium cracks in brittle fracture, *Advancements in Applied Mechanics* 1962, Volume 7, p.55–129.
- [45] M.L. Falk, A. Needleman, J.R. Rice, A critical evaluation of cohesive zone models of dynamic fracture, *Journal of Physics IV*, 2001, p.543–550.
- [46] J.R. Rice, Dislocation nucleation from a crack tip – an analysis based on the PIERLS concept. *Journal of Mechanics and Physics of Solids* 1992, Volume 40, p.239–271.
- [47] A. Hillerborg, M. Modeer, P.E. Petersson, Analysis of crack formation and growth in concrete by means of fracture mechanics and finite elements. *Cement Concrete Res* 1976, Volume 6, p.773–782.
- [48] A. Turon, C.G. Davila, P.P. Camanho, J. Costa, An engineering solution for mesh size effects in the simulation of delamination using cohesive zone models, *Engineering Fracture Mechanics*, Volume 74, 2007, p.1665–1682.
- [49] H. Darcy, *Les fontaines publiques de la ville de Dijon*, Dalmont, Paris, 1856.
- [50] T.S. Lundstrom, R. Stenberg, R. Bergstrom, H. Partanen, P.A. Birkeland, In-plane permeability measurements: a nordic round-robin study, *Composites: Part A*, Volume 31, 2000, p.29–43.
- [51] J.R. Weitzenböck, R.A. Shenoi, P.A. Wilson, Radial flow permeability measurement. Part A: Theory, *Composites: Part A*, Volume 30, 1999, p.781–796.
- [52] J.R. Weitzenböck, R.A. Shenoi, P.A. Wilson, Radial flow permeability measurement. Part B: Application, *Composites: Part A*, Volume 30, 1999, p.797–813.
- [53] S. Sharma, D. Siginer, Permeability Measurement Methods in Porous Media of Fiber Reinforced Composites, *Applied Mechanics reviews*, Volume 63, 2010.
- [54] J.R. Weitzenböck, R.A. Shenoi, P.A. Wilson, Measurement of three-dimensional permeability, *Composites Part A: Applied Science and Manufacturing*, Volume 29, p.159- 169.
- [55] R. Arbter, J.M. Beraud, C. Binetruy, L. Bizet, J. Bréard, S. Comas-Cardona, C. Demaria, A. Endruweit, P. Ermanni, F. Gommer, S. Hasanovic, P. Henrat, F. Klunker, B. Laine, S. Lavanchy, S.V. Lomov, A. Long, V. Michaud, G. Morren, E. Ruiz, H. Sol, F. Trochu, B. Verleye, M. Wietgreffe, W. Wu, G. Ziegmann, Experimental determination of the permeability of textiles: A benchmark exercise, *Composites Part A: Applied Science and Manufacturing*, Volume 42, Issue 9, 2011, p.1157-1168.

- [56] N. Vernet, E. Ruiz, S. Advani, J.B. Alms, M. Aubert, M. Barburski, B. Barari, J.M. Beraud, D.C. Berg, N. Correia, M. Danzi, T. Delavrière, M. Dickert, C. Di Fratta, A. Endruweit, P. Ermanni, G. Francucci, J.A. Garcia, A. George, C. Hahn, F. Klunker, S.V. Lomov, A. Long, B. Louis, J. Maldonado, R. Meier, V. Michaud, H. Perrin, K. Pillai, E. Rodriguez, F. Trochu, S. Verheyden, M. Wietgreffe, W. Xiong, S. Zaremba, G. Ziegmann, Experimental determination of the permeability of engineering textiles: Benchmark II, *Composites Part A: Applied Science and Manufacturing*, Volume 61, 2014, p.172-184.
- [57] P. Ferland, D. Guittard, F. Trochu, Concurrent methods for permeability measurement in resin transfer molding. *Polymer Composites*, 1996, Volume 17, p.149–158.
- [58] M. Tiago von H.P.F. Silva, P. Camanho, A.T. Marques, P. M.S.T. Castro, 3D-reinforcement techniques for co-bonded CFRP/CFRP and CFRP/metal joints: a brief review, *Ciência & Tecnologia dos Materiais*, Volume 29, Issue 1, 2017, p.e102-e107.
- [59] D. Herzog, V. Seyda, E. Wycisk, C. Emmelmann, Additive manufacturing of metals, *Acta Materialia*, Volume 117, 2016, p.371-392.
- [60] A. Nguyen, M. Brandt, S. Feih, A.C. Orifici, Pin pull-out behaviour for hybrid metal-composite joints with integrated reinforcements, *Composite Structures*, Volume 155, 2016, p.160-172
- [61] A. Nguyen, C.K. Amarasinghe, M. Brandt, S. Feih, A.C. Orifici, Loading, support and geometry effects for pin-reinforced hybrid metal-composite joints, *Composites Part A: Applied Science and Manufacturing*, Volume 98, 2017, p.192-206.
- [62] P.N. Parkes, R. Butler, J. Meyer, A. de Oliveira, Static strength of metal-composite joints with penetrative reinforcement, In *Composite Structures*, Volume 118, 2014, Pages 250-256.
- [63] K. Bodjona, L. Lessard, Hybrid bonded-fastened joints and their application in composite structures: A general review, *Journal of Reinforced Plastics and Composites*, 2016, p.1–18